Spectral characterization of solid-state laser-driven plasma sources of EUV light

Ruben Schupp

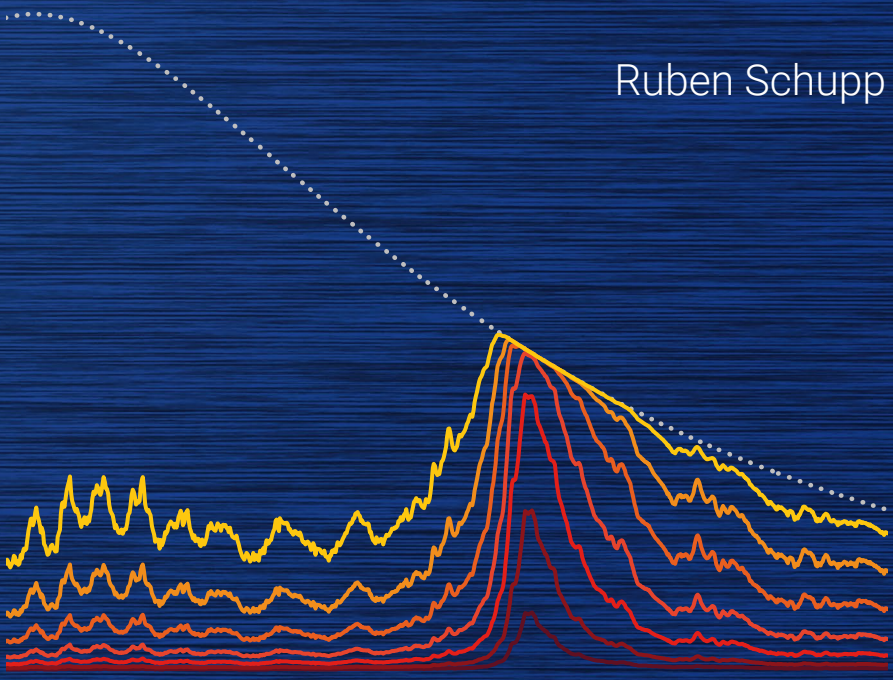

VRIJE UNIVERSITEIT

Spectral characterization of solid-state laser-driven plasma sources of EUV light

ACADEMISCH PROEFSCHRIFT

ter verkrijging van de graad Doctor of Philosophy
aan de Vrije Universiteit Amsterdam,
op gezag van de rector magnificus
prof.dr. V. Subramaniam,
in het openbaar te verdedigen
ten overstaan van de promotiecommissie
van de Faculteit der Bètawetenschappen
op woensdag 17 maart 2021 om 13.45 uur
in de aula van de universiteit,
De Boelelaan 1105

door

Ruben Schupp

geboren te Ehringshausen, Duitsland

promotoren:	dr. O.O. Versolato
	prof.dr. W.M.G. Ubachs
	prof.dr.ir. R.A. Hoekstra

This thesis was approved by the members of the reviewing committee:

prof.dr. M.R. de Baar (DIFFER and Eindhoven University of Technology)
prof.dr. R. Croce (Vrije Universiteit Amsterdam)
prof.dr.ir. H.L. Offerhaus (University of Twente)
dr. E. Sokell (University College Dublin)
dr.ir. H.O. Folkerts (ASML)

The research reported in this thesis was carried out at the Advanced Research Center for Nanolithography (ARCNL), a public-private partnership between the University of Amsterdam (UvA), Vrije Universiteit Amsterdam (VU), the Netherlands Organization for Scientific Research (NWO), and the semiconductor equipment manufacturer ASML.

Cover: Spectral emission of tin plasma in the extreme ultraviolet regime calculated for optical depths of 0.2, 0.7, 2, 4.5, 10, 20 and 40 (solid lines) and for a blackbody of 34 eV temperature (dotted line). The spectra shown are produced by applying the one-dimensional radiation transport model described in Chapter 4 to an experimentally recorded spectrum where a tin microdroplet was irradiated by a 2-μm-wavelength laser pulse.

ISBN: 978-94-92323-48-4

Contents

Introduction **1**

1 Efficient generation of extreme ultraviolet light from Nd:YAG-driven microdroplet-tin plasma **11**
1.1 Introduction 12
1.2 Experimental setup 13
1.3 Measurement results 17
1.4 Plasma expansion model 21
1.5 Model fit and discussion 23
1.6 Increasing radiative efficiency 25
1.7 Conclusion 27

2 Radiation transport and scaling of optical depth in Nd:YAG laser-produced microdroplet-tin plasma **29**
2.1 Introduction 30
2.2 Experiment 31
2.3 Methods 32
2.4 Results 34
2.5 Conclusion 38

3 Extreme ultraviolet light from a tin plasma driven by a 2-μm-wavelength laser **39**
3.1 Introduction 40
3.2 Experimental setup 41
3.3 Results 43
3.4 Conclusion 49

4 Characterization of 1- and 2-μm-wavelength laser-produced microdroplet-tin plasma for generating extreme ultraviolet light **51**
4.1 Introduction 52
4.2 Experiment 53

4.3 Scaling of spectral features with laser intensity and wavelength 54
4.4 Scaling of optical depth 60
4.5 Conclusions 65
4.A Appendix 66

5 Characterization of angularly resolved EUV emission from 2-μm-wavelength laser-driven Sn plasma using preformed liquid disk targets 69
5.1 Introduction 70
5.2 Experiment 71
5.3 EUV generation using 2-μm light on preformed targets 75
5.4 EUV generation using 1- and 2-μm laser light 81
5.5 Conclusions 84

References 85

List of publications 97

Acknowledgments 99

Introduction

Microelectronics, especially in the form of integrated circuits, has become an essential part of our everyday lives, be it in the form of consumer electronics such as smart phones and personal computers, or in bigger settings such as computer clusters used, e.g., for weather forecasting or to power search engines. The groundbreaking innovation making all of these applications possible was the transistor, a device proposed by J.E. Lilienfeld in the early twentieth century [1, 2]. In 1947, a first working device was built in the form of a point-contact transistor [3]. The extreme miniaturization of electronics over the last few decades was later made possible by introduction of the metal–oxide–semiconductor field-effect transistor (MOSFET). This device, invented in 1959, allowed for mass-production and efficient size reduction via photolithography [4].

In photolithography (referred to in the following as simply 'lithography'), light is used to imprint a pattern encoded on a mask onto a substrate. The mask is illuminated either in reflection or transmission after which the light is imaged onto a silicon wafer coated with a photoresistive chemical. Upon illumination, the structure of the chemical is altered and in subsequent processes the excess material is removed, leaving behind the printed structure. Over the years, the development of new complex techniques enabled the continued shrinkage of printed feature sizes while lithography continued to be the underlying production method. The progressive miniaturization of printable features is commonly gauged by the number of transistors printed per unit area. The latter was predicted by G.E. Moore to roughly double every two years, while the cost per transistor was predicted to approximately halve within the same time period [5, 6]. These predictions were closely followed by the semiconductor industry for several decades [7].

One of the main enablers for this achievement has been the use of ever-shorter wavelength light in the lithography process. While first lithography machines used light from mercury lamps of approximately 400 nm wavelength, these lamps were soon replaced by shorter-wavelength laser sources operating in the deep-ultraviolet (DUV) spectral regime in order to increase printing resolution. Following Abbe's resolution limit, the smallest feature size which can be printed, the so-called critical dimension (CD), is given by $\mathrm{CD} = k_1 \lambda / \mathrm{NA}$. The CD clearly scales with the wavelength λ of the light source. The remaining factors are the numerical aperture (NA)

of the illumination system and a production process specific constant k_1, typical values in DUV lithography systems being 0.3–0.4 [8], and are relatively more limited in their optimization. Nevertheless, after the introduction of ArF excimer lasers as light source at a 193 nm wavelength, the resolution scaling via wavelength came to an abrupt halt because of a lack of economically feasible high-power light sources at shorter wavelengths as well as increased difficulties arising from the strong absorption of shorter wavelength light by virtually all materials. These constraints made DUV lithography the standard for more than two decades and creative techniques were developed to continue the miniaturization of printable structures [8]. One important achievement towards further miniaturization was the increase of the system NA by insertion of a liquid with refractive index $n > 1$ between the illumination optics and the wafer. Another important advancement was the introduction of so-called multi-patterning, the process by which multiple illumination cycles are used to print a single structure. Nowadays, the technique of multi-patterning enables the printing of features well below the resolution limit of DUV lithography systems. The use of multi-patterning does however significantly increase the amount of production steps and in turn the cost per transistor. Hence, a new technological breakthrough was needed: lithography in the extreme ultraviolet (EUV) spectral region.

Using a shorter 13.5-nm wavelength, the printing resolution of ASML's lithography systems has further improved and the proposed high-NA imaging systems (NA = 0.55) will enable the introduction of 3 nm nodes within the next years [8, 9]. One of the main reasons for the choice of 13.5-nm light is the good reflectivity of producible multilayer optics at this wavelength which efficiently reflect in a 2% bandwidth around said wavelength, the so-called *in-band* region [10]. After deciding on an appropriate light source wavelength, the type of light source had to be chosen. Consideration was given to free-electron lasers, laser-produced plasmas (LPPs) or discharge produced plasmas. Based on factors including required EUV power, source up-time and assessment of financial risks, LPP sources using mass-limited targets eventually became the light source of choice. In these LPP sources, tin microdroplets are irradiated in a two-pulse scheme. First, a low-intensity prepulse propels and deforms the droplets into extended targets. These targets are subsequently illuminated by a second high-intensity pulse to create a hot, EUV-emitting tin plasma [11]. Tin was chosen over other elements, such as lithium, because a plethora of its charge states emit strongly at 13.5 nm, promising high efficiencies of converting laser light into the desired in-band radiation. Specifically, the tin charge states Sn^{10+}–Sn^{14+} emit intense in-band radiation. Within these ions, strong dipole transitions from singly excited states closely align around 13.5 nm, caused by strong configuration interaction of the respective atomic sub-shells. Recently, Torretti *et al.* have found that transitions between multiply excited states in these ions make a prominent contribution to emission features both in and around

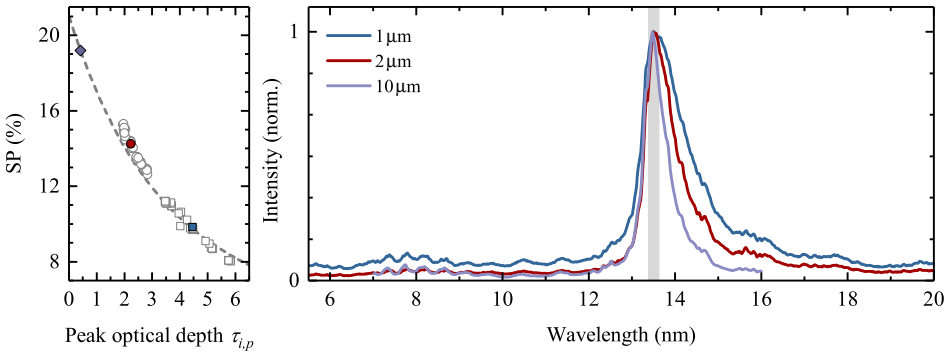

Figure 1: Left: Spectral purity of tin plasmas as a function of their optical depth as determined in Chapter 4. The dashed line indicates the SP as expected from a scaling of the spectral emission using an analytical 1D radiation transport model, outlined in Chapters 2 and 4. Right: corresponding spectra for the three wavelength cases depicted in the left panel and normalized to their peak emission. Spectra for 1- and 2-µm drive lasers are obtained from irradiating a 30-µm-diameter droplet and the spectrum for the 10-µm drive-laser case is recorded from a plasma formed from an extended tin target (reproduced from Ref. [13]). The gray shading depicts the in-band region matching the reflectivity of available Mo/Si multilayer optics.

the in-band region [12].

Now, after more than two decades of research and development, tin-droplet-based EUV light sources recently have entered the market and EUV lithography already has become a key technology enabling 7 nm nodes and beyond. Historically, CO_2 gas lasers were chosen to drive the plasma because of good scalability of their output power combined with the high obtainable efficiency of converting laser light into in-band radiation within a 2π hemisphere covered by light-collecting optics. This efficiency is referred to as the conversion efficiency (CE). Current machines produce more than 250 W of in-band radiation at CE values of 5-6% [11].

One of the enablers of high CE values using CO_2 lasers is the absorption of the $\lambda_L = 10.6\,\mu m$ laser light in relatively low-density regions of the plasma (typically 10^{18}–$10^{19}\,e^-/cm^3$) by the process of inverse bremsstrahlung. A low plasma density is, in turn, typically connected to a high ratio of in-band emission to overall EUV emission. This ratio defines the spectral purity (SP), and SP values as high as 20% have been measured in the case of CO_2-driven plasmas. An example of the spectral emission of such a CO_2-driven plasma is shown in Fig. 1. Also shown are spectra for 1- and 2-µm wavelength laser irradiation of droplet targets investigated in this thesis. Comparing the three wavelength cases, an advantage of the low den-

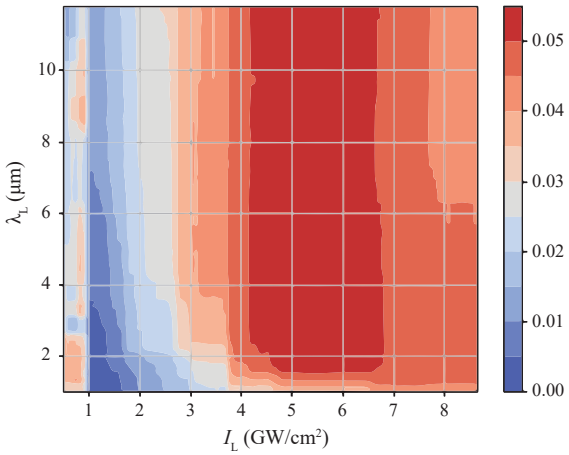

Figure 2: CE values simulated using the Lawrence Livermore National Laboratory HYDRA code [14] in one dimension. A thin liquid tin disk is irradiated with a tens-of-nanoseconds-long laser pulse of varying laser wavelength (λ_L) and intensity (I_L) to explore CE dependence on these two quantities. Modified from Ref. [15].

sity CO_2-driven plasma regarding SP becomes apparent in terms of the narrower 13.5 nm emission feature. The broadening of the spectral feature at 13.5 nm in the 1- and 2-μm cases can in part be understood in terms of the higher plasma density at which these shorter drive laser wavelengths are absorbed. Radiation produced in these denser regions, all other things being equal, encounters a higher column density of tin atoms that absorb and re-emit the radiation on its way out of the plasma, re-distributing spectral energy into wavelength bands other than the desired 2% bandwidth around 13.5 nm. The strength of this absorbance and re-emitance is quantified in the optical depth of the plasma. The optical depth is dependent on three factors: first, the ability of the atoms in the plasma to absorb radiation, quantified in terms of the opacity α_λ. Second, the length of the emitter column l. And third, the density of emitters, expressed in terms of the plasma's mass density ρ. In case of a short drive laser wavelength, e.g. 1 or 2 μm, the EUV-producing plasma has higher density (compared to a 10 μm CO_2-driven one), resulting in an increased optical depth that reduces the spectral purity, as shown in the left panel of Fig. 1.

In order to further optimize the CE of EUV light sources, consideration must be given to additional factors, such as the ability of the laser energy to be absorbed by the plasma as well as the fraction of this absorbed energy that is emitted as radiation into the hemisphere covered by light-collecting optics. One such example of this is recent simulation work performed by researchers at Lawrence Livermore

National Laboratory, shown in Fig. 2. In their simulations, CE was explored regarding the drive laser wavelength as well as its intensity using the HYDRA code [14] in one dimension and laser pulses of several-ten nanoseconds were used to illuminate thin sheets of liquid tin. Interestingly, a significant increase in CE with drive laser wavelength is observed, with a value of ∼3% obtained for a 1-μm driver, ending in a long-stretched optimum of constant CE above 5% starting at just below 2 μm and continuing to well above 10 μm. This simulation result highlights potentially high-obtainable CE's in the experimentally unexplored near- to mid-infrared region, where efficient high-power, solid-state laser technology has been developed over the last years. A strong advantage of these solid-state laser systems is their up to several times higher wall-plug efficiency than that of CO_2 gas lasers. Especially wavelengths near 2 μm are of interest where currently very promising high-power Big-Aperture-Thulium (BAT) laser technology at a 1.9-μm wavelength is under development that may become available for EUV light source applications in the near future [16]. Even though the CE for a 1-μm drive laser wavelength may be slightly lower, the high wall-plug efficiencies achievable with solid-state laser technology may lead to an overall more efficient EUV light source considering the ratio of usable EUV photons to electrical power. The 1-μm wavelength is further opportune because already today high-power lasers exist at a mature stage of development, ready for industrial use.

Another advantage of a shorter drive laser wavelength is that the higher density of the EUV emitting plasma allows for larger amounts of in-band radiation to be produced within a small plasma volume. This is important as in-band photons are only usable if they are produced within the etendue of the light collecting optics of the light source. The high SP values attainable in CO_2-driven plasmas come at the cost of emitter density and much larger plasma sizes are required to obtain equivalent amounts of in-band radiation. Consequently, figures of merit next to CE may be needed in the future in the form of, e.g., a CE value normalized to the plasma volume in which the in-band radiation is produced. A final optimization of an EUV light source will need to take into account the amounts of produced debris, be it in the form of fast ionic and atomic debris or larger particles such as tin clusters and microparticles, as well as radiation outside the desired in-band region. This debris needs to be manageable to enable long up-times of the EUV light source.

Because of the complex interplay of all of the above mentioned parameters, a careful optimization of high-power EUV light sources is required for each drive laser wavelength in order to find the optimal operating conditions. Overall, near-infrared solid-state lasers present a very promising class of drive laser candidates for future generations of industrial EUV light sources.

Outline and summary

In this thesis, the fundamental limits of converting laser radiation via tin plasma into a 2% bandwidth around 13.5 nm, relevant to nanolithographic applications, are experimentally investigated. For light source optimization, the effects of varying laser irradiation parameters (i.e., laser wavelength, laser intensity and beam spot size) and varying target morphologies on EUV spectra, CE's, SP's and the plasma's optical depth have been studied systematically.

In Chapter 1, the efficiency of radiating EUV light of a spherical tin droplet illuminated by high-energy, 1-μm-wavelength laser pulses is investigated. The employed pulses are of constant intensity in space and time to homogeneously heat the plasma. A significant growth of CE and of the overall efficiency in radiating light is found with increasing laser intensity, droplet size and laser pulse duration. The increase in the fraction of laser energy that is radiated away by the plasma is explained by a larger fraction of laser energy absorbed by the plasma, which can be described by a simple plasma expansion model assuming a constant radial plasma expansion speed. By using a more optimal ratio of laser beam to droplet size, promising conversion efficiencies of up to 3.2% are obtained. This 3.2% CE value combined with the higher wall-plug efficiency of 1-μm solid-state lasers over CO_2 gas lasers may make 1-μm light a feasible drive laser wavelength for EUV light source applications, challenging current industrial sources on their efficiency of converting electrical power to in-band energy.

In Chapter 2, the spectral data of Chapter 1 is analyzed in the context of its optical depth using a one-dimensional, analytical radiation transport model and changes in optical depth with droplet size and laser pulse duration are quantified. The model relates any two experimental spectra, allowing one to reproduce all spectra from any experimental spectrum by means of a single free parameter, the relative optical depth. Using this model, we find a linear increase of optical depth with droplet diameter with a slope coefficient that increases with laser pulse duration. With optical depth being the product of the plasma's opacity, density, and scale length, the increase in optical depth is interpreted as an increase in effective plasma scale length. The results from this chapter provide guidance for EUV light source design, showing that plasma scale length should be kept small to reach the full CE potential in the case of dense, 1-μm-driven plasma.

In Chapter 3, a change towards a longer solid-state drive laser wavelength is made, exploring the wavelength regime between the well-known drive-laser cases of 1 and 10 μm. Laser pulses of 2-μm wavelength, produced by a master oscillator power amplifier system built at ARCNL, are used to create plasma on a planar-solid tin target. The measurements are then compared to ones using a 1-μm driver in order to study the change in plasma emission with drive laser wavelength. Via comparison of charge-state-specific features in the recorded emission spectra, we find

that in order to maintain a certain average charge state in the plasma, and with it the plasma temperature, an inverse linear scaling of drive laser intensity with laser wavelength is required. In the 2-μm case, a high CE value of 3.1% is measured at an angle of 60° with respect to the incident laser axis. This value is roughly a factor of 2 higher than the 1-μm case under similar experimental conditions. The two times higher CE value correlates well to the observed factor of 2 improvement in SP. In the spectral emission of the 1-μm case, strong absorption of in-band radiation is observed which explains the origin of a lower SP value in this case compared to the 2-μm case. The absorption of radiation around 13.5 nm is qualitatively explained using an analytical 1D-radiation transport model comprising two plasma zones of different temperature and density, where in Chapter 2 a single zone was sufficient. The high CE and SP for the 2-μm driver highlight its potential in driving plasmas in EUV light source applications.

After the brief intermezzo on planar-solid targets, we investigate in Chapter 4 the difference in plasma formation and emission between 1- and 2-μm-driven plasmas from droplet targets. As in Chapter 3, charge-state-specific features between the two wavelength cases are compared, confirming the inverse linear scaling of drive laser intensity with laser wavelength also for the droplet target case. The experimental results are found to be in agreement with theoretical predictions based on the plasma's equation-of-state as well as with results from radiation hydrodynamic simulations conducted with the RALEF 2D code [17]. These simulations reveal an inverse scaling of electron density with laser wavelength. The lower density in the longer drive laser wavelength case is understood from the fraction of laser energy absorbed via inverse bremsstrahlung, which scales with the product of plasma density and drive laser wavelength. Lastly, the recorded spectra are investigated in the context of their peak optical depth, using an improved model from that presented in Chapter 2. A smaller optical depth is found in the 2-μm case and the reduction in optical depth is traced to the reduction in plasma density. The lower optical depth and resulting higher SP values for the 2-μm driver combined with its high coupling efficiency with the plasma again suggest that this wavelength may be well suited for EUV light source applications, allowing for relatively high CE values over a wide range of plasma sizes.

Chapter 5 connects all previous chapters by studying the plasma emission from preformed tin droplets for drive laser wavelengths of 1 and 2 μm. In a two-pulse scheme, spherical tin droplets are first deformed to disk-like targets. These disk-like targets are then irradiated using a second, higher-intensity laser pulse. We have studied the influence of target diameter, laser wavelength, laser intensity and laser pulse duration on EUV spectra, SP's and CE's. Surprisingly, high CE values of up to approximately 3% in the 2-μm-driven plasma are almost independent of pulse duration and laser intensity within the scanned range. This is a promising result, indicating that EUV light source power may be scaled via those parameters

at little to no cost regarding CE. We further find, as in Chapter 1, that CE is strongly dependent on target size and with it on the fraction of laser energy absorbed by the target, finding back the CE and SP values of the planar-solid and droplet target cases as studied in Chapters 3 and 4. Comparing the two drive laser wavelength cases, we again find strong self-absorption in the 1-μm-driven plasma at large target sizes, which drastically reduces the attainable CE's. These results highlight the potential benefits from the use of a 2-μm drive laser system in EUV light source applications using mass-limited droplet targets.

In summary, solid-state lasers operating at 1- or 2-μm wavelength show high potential for use as drive lasers in future generations of EUV light sources. In addition to the here conducted studies it is of interest to further extend the range of drive laser wavelengths toward the mid-infrared regime. Even though there are no high-power solid-state lasers readily available in this wavelength range, experimental investigations of plasmas produced at these mid-infrared wavelengths will further deepen the physical understanding of the laser-plasma interaction and measurements of the plasma's spectral emission will aid the understanding of radiation transport processes within the plasma. In addition, further investigations are needed before the possible use of 1- or 2-μm lasers in industrial EUV light sources. First, a more extensive investigation of the obtainable CE using a 2-μm drive laser wavelength is needed. This investigation could include, e.g., heating of the tin targets with a more homogeneous laser intensity profile as was carried out with the 1-μm driver in Chapters 1 and 2. Second, it will be of interest to investigate scaling relations that capture the laser pulse parameters required to fully evaporate the tin targets in order to obtain a truly 'mass-limited' EUV light source where no tin particle clusters remain at the end of the EUV-creating laser pulse. For parameter sets where a full evaporation of the target material is achieved, detailed measurements of the size of the in-band emitting region and of the resulting ion debris will be essential to assess the the potential of 1- or 2-μm wavelength drive lasers for use in industrial EUV light sources.

1 | Efficient generation of extreme ultraviolet light from Nd:YAG-driven microdroplet-tin plasma

R. Schupp, F. Torretti, R. A. Meijer, M. Bayraktar, J. Scheers, D. Kurilovich, A. Bayerle, K. S. E. Eikema, S. Witte, W. Ubachs, R. Hoekstra, and O. O. Versolato

Physical Review Applied **12**, 014010 (2019)

We experimentally investigate the emission of extreme ultraviolet (EUV) light from a mass-limited laser-produced plasma over a wide parameter range by varying the diameter of the targeted tin microdroplets and the pulse duration and energy of the 1-μm-wavelength Nd:YAG drive laser. Combining spectroscopic data with absolute measurements of the emission into the 2% bandwidth around 13.5 nm relevant for nanolithographic applications, the plasma's efficiency in radiating EUV light is quantified. All observed dependencies of this radiative efficiency on the experimental parameters are successfully captured in a geometrical model featuring the plasma absorption length as the primary parameter. It is found that laser intensity is the pertinent parameter setting the plasma temperature and the tin ion charge state distribution when varying laser pulse energy and duration over almost two orders of magnitude. These insights enabled to obtain a record-high 3.2% conversion efficiency of laser light into 13.5 nm radiation and to identify paths towards obtaining even higher efficiencies with 1 μm solid-state lasers that may rival those of current state-of-the-art CO_2-laser-driven sources.

1.1 Introduction

Highly charged tin ions in laser-produced transient plasmas are the atomic sources of extreme ultraviolet (EUV) light at 13.5 nm wavelength for nanolithography [18–32]. In state-of-the-art EUV sources such plasmas are produced by irradiation of micrometer-sized tin droplets with high-power CO_2-gas-laser pulses [11, 33, 34] in a two-step process where first a laser pre-pulse [11, 33–39] shapes the droplet into a target optimized for EUV production with a second, more energetic pulse. Key physical processes were reviewed by Banine *et al.* [31].

Alternatively, solid-state 1-μm-wavelength Nd:YAG laser systems can be used for plasma creation, offering significant advantages over the 10-μm-wavelength CO_2 drive laser. The advantages include an improved energy efficiency, a significantly more compact size at same output power and improved temporal pulse shaping capabilities. Moreover they could enable a single-pulse irradiation scheme. YAG systems may in fact replace CO_2 lasers if the efficiency of converting laser energy into radiation within a 2% bandwidth around 13.5 nm that can be reflected by multilayer optics [10, 40] gets sufficiently competitive.

Nd:YAG-driven light sources have a much higher, near complete laser absorptivity due to the strong increase of the critical plasma electron density n_c with decreasing wavelength λ ($n_c \propto \lambda^{-2}$). The cross section of the here dominant [41] inverse bremsstrahlung absorption mechanism strongly increases with electron density [42, 43]. However, the density increase may cause self-absorption of the emitted EUV light, leading to opacity-broadened emission [44–47]. In turn, more light is emitted outside of the accepted bandwidth. Modeling these opacity effects challenges even the most advanced atomic structure calculations [29] due to the strongly correlated electronic structure of the multielectron open-4*d*-shell tin ions raising the need for experimental investigations.

The literature on Nd:YAG-driven tin plasma mostly deals with the emission from planar-solid targets [46–57], tin-coated spherical targets [44, 58–62], or liquid-droplet targets out of tin alloys [63]. The literature covering the emission properties of laser-produced plasma (LPP) from high-purity tin microdroplets, the industrial targets of choice, remains scarce [64–66].

Here, we present the results of a systematic investigation of the characteristics of the EUV spectra of these sources over a wide parameter range, varying the diameter of the targeted, pure tin microdroplets (16–65 μm), the laser pulse duration (0.5–25 ns) and its energy, presented as intensity [$(0.1–2.7) \times 10^{11}$ W/cm^2], using a transmission-grating spectrometer [67, 68]. The combination of this spectroscopic data with absolute measurements of the *in-band* emission in the 2% bandwidth around 13.5 nm enables three linked figures of merit to be obtained characterizing the emission from the plasma: spectral purity, conversion efficiency, and radiative efficiency. Conversion efficiency (CE) is commonly used and represents

the ratio of $E_{\mathrm{IB},2\pi}$ over the energy of the drive laser (E_{L}). $E_{\mathrm{IB},2\pi}$ is the total in-band radiation emitted into the half sphere back towards the laser that is reflected by the light collection optics in industrial sources. Spectral purity (SP) is defined as the ratio of $E_{\mathrm{IB},2\pi}$ and total EUV energy ($E_{\mathrm{rad},2\pi}$) emitted in the same half sphere. Through basic energy conservation considerations, SP serves as an absolute upper limit to the conversion efficiency: CE $\leq$ SP, where CE approaches SP only in the case of light emission solely in the backward-facing half sphere. This limit value is lowered by considering that light is also emitted in the opposite, forward-facing half sphere. Indeed, a more stringent limit of CE $\leq$ SP/2 holds in the case of spherically symmetric emission [69]. These limits emphasize the importance of spectroscopic investigations as introduced here.

Considering the application purposes, the radiative efficiency η_{rad} is defined as the ratio of $E_{\mathrm{rad},2\pi}$ to laser energy E_{L} and it thus equals the ratio CE/SP. Simulation works predict that in total 70% up to 90% of the absorbed laser light is emitted as radiation [70–72]. For optimal, high-CE source operation both SP and radiative efficiency should be as high as possible. A further crucial requirement is that the plasma should create manageable amounts of debris comprising, e.g., fragments or high-energy particles that could limit the optics lifetime. Laser energy not contributing to radiation may instead contribute to generating fast ionic debris. Possible gains in radiative output power should be carefully measured out against, e.g., increases in the material load on the optical components. A full quantification of various debris loads is left for future work.

In order to optimize the three figures of merit of EUV-source operation, we introduce a geometrical model with the plasma-absorption length as its prime parameter. The model describes very well the dependencies of η_{rad} on source parameters such as droplet size and laser-beam size. Employing these insights, we obtain a record-high CE of 3.2% and identify paths towards even higher values.

This paper is structured as follows. In Section 1.2 the experimental setup is introduced, followed by a description of the measurements in Section 1.3. A plasma expansion model is presented in Section 1.4 that is applied to the experimental data in Section 1.5. In Section 1.6 we apply the found scalings to an industrially relevant case and close with a discussion of our findings in Section 1.7.

1.2 Experimental setup

Molten Sn of 99.995% purity is pushed through a capillary glass tube with a micrometer-sized orifice into a vacuum chamber of 5×10^{-7} mbar background pressure. Plateau-Rayleigh instabilities lead to the breakup of the liquid stream into small fragment droplets. Evenly sized microdroplets are produced from these fragments by inducing a pressure modulation on the liquid stream in the glass tube leading to a

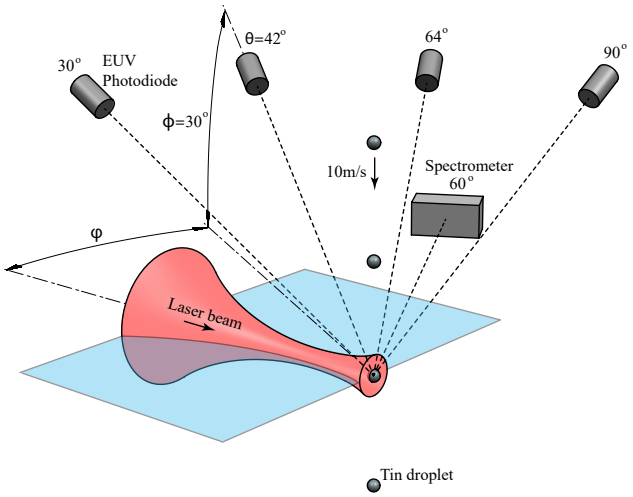

Figure 1.1: Schematic representation of the experimental setup. The laser beam, depicted in red, illuminates the falling tin microdroplets (gray spheres). The produced plasma emission is observed using a transmission-grating spectrometer (gray box) as well as four EUV photodiode assemblies (gray cylinders) measuring the absolute amount of produced in-band radiation. All angles θ are indicated with respect to the laser-beam propagation axis, with $\cos\theta = \cos\phi\cos\varphi$.

controlled coalescence of the smaller fragment droplets. The resulting microdroplet size, measured using imaging techniques [35, 70], is controlled by variation of the applied modulation frequency. Modulation frequencies between 3 and 100 kHz are used resulting in droplets between 65 and 20 μm in diameter. Above 100 kHz the interdroplet spacing is on the order of the laser-beam spot size; therefore, in order to produce droplets as small as 16 μm with sufficient spacing, we make use of imperfect coalescence resulting in periodic groups of smaller and bigger droplets.

The droplets travel at 10 m/s through a He-Ne laser light sheet scattering the laser light, which is subsequently detected by a photomultiplier tube and used to trigger the drive laser and the data-acquisition system at 10 Hz. After detection, the droplet is irradiated by a linearly polarized, high-intensity laser pulse from an in-house built Nd:YAG laser system seeded at 1064 nm [73]. The laser system produces a flat-top spatial profile and has temporal pulse-shaping capabilities allowing the production of pulses from 0.4–1000 ns duration. All but the 0.5-ns pulse are box-shaped and their duration is measured as FWHM.

With the purpose of maintaining the homogeneous spatial intensity distribution, the laser beam is imaged from the exit of the amplifier rod onto the droplet. In order

to match droplet and laser-beam spot size, and to reach the necessary intensities on the order of 10^{11} W/cm^2, the laser beam is demagnified to 96 μm FWHM. Of the total laser pulse energy, a fraction of 80% falls within the FWHM area. To obtain an even smaller beam spot size of 56 μm, used for measurements described in Section 1.6, a 3.5-mm aperture is placed in the object plane of the beam. In both cases, the laser-beam spot is slightly elliptical, with less than 25% difference between the major and minor axis, and we use the average value of the two axes. The laser-beam energy is controlled using a combination of a half-wave plate and a thin-film polarizer without affecting the spatial intensity distribution.

The spectral emission of the produced plasma is observed under an angle of 60° (see Fig. 1.1) using a broadband transmission-grating spectrometer [67, 68]. The spectrometer is operated with an entrance-slit width of 25 μm and a 10 000 lines/mm grating obtaining an instrument resolution of 0.1 nm FWHM at 13 nm [67]. The dispersed light is captured by a back-illuminated CCD from Greateyes (GE2048 512BI UV1), cooled to −30 °C to reduce thermal noise.

The measured images are cropped and corrected for shear and tilt introduced by a slight misalignment of slit and grating with respect to the camera pixel array. Afterwards the images are averaged over the non-dispersive axes and the read-out noise and dark counts are eliminated by subtracting a dark exposure image (i.e., an image obtained using the same exposure time but without plasma present). Calibration of the dispersive axis is performed using reference spectra entailing tabulated [74], well-known Al^{3+} and Al^{4+} line features between 11 and 16 nm. The calibration spectra are taken after the experiments by irradiating a solid aluminum target with the Nd:YAG laser at the same position as the droplets. After calibration, the spectra are corrected for second-order contributions in the wavelength range above 11 nm using the second-order diffraction efficiency of the grating [68]. Lastly, the spectra are divided by the first-order diffraction efficiency of the grating as well as the quantum efficiency of the camera. Since the grating transmission is not calibrated below 5.5 nm, all SP values in the following are calculated for a wavelength range of 5.5–25.5 nm. Given the low emission anisotropies observed over the backward half sphere (see below), spectra obtained under an angle of 60° are used for SP.

To obtain an absolute measurement of the produced in-band radiation (13.5 nm ±1%), four silicon photodiode assemblies are mounted under angles of 30°, 42°, 64° and 90° (Fig. 1.1). Photodiode measurements are corrected for their respective solid-angle coverage. These assemblies use Mo/Si multilayer mirrors (MLMs) [10, 40] as found in industrial sources to reflect the in-band part of the radiation onto the photodiodes. Any remaining optical light reflected by the MLMs is subsequently removed by a Si/Zr coating on the photodiodes (SXUV100), which is transmissive for in-band radiation. The response function of all individual components is known, providing a measure of the absolute amount of produced in-band radiation.

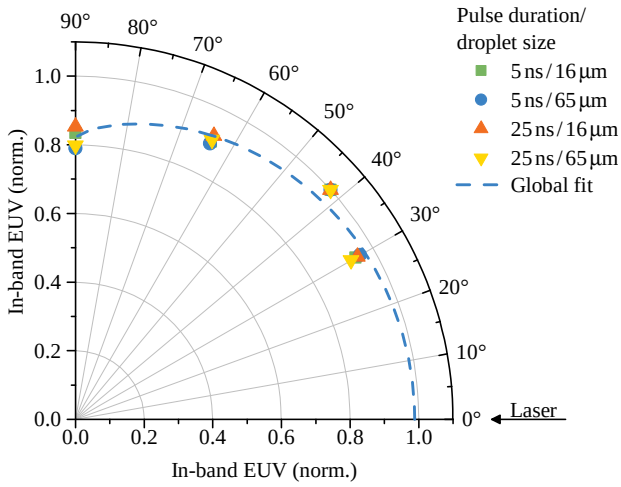

Figure 1.2: Angular dependency (θ) of the in-band emission with respect to the laser-beam axis. Depicted are measurements for the 96-µm laser-beam size. For each pulse duration, the data from the smallest and biggest droplet sizes are shown normalized to their maximum values. The dashed blue line is the result of a global fit of Eq. (1.2).

In order to take into account the emission anisotropy over the backward half sphere where CE is defined, we integrate the angular dependency $f(\theta)$ of the in-band emission. For integration the obtained measurements from the photodiodes in Fig. 1.2 are used, employing the cylindrical symmetry of the system with respect to the laser beam axis

$$\mathrm{CE} \propto \int_0^{\pi/2} d\theta f(\theta) \sin(\theta), \tag{1.1}$$

where the angular dependence $f(\theta)$ of the in-band emission is typically described by (e.g., Refs. [52] and [75])

$$f(\theta) = \alpha + \beta \cos^{\gamma}(\theta). \tag{1.2}$$

Fitting Eq. (1.2) to the measured data, we obtain the following values for the fit parameters: $\alpha = 0.82(2)$, $\beta = 0.17(3)$, and $\gamma = 0.6(3)$. From integration we obtain a value for the anisotropy-corrected CE that is only 5% lower than the value from the photodiode under 30° angle that we use throughout this paper, extrapolated assuming isotropic emission.

1.3 Measurement results

In order to optimize SP and η_{rad}, and therewith CE, we vary three key parameters of our LPP source: laser intensity (see Fig. 1.3), laser pulse duration and droplet size. Following this order, we describe below their impact on the observed spectra and the values of SP and CE as presented in Fig. 1.4. The trends in the radiative efficiency, defined as $\eta_{\mathrm{rad}} \equiv \mathrm{CE/SP}$ are described in Section 1.5. It is preceded by the introduction of a plasma expansion model in Section 1.4 describing the scaling of η_{rad}.

Laser intensity

We start by describing the effect of changing the laser intensity using the example of a 96-μm-sized, 15-ns-long laser-beam pulse and a 46-μm-diameter droplet. The intensity, calculated as $I = E_{\mathrm{L}}/(\tau \pi w^2)$ using the laser pulse duration τ and laser-beam radius $w = \mathrm{FWHM}/2$, is varied over more than 1 order of magnitude in the range of (0.1–2.7) $\times 10^{11}$ W/cm^2 by changing the laser-beam energy. The normalized emission spectra arising from these experimental conditions are shown in Fig. 1.3 and in reduced size in Fig. 1.4(a).

The most prominent characteristic observed in Fig. 1.3 is the shift of the main emission feature from 15 nm toward the desired 13.5 nm with increasing laser intensity. This shift is related to the creation of tin ions of higher charge states (Sn^{8+}–Sn^{15+}) relevant for in-band emission [18, 21, 23, 29]. Additionally, the main emission feature narrows towards higher intensity, reaching a FWHM of 0.9 nm at 1.4×10^{11} W/cm^2.

To resolve which charge states are contributing to in-band emission at a given intensity we look at the short-wavelength emission between 7 and 12 nm. As described in Refs. [20] and [76], Sn^{8+}–Sn^{15+} have unique emission features in this regime stemming from radiative decay out of electronic configurations such as, e.g., the $4p^5\,5s$ in Sn^{14+} where a $4p$ core electron is promoted to the $5s$ subshell. These configuration lie above the in-band contributing $4p^5\,4d^{m+1} + 4p^6\,4d^{m-1}\,4f + 4p^6\,4d^{m-1}\,5p$ (cf. Fig. 1.3). Using such out-of-band features as diagnostics it is evident that for the highest laser intensity (2.7×10^{11} W/cm^2) charge states of at least up to Sn^{15+} are present in the plasma.

The above observations relate to the trend in SP values presented in Fig. 1.4(d) where we see a sharp increase in SP between 0.1 and 0.5×10^{11} W/cm^2. Above 0.5×10^{11} W/cm^2 the incline in SP slows down and SP levels off in the range of (0.8–1.7) $\times 10^{11}$ W/cm^2 before it decreases again. The sharp increase in SP is explained by an increase in average charge state of the plasma causing reduced emission above 16 nm while favoring in-band emission. At the same time the amount of short wavelength radiation (below 12 nm) increases steadily. Nevertheless, SP con-

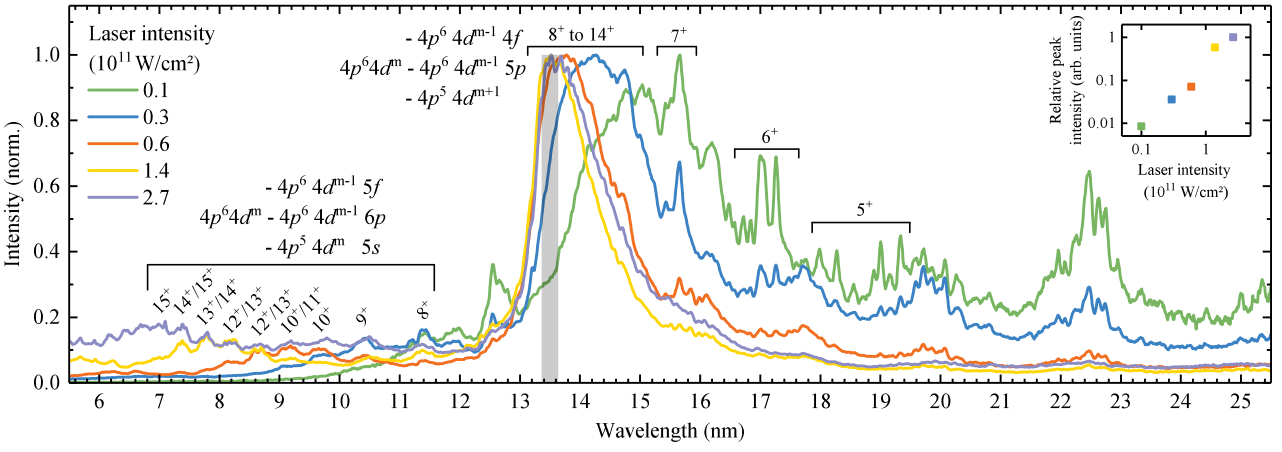

Figure 1.3: Normalized emission spectra for various Nd:YAG laser intensities resulting from a 46-µm-diameter tin droplet illuminated with a 96-µm-sized laser beam of 15-ns duration. The gray-shaded area shows the 2% bandwidth around 13.5 nm, relevant for nanolithographic applications. The emission features attributed to the various Sn ions are labeled with the respective charge-state number. Also labeled are the most relevant transition arrays contributing to the in-band emission and the short-wavelength features between 7 and 12 nm, where m is an integer between 0 and 6 corresponding to Sn^{14+} and Sn^{8+}, respectively [21, 23, 76]. The inset figure shows the relative peak-emission intensities as a function of laser pulse intensity.

tinues rising due to the narrowing of the main spectral feature at 13.5 nm. Above 1.4×10^{11} W/cm^2 SP declines very slowly because the main emission peak stops narrowing while the amount of short wavelength radiation keeps on increasing. At intensities above 1.7×10^{11} W/cm^2 the main feature widens again leading to a more rapid decrease of SP. For the lowest and highest intensities measured an increasing fraction of the emission is outside the measured or calibrated range, respectively, slightly increasing the SP.

Even though SP decreases again at higher intensities, CE monotonically increases over the entire intensity range as shown in Fig. 1.4(d), reaching values up to 1.9%.

Laser pulse duration

In this section we explore the influence of laser pulse duration on the plasma emission as presented in Fig. 1.4(b). For the measurements we chose an intensity of 1.4×10^{11} W/cm^2 at which the main emission feature is narrowest and SP is highest. The droplet diameter as well as the beam size are left unchanged at 46 and 96 μm, respectively.

Upon reducing the laser pulse duration, a narrowing of the main emission peak at 13.5 nm is visible as well as a reduction of the short and long wavelength radiation. The only exception is the pulse duration of 0.5 ns for which the main feature widens again and more emission is observed above 16 nm. For all pulse durations the strong resemblance of the spectra is remarkable indicating that the laser intensity is the pertinent parameter setting the plasma temperature and charge-state distribution. All spectra show similar features and only small differences are visible in the relative emission intensity around 8 nm as well as in the width of the dominant feature at 13.5 nm. The widening of the main emission feature can be attributed to changes in optical depth of the plasma induced by the different plasma sizes for the various laser pulse durations. The larger optical depth causes increased absorption and re-emission of EUV radiation resulting in the observed broadening of the spectral features.

Translating these observations into the SP curve in Fig. 1.4(e), we see an increase in SP from 0.5 to 2.5 ns where it reaches its maximum value. Above 2.5 ns a steady but rather weak decrease from 12% to 8% is visible.

As in the preceding subsection, the measured CE monotonically increases with pulse duration. In the scanned parameter range a relatively high CE of 2.2% is reached at 25 ns.

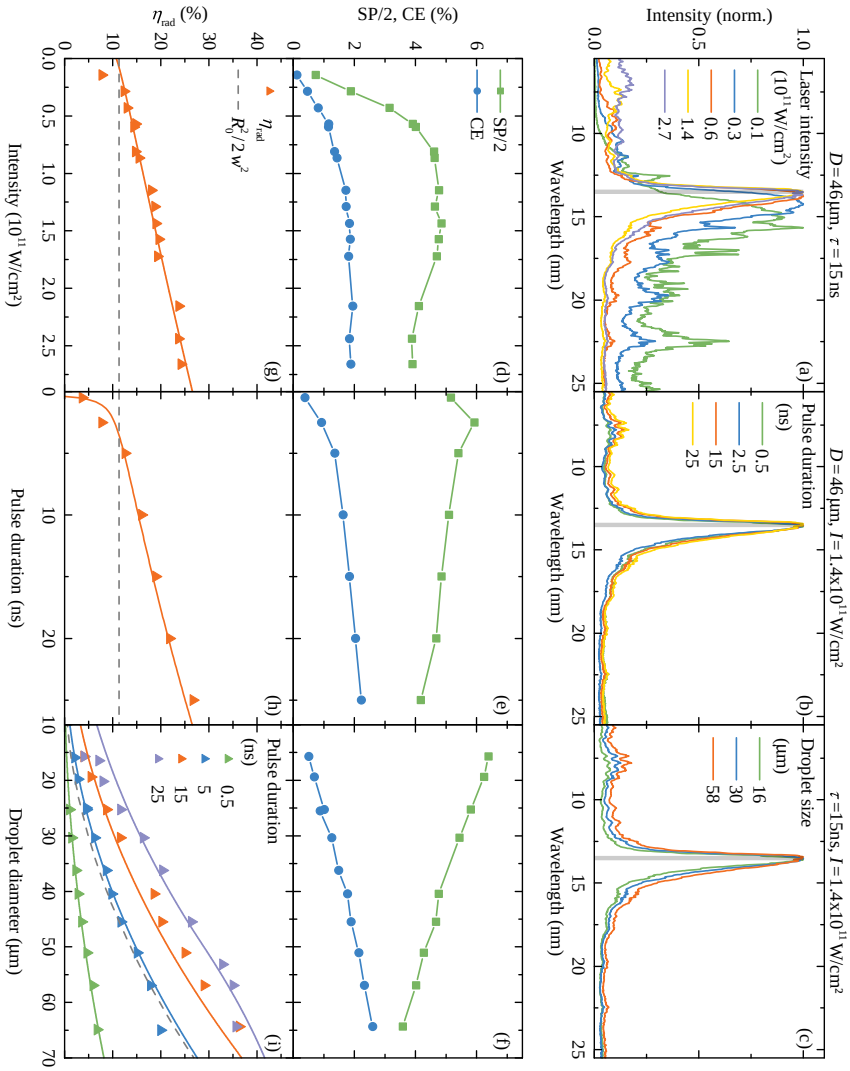

Figure 1.4: Caption on the following page.

Figure 1.4: (Figure on previous page) Top row: spectra for tin microdroplets irradiated by (a) various Nd:YAG laser pulse intensities, (b) laser pulse durations, and (c) droplet sizes. The gray vertical bar depicts a 2% bandwidth around 13.5 nm. Center row: SPs (here divided by a factor 2 for convenience) and CE corresponding to the spectra above. Bottom row: radiative efficiencies ($\eta_{\mathrm{rad}} \equiv$ CE/SP) and the result of a global fit of our plasma expansion model as described in Section 1.5 (solid lines). The gray dashed lines in (g)–(i) depict the geometrical overlap ($R_0^2/2w^2$) of laser beam and droplet for isotropic emission.

Droplet size

Lastly, we show the effect of a change in droplet diameter onto the spectral emission in Fig. 1.4(c). For the measurements shown a pulse duration of 15 ns was used at an intensity of 1.4×10^{11} W/cm^2. Enlarging the droplet diameter leads to increased relative emission at wavelengths below 13 nm while all spectra show strong similarity with respect to their emission features. Again, predominantly the width of the main emission feature varies and its change can be attributed to changes in the optical depth of the plasma.

Looking at SP in Fig. 1.4(f), we find a steady decline from 13% at 16 μm to 8% at 58 μm diameter. Once more, in contrast to the scaling of SP, CE monotonically increases over the entire range of droplet diameters.

1.4 Plasma expansion model

For all cases presented in Fig. 1.4, CE increases monotonically with the scanned parameter, even when SP declines. This behavior can be understood as an increase in radiative efficiency that counteracts the losses in SP for bigger droplets and longer pulses. To describe the changes in radiative efficiency with respect to laser intensity, pulse duration, and droplet radius we develop a model taking into account the increase in laser light absorption due to plasma expansion during the laser irradiation.

In the model, η_{rad} is proportional to the absorbed laser light assuming that a constant fraction is lost to plasma kinetics. At time t_0 when the laser pulse arrives at the droplet the absorbed laser light fraction equals the spatial overlap of droplet and laser beam. At the intensities used, reflectivity can be neglected, resulting in full absorption within the overlap region [70].

The absorbed laser light leads to ablation and plasma creation beyond a certain threshold laser intensity [35, 70]. This plasma expands establishing a radial density gradient around the droplet [70] (see Fig. 1.5). All laser light is absorbed close to an electron density that is of the order of, but below, the critical electron density

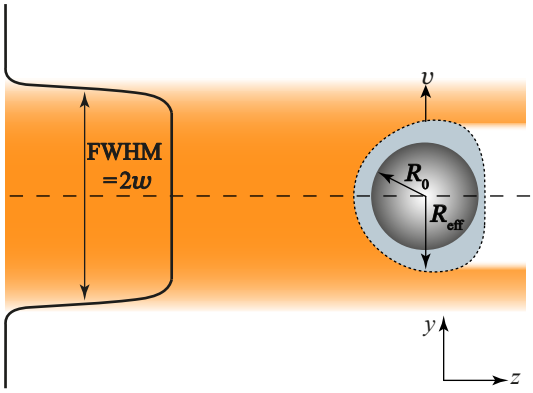

Figure 1.5: Schematic representation of the laser-produced plasma system. The laser pulse (orange shaded area) propagating in positive z direction is absorbed by the liquid Sn droplet of radius R_0 (gray sphere). During laser irradiation plasma is created around the droplet (light gray shaded area) increasing the absorbing area. The latter expands with a constant velocity v laterally to the laser-beam propagation direction, increasing the effective radius of absorption to $R_{\mathrm{eff}} = R_0 + vt$.

for the Nd:YAG laser wavelength ($n_c = 1 \times 10^{21}\,\mathrm{e}^-/\mathrm{cm}^3$) [41]. With time, the density contour at which laser light is absorbed moves outwards and the absorptive area increases. Analogously to Refs. [35] and [77], we introduce a power law, here for the lateral expansion speed $v(I) = a \times I^b$, at which this density contour moves outwards. The expansion speed is constant over the duration of the laser pulse. Before the plasma can efficiently emit radiation it needs to be heated to reach the relevant plasma temperatures. During this time no significant amount of in-band radiation is emitted implying a lowering of the radiative efficiency. To capture this effect a plasma heat-up time t_h is introduced as a multiplicative factor $(1 - t_h/\tau)$ following Ref. [78], where τ is the laser pulse duration. To account for the fraction of laser energy lost to plasma kinetics and into radiation emitted towards the forward-facing half sphere, we introduce the maximal radiative efficiency η_{max}.

Next, we divide the calculation into three cases: (i) $R_0 + v\tau \leq w$; (ii) $R_0 + v\tau > w$; (iii) $R_0 \geq w$. In case (i), the droplet is initially smaller than the beam and the absorbing area expands during the laser irradiation, but will not exceed the laser-beam size during the pulse. In case (ii), the droplet is smaller than the beam but the absorbing surface exceeds the laser-beam size before the laser pulse ends. In this case we neglect any expansion beyond time $t_w = (w - R_0)/v$ when the absorbing surface exceeds the laser beam because from thereon full overlap of laser and plasma is reached. In the most extreme case (iii), the liquid droplet

itself is already larger than the beam leading to unity absorption during the entire laser pulse duration. These considerations lead to the following smooth, continuous global fit function:

$$\eta_{\mathrm{rad}} = \left(1 - \frac{t_h}{\tau}\right)\eta_{\max} \times \begin{cases} \dfrac{\frac{1}{3}v^2\tau^3 + R_0 v\tau^2 + R_0^2\tau}{w^2\tau} & \text{(i)} \\ \dfrac{\frac{1}{3}v^2 t_w^3 + R_0 v t_w^2 + R_0^2 t_w}{w^2\tau} + \dfrac{\tau - t_w}{\tau} & \text{(ii)} \\ 1 & \text{(iii)} \end{cases} \tag{1.3}$$

There are only three main free fit parameters, being $\eta_{\max}$, t_h, and v, where the latter is, in turn composed of two free fit parameters a and b (relevant only for the laser-intensity dependency).

1.5 Model fit and discussion

The obtained radiative efficiencies are presented in Fig. 1.4(g)–1.4(i) and our model can be used to understand the monotonous nature of their rise with all varied parameters. The result of a single, *global* fit of our model (see Eq. (1.3)) to all experimental data related to the variation of the laser pulse duration and droplet diameter is depicted in Fig. 1.4(h) and 1.4(i), where all data is taken at a constant intensity of $1.4 \times 10^{11}\,\mathrm{W/cm^2}$. An excellent agreement between model and experiment is obtained. From the fit a plasma expansion velocity $v = 0.9(1)\,\mu\mathrm{m/ns}$, a maximal radiative efficiency of $\eta_{\max} = 49(2)\,\%$ and a plasma heat-up time $t_h = 0.34(2)\,\mathrm{ns}$ are retrieved. The radiative efficiency from the geometrical laser-droplet overlap, without considering the expanding plasma, is given by $R_0^2/2w^2$ for isotropic emission shown as dashed lines in Fig. 1.4(g)–1.4(i).

The plasma heat-up time t_h agrees well with the 0.4 ns calculated in Ref. [79] for Nd:YAG-produced Sn plasmas of about 30-eV temperature. However, further transient effects in the plasma due to, e.g., the finite rise and fall times that are a dominant part of the shortest pulse, cannot be excluded. Given its small, sub-ns value, t_h has negligible impact on radiative efficiency except for the shortest, 0.5-ns pulse-duration case.

The fitted value of the maximal radiative efficiency of 49% (with a highest experimentally obtained value of approximately 35%) comes close to the maximally possible value of 50% in the case of isotropic emission. As energy is invariably lost through other processes such as ionization and plasma kinetics, we conclude that a finite anisotropy conveniently causes a preferred emission of light into the backwards half sphere as also indicated, e.g., in Ref. [66].

O'Shay *et al.* [71] estimated the total amount of radiated energy from a tin LPP in 4π steradian to be on the order of 90% of the absorbed laser energy. Tillack *et al.* [72] simulated the energy balance of spherical tin targets and concluded that about 70% of the energy is converted into radiation. This is in broad agreement with the 70–80% estimate from the simulations presented in Ref. [70]. Combining our fit value with this approximately 80% theory value we conclude that approximately 30% of the laser light is converted into radiation emitted in the forward half sphere. The in-band emission anisotropy in Fig. 1.2 also evidences a slight preference for backward emission. These findings are further supported by Refs. [64] and [65]. Our CE results are consistent with those obtained in Ref. [64] taking into account the droplet and beam spot sizes used.

The expansion velocity obtained from the fit agrees well with those inferred from radiation hydrodynamic simulations [70]. In that work, a 46-μm-diameter droplet was irradiated by a 115-μm FHWM Gaussian Nd:YAG laser beam at an average intensity of 1.3×10^{11} W/cm^2. A dominant, 80% fraction of the laser light is absorbed in the region close to but before the critical surface [41]. Lateral expansion speeds on the order of $v \sim 1$ μm/ns resulted from the simulations for densities approximately (0.1–0.5)n_c.

Using the global fit values for η_{max} and t_h, we next apply and fit our model to the laser-intensity dependency in Fig. 1.4(g). Again, an excellent agreement is found between model and experiment, obtaining the parameter values $a = 0.69(5)$ and $b = 0.8(1)$. This near-linear dependence of v on I is in line with the simulation data underpinning Ref. [70]. We note that t_h may also depend on intensity but its contribution to the 15-ns pulse-duration case is marginal and completely removing t_h from Eq. (1.3), in fact, does not significantly change the obtained values for the expansion velocity parameters a, b.

In conclusion, we can describe the scaling of the radiative efficiency with all studied parameters by a model describing the increase of laser absorption with plasma expansion. Excellent overall agreement between model and experimental data is obtained. We note that in our current investigations the effective radius $R_{eff} = R_0 + v\tau$ remained below the beam radius w corresponding to case (i) in Eq. (1.3). The finite ellipticity of the laser-beam spot is not expected to significantly influence the measurements as the plasma expansion does neither exceed minor nor major axis. Values above our experimental maximum of 35%, possibly nearing 50%, appear to be feasible. Thus, in order to obtain high CE, a set of parameters needs to be found where a high value for SP is achieved while optimizing the absorbed fraction of laser light, or radiative efficiency. Changing the beam size in the following section enables us to probe beyond model case (i) and maximize radiative efficiency.

1.6 Increasing radiative efficiency

In order to increase the radiative efficiency, and with it CE, the laser-beam size is reduced to 56 μm. As before, the beam-to-droplet overlap is scanned by changing droplet size (Fig. 1.6). The laser intensity is set to an optimal 1.4×10^{11} W/cm^2 for SP and the laser pulse duration to 15 ns. The spectra for the small beam spot size in Fig. 1.6(a) show a small but significant broadening of the main emission feature on its long wavelength side with a corresponding systematic reduction of SP in Fig. 1.6(b). This may be related to an absence of heating of the outer plasma layers beyond 56 μm.

A considerable overall increase in CE is obtained for all droplet sizes. It monotonically rises with the droplet diameter reaching a record-high value of 3.2%. We note that the ever more slowly decreasing values for SP/2 and increasing CE appear to converge to a common value. This intriguing observation indicates that the limit CE ≤ SP/2, strictly valid only for isotropic emission [69], may provide a good estimate for the maximally reachable CE value of the plasma source.

Over the entire range measured, the radiative efficiency is monotonically increasing and significantly higher than for the 96-μm laser beam (see Fig. 1.6(c)). Comparing the small-beam measurements to the model results of Section 1.5, we plot Eq. (1.3) using the values for v and t_h as determined from the global fit in Fig. 1.4. We set the beam spot size to 56 μm leaving only η_{rad} as a free fit parameter. The model fit shown with the dashed-dotted line in Fig. 1.6(c) is in excellent agreement with the experimental data. The obtained value for $\eta_{\mathrm{max}} = 42(1)\%$ is slightly lower than before, although within systematic uncertainties of determining beam spot and droplet size. The regime probed by these small-beam measurement includes model cases (ii) and (iii) that are not reachable in Section 1.5. In these cases, the laser beam does not directly heat the laterally expanding high-density plasma at radii $R_{\mathrm{eff}} > w$, which may affect η_{rad} through differences in the energy partitioning between forward and backward emission, and plasma kinetics. Further, the finite ellipticity of the laser-beam spot may slightly influence the measurements as the plasma expansion in these cases (ii) and (iii) exceeds major and minor axis over the scanned parameter range.

Aside from the already explored reduction of laser beam-spot and increase of droplet size to improve η_{rad}, our model shows that laser pulses of even longer duration could also be employed to compensate for a geometrical mismatch. For all three solutions, increases in η_{rad} are partially offset by a decrease in SP. Given the limit conditions CE ≤ SP or the apt CE ≤ SP/2, any global approach to source optimization needs to maximize both SP and the laser-plasma overlap captured by η_{rad}. Based on these considerations and our spectroscopic measurements in Fig. 1.6(a) from which we obtain values for SP above 12%, conversion efficiencies of CE = SP/2 = 6% may in fact be achievable. These values would rival those of cur-

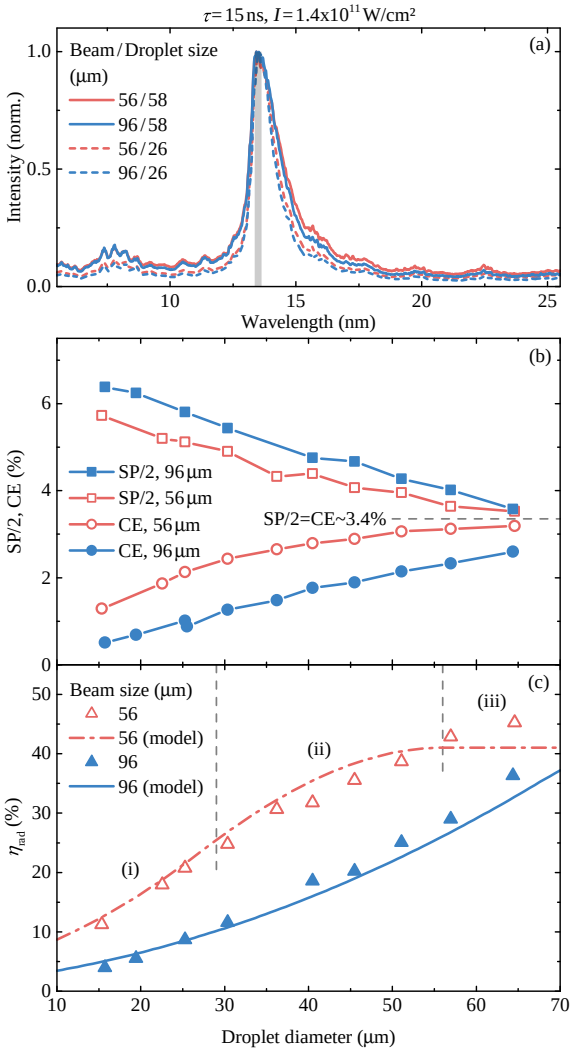

Figure 1.6: (a) Spectra for two droplet sizes and two laser-beam sizes (see main text) at a laser intensity of 1.4×10^{11} W/cm^2; (b) values for SP/2 and CE versus droplet diameter for the two laser-beam sizes; (c) radiative efficiency versus droplet diameter for the two laser-beam sizes. The dash-dotted and solid lines represent the model curves. For the 56-μm laser beam, the regimes corresponding to the three model cases (i)–(iii) of Eq. (1.3) are highlighted by the vertical dashed lines (see main text).

rent CO_2-laser-driven sources. To obtain such efficiencies, the observed systematic decrease of SP with decreasing beam size needs to be negated. The model points towards another class of solutions including maximizing η_{rad} by using a separate laser 'pre-pulse' to predeform the microdoplet into a disk shape [11, 33–39] that closely matches the applied 'main' laser beam-spot size.

1.7 Conclusion

We experimentally investigate the emission of EUV light from Nd:YAG laser-produced plasma over a wide parameter range, varying the laser energy, its pulse duration, and the size of the tin microdroplets. Spectroscopic measurements combined with absolute measurements of the emission into a 2% bandwidth around 13.5 nm allow us to obtain the scaling of three coupled parameters: the spectral purity SP, the conversion efficiency CE, and the radiative efficiency η_{rad} expressed as the ratio CE/SP. We successfully capture all observed scalings of η_{rad} in a geometrical model featuring the plasma absorption length as the pertinent parameter. Using a smaller laser-beam spot size, approaching the size of the droplets, we obtain a record-high 3.2% conversion efficiency of laser light into in-band radiation. Energy conservation considerations bind the maximum value of CE to SP/2 for isotropic emission, and our measurements strongly hint at the convergence of CE towards this theoretical limit. A 6% conversion efficiency value may thus be achievable in future experiments that should also quantify and compare the debris produced by Nd:YAG laser-produced plasma sources to industrial ones using CO_2 lasers. High values for the key parameter, the conversion efficiency, are indeed obtainable from a single 1-μm-laser-pulse irradiation scheme. Combining these high conversion efficiency values with the advantages of reduced footprint, beneficial wall-plug efficiency, and laser stability this work enhances the prospects that Nd:YAG-driven LPP light sources will find application in EUV nanolithography.

2 | Radiation transport and scaling of optical depth in Nd:YAG laser-produced microdroplet-tin plasma

R. Schupp, F. Torretti, R. A. Meijer, M. Bayraktar, J. Sheil, J. Scheers, D. Kurilovich, A. Bayerle, A. A. Schafgans, M. Purvis, K. S. E. Eikema, S. Witte, W. Ubachs, R. Hoekstra, and O. O. Versolato

Applied Physics Letters **115**, 124101 (2019)

Experimental scaling relations of optical depth are presented for the emission spectra of a tin-droplet-based, 1-μm-laser-produced plasma source of extreme ultraviolet (EUV) light. The observed changes in the complex spectral emission of the plasma over a wide range of droplet diameters (16–65 μm) and laser pulse durations (5–25 ns) are accurately captured in a scaling relation featuring the optical depth of the plasma as a single, pertinent parameter. The scans were performed at a constant laser intensity of 1.4×10^{11} W/cm^2, which maximizes the emission in a 2% bandwidth around 13.5 nm relative to the total spectral energy, the bandwidth relevant for industrial EUV lithography. Using a one-dimensional radiation transport model, the relative optical depth of the plasma is found to linearly increase with droplet size with a slope that increases with the laser pulse duration. For small droplets and short laser pulses, the fraction of light emitted in the 2% bandwidth around 13.5 nm relative to the total spectral energy is shown to reach high values of more than 14% which may enable conversion efficiencies of Nd:YAG laser light into—industrially—useful EUV radiation rivalling those of current state-of-the-art CO_2-laser-driven sources.

2.1 Introduction

The semiconductor industry is currently moving from deep-ultraviolet to extreme ultraviolet (EUV) lithography for high-volume manufacturing of the next generation of microelectronics where the shorter wavelength of the EUV radiation enables further miniaturization. The light sources of choice for the nanolithographic applications are laser-produced plasmas (LPPs) [11, 18–32, 80–82]. In these sources, tens-of-micrometer-sized tin droplets are irradiated by high-intensity (10^{10} W/cm^2) laser pulses, in order to generate a high-density (10^{19} e$^-$/cm^3) plasma that efficiently emits EUV radiation [83]. Tin is used because several of its charge states have strong dipole transitions such as the $4d$–$4f$, $4p$–$4d$, and $4d$–$5p$ arrays in Sn^{8+}–Sn^{15+} which strongly emit around 13.5 nm [18, 27], a wavelength that matches the peak reflectivity of available Mo/Si multilayer optics [10, 40] used in state-of-the-art EUV-lithography. The light of interest within a 2% bandwidth around 13.5 nm is referred to as *in-band* radiation.

Currently, CO_2-gas lasers operating at 10 μm wavelength are used to drive the EUV-emitting plasma, but with further developments regarding their output power, YAG solid-state lasers operating at 1 μm may become a viable alternative in the future. YAG laser systems provide a smaller footprint, a significantly higher efficiency in converting electrical power to laser light, and excellent temporal pulse shaping capabilities. The shorter 1 μm wavelength of YAG lasers gives rise to a 100 times higher critical plasma density ($n_{\mathrm{crit}} \propto \lambda^{-2}$) compared to CO_2-laser-driven plasmas, and higher laser intensities of typically 10^{11} W/cm^2 are needed to efficiently produce in-band radiation. The higher critical density results in a much higher, nearly complete absorption of the laser light by the tin target through the mechanism of inverse bremsstrahlung [42, 69]. A possible adverse effect of the higher critical plasma density is the creation of EUV radiation in plasma regions of higher density and high opacity. Significant self-absorption of the emitted radiation can lead to a broadening of the spectral emission out of the 2% bandwidth of interest, thus reducing the spectral purity (SP) of the EUV plasma source [44–47]. SP is defined as the ratio of in-band energy ($E_{\mathrm{IB},2\pi}$) over the total EUV energy ($E_{\mathrm{rad},2\pi}$) emitted into the hemisphere back toward the laser that is covered by multilayer optics in industrial sources. Conversion efficiency CE is defined as the ratio of the total produced in-band energy $E_{\mathrm{rad},2\pi}$ and the total incident laser energy. Considering conservation of energy, SP represents the absolute upper limit to the conversion efficiency: CE $\leq$ SP, where CE approaches SP only if all light is emitted in the backward-facing 2π steradian and no laser energy is converted into other energy channels such as kinetic energy of charged particles [84]. A more stringent limit of CE $\leq$ SP/2 is found in the case of spherically symmetric emission [69]. Given the importance of SP as indicator for source performance, its scaling with relevant source parameters such as tin-droplet size, laser pulse duration and laser beam spot size needs to be

quantified and understood. The existing literature on Nd:YAG-laser-driven plasma from high-purity tin microdroplets [64–66], the industrial targets of choice, mainly focuses on the integrated amount of produced in-band emission rather than on the spectral properties of the plasma, despite the importance of SP.

In this Letter, a systematic study of the influence of droplet size and laser pulse duration on the emission spectrum of a droplet-based, Nd:YAG-driven EUV source is presented. An analytical solution for radiation transport in an optically thick one-dimensional plasma is used to quantify opacity driven broadening of key emission features.

2.2 Experiment

In the experiment, spherical micrometer-sized liquid tin droplets were irradiated with high-intensity laser pulses from a Nd:YAG laser system[73] operated at 1064 nm as described in Ref. [35] and [84]. The laser pulse was temporally box shaped and of adjustable duration. It had a spatially flat-top shape of 96 μm diameter to homogeneously heat the plasma. The spectral emission from the plasma was observed with a transmission grating spectrometer [68] under 60° with respect to the incoming laser beam. The measured spectra were corrected for the grating's first and second order diffraction efficiency as well as for the quantum efficiency of the camera. After correction, the SP values were calculated with respect to the measured spectral range of 5.5–25.5 nm. The wavelength was calibrated in a separate experiment using atomic line emission from an aluminum plasma. Using a laser intensity of 1.4×10^{11} W/cm^2 at which SP is optimal [84], two sets of experiments were conducted.

First, spectra were measured for several laser pulse durations within the range of 5–25 ns while keeping the droplet size fixed at 46 μm. As seen in Fig. 2.1(a), the main emission feature at 13.5 nm broadens for longer laser pulse duration, while all other spectral emission features stay remarkably similar even though the laser pulse duration was varied by a factor of five. This indicates that laser intensity is the pertinent parameter of the investigated LPP determining charge state distribution and temperature of the plasma [84, 85].

Second, spectra were measured for various droplet sizes in the range of 16–65 μm at constant laser pulse durations of 5, 15 and 25 ns. Spectra for the 15-ns case are shown in Fig. 2.1(b). A striking similarity in spectral structure is observed among plasmas formed on droplets of various sizes. With increasing droplet size, the main spectral feature at 13.5 nm broadens and the short-wavelength radiation between 5.5 and 12 nm increases in intensity relative to the main emission feature.

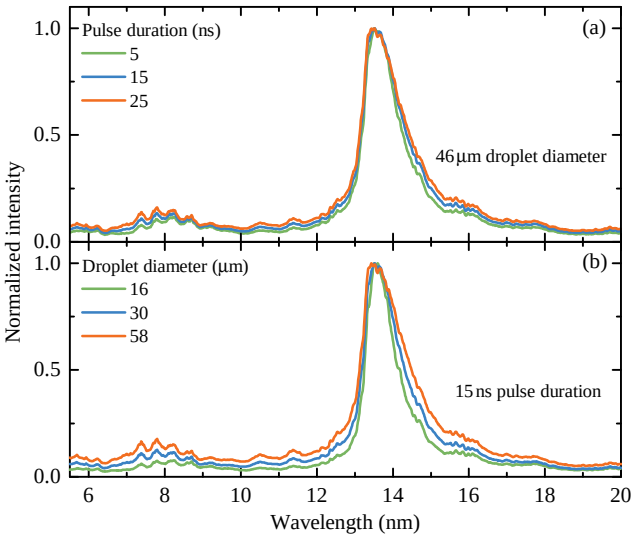

Figure 2.1: Selection of emission spectra of Nd:YAG-laser-produced plasma from tin microdroplets irradiated at a constant laser intensity of $I = 1.4 \times 10^{11}\,\mathrm{W/cm^2}$ while varying either (a) the laser pulse duration or (b) the droplet diameter.

2.3 Methods

The observed broadening of spectral features for increased pulse duration and droplet size, illustrated in Fig. 2.1, can be connected to an increase in the optical depth of the emitting plasma. The spectral radiance L_λ of a plasma with significant absorption and re-emission can be calculated using the equation of radiation transport. The subscript λ indicates the wavelength dependency of L_λ. The solution for a homogeneous one-dimensional plasma can be given in analytic form [86]

$$L_\lambda = S_\lambda \left(1 - e^{-\tau_\lambda}\right), \tag{2.1}$$

where $S_\lambda = j_\lambda/\alpha_\lambda$ is the source function defined by the ratio of emissivity j_λ and the absorptivity α_λ. Opacity is given by $\kappa_\lambda = \alpha_\lambda/n_\mathrm{i}$, where n_i is the ion density. In local thermodynamic equilibrium (LTE), where the atomic levels are thermally populated, the source function S_λ equals the Planck blackbody function B_λ. We assume that such LTE holds for the high-density, strongly collisional Nd:YAG-driven plasma. In the exponent, τ_λ is the wavelength-specific optical depth given by $\tau_\lambda = \int \alpha_\lambda dx$, where the absorptivity α_λ is integrated over the plasma length. Rearranging Eq. (2.1) the optical depth of the observed plasma can be obtained from its spectral radiance via

$$\tau_\lambda = -\ln\left(1 - \frac{L_\lambda}{B_\lambda}\right), \tag{2.2}$$

with the relative spectral radiance L_λ/B_λ. The optical depth of plasmas of same temperature and density can only differ by a wavelength-independent factor a_i, here referred to as the relative optical depth, relating the plasmas' optical depths via $\tau_{\lambda,i} = a_i\,\tau_{\lambda,0}$. It follows from Eq. (2.2) that

$$\frac{L_{\lambda,i}}{B_\lambda} = 1 - \left(1 - \frac{L_{\lambda,0}}{B_\lambda}\right)^{a_i}. \tag{2.3}$$

It is instructive to use Eq. (2.3) to interpret the observed spectral changes, hypothesizing that plasma length scale is the pertinent parameter. At the wavelength λ_p of peak radiance near 13.5 nm, the optical depth typically has high values as follows from the work of Colgan *et al.* [29]. Their calculation results indicate a peak opacity value of $\sim 5 \times 10^5$ cm^2/g at a relevant 0.01 g/cm^3 ion density. Thus, taking a reasonable 20 μm plasma length [69], we deduce a typical value $\tau_{\lambda_p} \approx 10$. Next, as the plasma is heated under conditions of a spatially homogeneous laser illumination at constant intensity we can ascribe to it a single, constant temperature. The entire plasma surface thus has a radiance L_{λ_i} (in units of W sr^{-1} m^{-2} Hz^{-1}) that is constant over the duration of the laser pulse. The observed spectra $O_{\lambda,i}$ can be related to L_{λ_i} by further realizing that an opaque plasma will have a spectral radiance equal to that of a blackbody $B_{\lambda,p}$ as here at 13.5-nm wavelength ($\tau_{\lambda_p} \approx 10$). Thus, we equate $O_{\lambda,p}/B_{\lambda,p} := 1 = L_{\lambda,p}/B_{\lambda,p}$.

Using Eq. (2.3) any spectrum can be expressed in terms of any other spectrum via the relative optical depth a_i. The value of a_i can be obtained with respect to a chosen reference spectrum from a fit of Eq. (2.3) to the relative spectral radiance $L_{\lambda,i}/B_\lambda$. As reference, for which $a_i = 1$, the relative spectral radiance $L_{\lambda,0}/B_\lambda$ of the spectrum with the narrowest main emission feature is used in the following, i.e., the one measured at 5 ns pulse duration and 16 μm droplet size. Typical literature values for the electron temperatures at which Nd:YAG LPPs most efficiently emit in-band radiation vary between 28 and 40 eV [29, 69, 79, 87]. A temperature in the center of this range of 34 eV is chosen for B_λ for all spectra. A common temperature is used because the laser intensity, which sets the effective plasma temperature, remains constant for all measurements. Variation of the blackbody temperature within the stated limits changes the fitted relative optical depth (see below) by less than 3%.

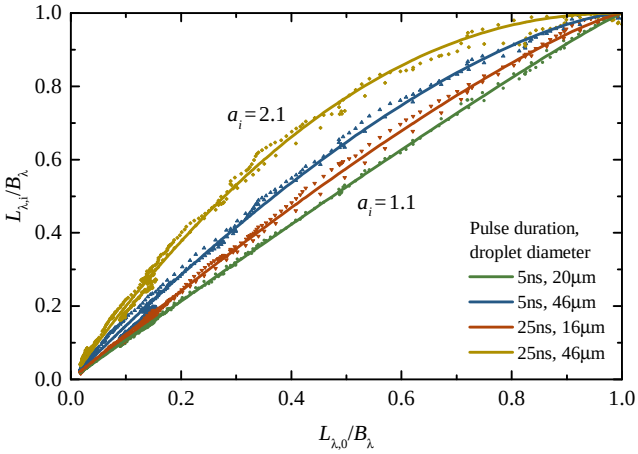

Figure 2.2: Relative spectral radiance $L_{\lambda,i}/B_\lambda$ of experimental spectra taken at constant laser intensity but various laser pulse durations and droplet sizes (cf. Fig. 2.1). The relative spectral radiances are plotted as dotted curves with respect to the one of a reference spectrum $L_{\lambda,0}/B_\lambda$ obtained at 5 ns laser pulse duration and 16 µm droplet diameter where the main emission feature at 13.5 nm is narrowest. For the blackbody function B_λ a temperature of 34 eV was used. The solid lines depict fits of Eq. (2.3) to the data featuring the relative optical depth a_i as single free fit parameter.

2.4 Results

Fig. 2.2 shows example data for $L_{\lambda,i}/B_\lambda$ versus $L_{\lambda,0}/B_\lambda$ for a wide range of droplet sizes and pulse durations. Excellent agreement of data and model fit is observed, featuring the relative optical depth a_i as single free fit parameter.

The values of the relative optical depth a_i as obtained from the procedure shown in Fig. 2.2 enable reproduction of spectra measured for other droplet sizes and laser pulse durations by radiation transport of the reference spectrum. Inserting the relative optical depth obtained from the fits into Eq. (2.3) and multiplying by B_λ leads to an excellent reproduction of experimental spectra as seen in Fig. 2.3(a) and 2.3(b). This is especially true for the main emission feature around 13.5 nm. When comparing the transported spectrum in the short-wavelength region between 5 and 12 nm, minor differences are visible. The differences are very small for increasing pulse duration in Fig. 2.3(a) and become slightly more pronounced for increasing droplet size in Fig. 2.3(b). This may be explained by changes in the plasma other than a simple linear optical depth such as emission from a multitemperature plasma or a slight dependence of plasma charge state distribution with droplet size and pulse

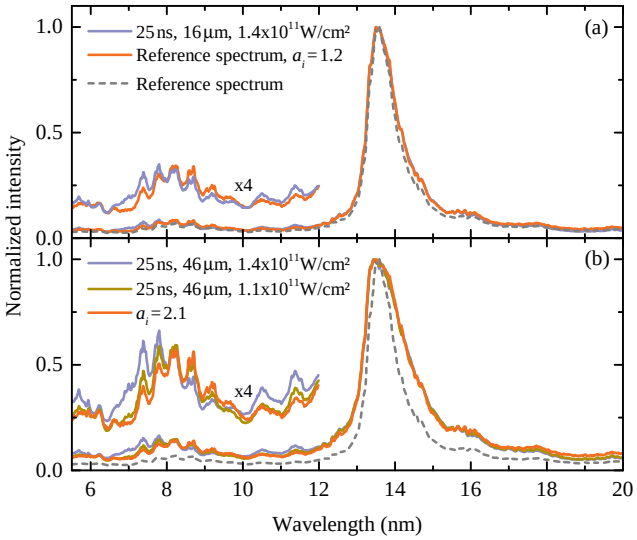

Figure 2.3: Comparison of the reference spectrum and radiation transported reference spectrum with the measured spectra. The reference spectrum was transported using Eq. (2.3) together with the relative optical depth as determined in Fig. 2.2. (a) Increasing laser pulse duration (b) Increasing laser pulse duration and droplet size. An additional spectrum is shown measured at lower laser intensity of 1.1×10^{11} W/cm^2 providing a better match with the radiation transported spectrum in the 5–12 nm range.

duration. Comparison of the relative intensities of the short-wavelength features suggests that the average charge state slightly increases with droplet size [76, 84]. To account for a possibly higher average charge state of the plasma at longer pulse duration and larger droplet size, the scaled reference spectrum may instead be compared to spectra taken at lower laser intensity. Indeed, comparing to spectra taken at a laser intensity of 1.1×10^{11} W/cm^2 shows excellent agreement over the entire spectral range measured. We thus observe that the short-wavelength band between 5 and 12 nm is a much more sensitive probe to the emission properties of Sn LPPs than the main emission feature at 13.5 nm.

In Fig. 2.4(a) the fitted values for spectra of all pulse durations and droplet sizes are summarized. The relative optical depth a_i appears to scale linearly with droplet radius and to strongly depend on the pulse duration. Linear fits are in good agreement with the data and converge to a common intercept of ∼0.7 at zero droplet diameter. The slope coefficients monotonically increase with pulse duration from 0.017 to 0.025 and 0.030 µm^{-1} for 5, 15 and 25 ns, respectively.

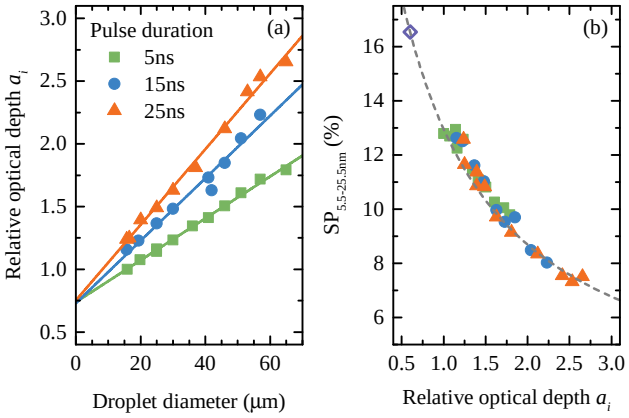

Figure 2.4: (a) Dependency of the relative optical depth a_i on the droplet diameter for various laser pulse durations as obtained, e.g., in Fig. 2.2. The solid lines show a linear extrapolation of the data toward zero droplet size. (b) Experimental values for spectral purity ($SP_{5.5-25.5nm}$) versus relative optical depth. The dashed line represents $SP_{5.5-25.5nm}$ as calculated from the radiation transported reference spectrum. The open diamond symbol indicates the $SP_{5.5-25.5nm}$ value of the radiation transported reference spectrum for a relative optical depth parameter $a_i = 0.6$, a value obtained from comparison of the radiation transported reference spectrum with the emission of the CO_2-laser-driven plasma as shown in Fig. 2.5 (see text).

Having identified the optical depth as the pertinent scaling parameter for Nd:YAG-laser-produced tin plasmas the spectral purity of the emission spectrum is related to it in Fig. 2.4(b). Using this scaling all experimental $SP_{5.5-25.5nm}$ values, calculated over a range of 5.5–25.5 nm as denoted in the subscript, collapse onto the gray dashed curve obtained by calculating the $SP_{5.5-25.5nm}$ of the radiation transported reference spectrum.

It is instructive to compare the $SP_{5.5-25.5nm}$ scaling captured by the gray dashed curve with the SP value of spectra from a state-of-the-art, CO_2-laser-driven EUV source. Such CO_2-laser-driven plasmas may be expected to have small optical depths $\tau < 1$ and thus less broadening, considering the 100-fold decrease in critical density compared to the Nd:YAG case. These CO_2-laser-driven sources are, in general, characterized by relatively high SP and CE values. The spectrum was obtained (see Fig. 2.5) by pre-deforming a droplet by a low-intensity CO_2 laser *pre-pulse*, leading to a disk-shaped target of approximately 200 μm in diameter. The flat target was subsequently irradiated by a high-intensity, 100 ns, 320 mJ *main pulse* with a beam size that matched the target to produce EUV radiation. In this

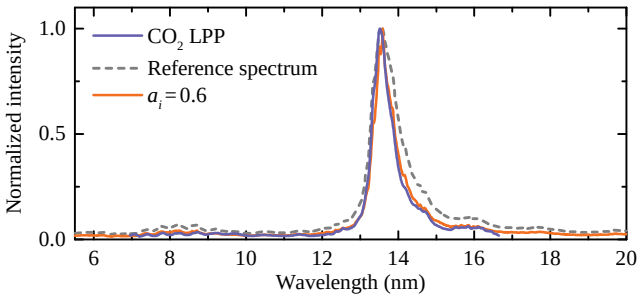

Figure 2.5: Comparison of the transported reference spectrum using Eq. (2.3) with $a_i = 0.6$ and the spectral emission from a CO_2-laser-driven plasma.

case, the spectrum was taken over a wavelength band spanning 6.8–16.7 nm. The fraction of light emitted in the 2% bandwidth around 13.5 nm relative to the total spectral energy in this measured bandwidth is $SP_{6.8nm-16.7nm} = 23\%$. For a relative optical depth $a_i = 0.6$, the Nd:YAG reference spectrum is found to closely match this $SP_{6.8nm-16.7nm}$ performance (also see Fig. 2.5). Over the extended wavelength band of 5.5–25.5 nm that defines SP in this work, this scaled Nd:YAG LPP spectrum has $SP_{5.5-25.5nm} = 16.5\%$ (open diamond symbol in Fig. 2.4(b)). The reference spectrum for $a_i = 0.6$ closely resembles the CO_2 spectrum. This is a remarkable finding as the plasma conditions for the two cases are vastly different and the conditions of LTE and $\tau \gg 1$ required for the procedure outlined in this work are not met for the CO_2 case.

Calculating the maximally obtainable conversion efficiency via $CE = SP/2$ [69, 84] a significantly higher CE value is expected for CO_2-driven LPPs, given its higher SP. However, accounting for the fraction of laser light ϵ absorbed by the tin target—near unity (> 0.9 [70]) for the case of 1 µm radiation, while about 0.7 for 10 µm light [88]—both drive laser cases may indeed have about the same conversion efficiency limit of $CE = \epsilon SP_{5.5-25.5nm}/2 \approx 6\%$ making 1 µm solid-state lasers a viable alternative as source drive lasers. Naturally, the maximum obtainable CE depends not only on the emission spectrum as there are further significant contributions to the total energy balance, aside from a finite emission anisotropy. Examples include plasma kinetics, ionization energy, as well as contributions from plasma emission outside the 5.5–25.5 nm range. A careful comparison of this total energy balance is required between the CO_2 and Nd:YAG drive laser cases. Further, a central requirement is the creation of manageable amounts of debris from the plasma. This entails, among others, fragments or high-energy particles that could reduce optics lifetime. Laser energy not contributing to radiation may instead lead to the production of fast ionic debris and possible gains in spectral purity and radiative output

power should be carefully weighed out against, e.g., increases in the tin load on the optical components. A full quantification of the loads of various debris is left for future work.

2.5 Conclusion

In conclusion, optical depth is established to be the pertinent scaling parameter in high-density laser-produced plasmas from tin-microdroplets. Observed changes in the experimental emission spectra from plasmas of various droplet sizes as well as various laser pulse durations are remarkably well described using a one-dimensional radiation transport equation featuring the relative optical depth of the plasma as sole parameter. The excellent description of the experimental data by the model suggests that a dominant fraction of the EUV emission may be produced in a single-density, single-temperature region of the plasma because the underlying opacity does not appear to change. The here established scaling with optical depth indicates that Nd:YAG LPPs may suffer from strong absorption and re-emission significantly redistributing the spectral energy into wavelength-bands other than 13.5 nm in case of large plasma size. Therefore, the optical depth of these light sources needs to be minimized to reach highest SP values which can be done by reduction of laser pulse duration and droplet size. In such optimized cases, and accounting for the difference in laser absorptivity, CE values of Nd:YAG-driven plasma may well rival those of state-of-the-art CO_2-driven plasma sources.

3 | Extreme ultraviolet light from a tin plasma driven by a 2-μm-wavelength laser

L. Behnke, R. Schupp, Z. Bouza, M. Bayraktar, Z. Mazzotta, R. Meijer, J. Sheil, S. Witte, W. Ubachs, R. Hoekstra, and O. O. Versolato

Opt. Express **29**, 4475-4487 (2021), manuscript as submitted

An experimental study of laser-produced plasmas is performed by irradiating a planar tin target by laser pulses, of 4.8 ns duration, produced from a KTP-based 2-μm-wavelength master oscillator power amplifier. Comparative spectroscopic investigations are performed for plasmas driven by 1-μm- and 2-μm-wavelength pulsed lasers, over a wide range of laser intensities spanning $(0.5–5) \times 10^{11}$ W/cm^2. Similar extreme ultraviolet spectra in the 5.5–25.5 nm wavelength range and underlying plasma ionicities are obtained when the intensity ratio is kept fixed at $I_{1\mu m}/I_{2\mu m} = 2.4(7)$. Crucially, the conversion efficiency of 2-μm-laser energy into radiation in the industrially relevant 2% bandwidth centered at 13.5 nm is found to be a factor of two larger, at a representative 60° observation angle, than in the case of the denser 1-μm-laser-driven plasma.

3.1 Introduction

Extreme ultraviolet (EUV) lithography has successfully entered high-volume manufacturing, enabling the continued miniaturization of semiconductor devices. The required EUV light is generated from mass-limited tin-microdroplet laser-produced plasma (LPP) [11, 12, 80, 82, 83]. Multiply-charged tin plasma ions are the atomic sources of EUV radiation near 13.5 nm wavelength [12, 18, 19, 23, 24, 27, 29, 30]. Currently, CO_2-gas lasers operating at $\lambda = 10.6\,\mu$m wavelength are used to drive the EUV-emitting plasma at a high conversion efficiency (CE) of laser energy into *in-band* radiation, i.e., in a 2% wavelength bandwidth centered at 13.5 nm emitted into the hemisphere back towards the laser that is relevant for state-of-the-art EUV lithography. Solid-state lasers, operating at near- or mid-infrared wavelengths, may however become a viable alternative in the future. Such laser systems would potentially provide a smaller footprint, a significantly higher efficiency in converting electrical power to laser light, and may be scaled to much higher pulse energies and output powers which will enable even more powerful EUV light sources. However, the shorter drive laser wavelength of, e.g., the well-known Nd:YAG laser (1.064 μm) is associated with large optical depths originating from a high critical plasma density [80]. Large optical depths may strongly limit the efficiency of such Nd:YAG-driven sources as opacity effects broaden the EUV spectrum well beyond the 2% wavelength acceptance bandwidth, thus reducing the spectral purity (SP) of the EUV plasma source [44–47, 62, 84, 89, 90]. SP is defined here as the ratio of in-band EUV energy to the total energy emitted in the 5.5–25.5 nm range. Simulation efforts indicate that a global optimum of the efficiency of converting drive laser light into useful EUV radiation lies in between the well-known 1- and 10-μm cases [91]. In this range, thulium lasers, operating at 1.9-μm wavelength, appear promising [16]. However, no experimental studies of plasmas driven by lasers in this wavelength range, under conditions relevant for EUV emission, are yet available. In this work we present a study of the EUV emission spectrum of a 2-μm-wavelength-LPP generated from a planar-solid tin target. The laser light is obtained from a master oscillator power amplifier (MOPA) based on a series of KTP crystals pumped by a Nd:YAG laser. This setup enables assessing the potential of thulium lasers without the expense of building and fielding one. The obtained EUV spectra and CE are compared to those obtained from Nd:YAG-LPP under otherwise very similar conditions.

3.2 Experimental setup

In this work we present an experimental study of an LPP generated by illuminating a planar-solid tin target of 99.995% purity with lasers having wavelengths of 1 μm and 2 μm. The target is mounted on a two-axis translation stage inside a vacuum chamber pumped to 1×10^{-6} mbar. The target is moved after illumination by two laser pulses to prevent crater formation influencing the EUV emission. Spectral emission in the 5–25 nm range is recorded by means of a transmission grating spectrometer positioned at 60 degrees with respect to the incoming laser (see Fig. 3.1). The spectrometer is operated with a slit width of 25 μm and a 10 000 lines/mm grating. The dispersed light is collected on a back-illuminated charge coupled device and is post-processed, correcting for the camera's quantum efficiency and grating dispersion efficiency. More details on the spectrometer and post-processing of the images are provided in Ref. [68] and [84]. To obtain the absolute amount of EUV radiation emitted in a 2% bandwidth around 13.5 nm, a calibrated EUV photodiode assembly [84] is used. It is installed at an angle of $-60°$, mirroring the alignment of the spectrometer, see Fig. 3.1(a). This photodiode assembly consists of a Mo/Si multilayer mirror that reflects the in-band radiation onto a photodiode. The photodiode is coated with a Si/Zr coating in order to block infrared light.

The 2-μm light source comprises a KTP-based MOPA operated in type-2 phase matching following the approach of Arisholm *et al.* [92]. The MOPA setup is pumped at a 10 Hz repetition rate by a seeded Q-switched Nd:YAG laser (Quanta-Ray 250-10 PRO) providing pulses of 10 ns duration (at full width at half maximum, FWHM). First, a 2170 nm idler seed beam of 1.8 mJ energy is created in a singly-resonant optical parametric oscillator (OPO). To create this seed beam, 18 mJ of the pump light is demagnified to a beam diameter of 1.5 mm and is coupled into the OPO which is operated in a collinear alignment. About 20% of the pump radiation is converted into a 2090-nm-wavelength signal beam and a 2170 nm idler beam. At the exit of the OPO a dichroic mirror separates the signal and idler beams from the remaining pump radiation. The idler beam is subsequently expanded to 11 mm in diameter to seed the OPA, while the signal beam is removed through polarization optics. The OPO and OPA are pumped by the same laser. To achieve the highest efficiency in the OPA, 1.3 J of the pump laser light is delayed by 1.3 ns and is reduced to a beam size of 10 mm in diameter. Seed and pump beams are overlapped on a dichroic mirror after which they pass three 18-mm-long KTP crystals. The crystal orientation is alternated to compensate for walk-off. A total energy of 260 mJ is achieved in signal and idler combined. Pump and signal beams are separated from the idler using a dichroic mirror and polarization optics, respectively. To adjust the idler beam energy a combination of half-wave plate and polarizer is installed before it is focused onto the tin target. The size of the focal spot is 72×128 μm (FWHM). The asymmetry in the focal spot size is caused by the slightly higher beam quality

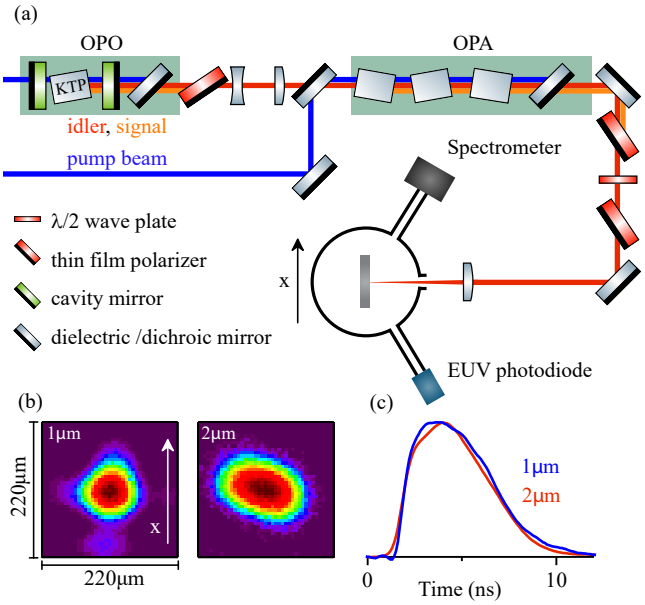

Figure 3.1: (a) Schematic representation of the experimental setup. A master oscillator power amplifier (MOPA) setup, comprising an optical parametric oscillator (OPO) and an optical parametric amplifier (OPA), is pumped by a Nd:YAG laser. The 2-μm-idler beam from the MOPA is focused onto a planar-solid tin target to create plasma. The EUV emission from the plasma is captured by a transmission grating spectrometer and a calibrated EUV photodiode. (b) Spatial and (c) temporal profiles of the 1-μm and 2-μm drive lasers.

on the horizontal, x-axis of the beam (cf. Fig. 3.1(b)). The temporal pulse duration is 4.8 ns (FWHM). Uncertainties in determining the FWHM pulse duration are at or below 0.5 ns. The pulse has a short rise time of ∼1 ns whereas its fall time is significantly longer and is seen to follow the pulse shape of the seed beam.

A seeded, in-house built Nd:YAG laser is used as the 1-μm-laser light source to drive plasma [73]. The laser employs two electro-optical modulators to create temporal profiles of the desired shape. Here the temporal profile was shaped to match that of the idler of the MOPA (see Fig. 3.1(c)). A lens is used to focus the laser beam onto the tin target to a symmetric spot size of 66 μm (FWHM) closely matching the beam spot size of the idler beam in the measurement plane (see Fig. 3.1(b)).

3.3 Results

In the following, we assess the potential of a 2-μm-wavelength tin-plasma driver by studying the spectral characteristics with emphasis on EUV in-band radiation. Fig. 3.2(a) shows EUV spectra obtained when the beam intensity $I_{2\mu m}$ is varied in a (0.2–1.9) × 10^{11} W/cm^2 range. The intensity of the 2-μm driver $I_{2\mu m}$ is given by the peak intensity in time and space by $I_{2\mu m} = (2\sqrt{2\ln 2/2\pi})^3 E_{2\mu m}/abt_p$. Here, $E_{2\mu m}$ is the laser energy, a and b are the Gaussian FWHM sizes along the major and minor axis of the elliptical beam, and t_p is the FWHM pulse duration. Spectral features belonging to Sn^{5+}–Sn^{15+} are observed in the studied spectral range [18, 21, 23, 29, 76, 93]. At the lower laser intensities, spectral features belonging to Sn^{5+}–Sn^{8+} are visible. At higher laser intensities, spectral features related to the higher charge states Sn^{10+}–Sn^{15+} are prominent. Spectral emission from these charge states also becomes visible in the short-wavelength region of the spectra below 12 nm. The evolution of spectral features in this wavelength regime gives direct qualitative insight into the underlying charge state distribution as the contributions from the individual charge states can be identified [76].

For comparison, in Fig. 3.2(b) a set of spectra is presented that was obtained using the 1-μm-wavelength driver. Emission spectra are obtained for beam intensities $I_{1\mu m}$ ranging (0.4–4.4) × 10^{11} W/cm^2. $I_{1\mu m}$ is defined analogously to $I_{2\mu m}$. The beam intensities are selected such that similar short-wavelength features are obtained as in the respective 2-μm cases. The laser intensity at which any particular charge state distribution is obtained, is lower for the 2-μm case by about a factor of two. The evolution of spectral features with laser intensity appears to be similar, comparing Fig. 3.2(a) and 3.2(b).

To study this difference in more detail, pairs of intensities $I_{1\mu m}$ and $I_{2\mu m}$ were chosen such that the short-wavelength spectral features, ranging from 6–10 nm, in the respective emission spectra are best matching. In Fig. 3.2(c), the ratio of thus selected pairs $I_{1\mu m}/I_{2\mu m}$ is plotted versus $I_{1\mu m}$. On average the 1-μm-driver requires a constant factor 2.4(7) higher intensity to reach the same effective charge state distribution of the plasma when compared to the 2-μm case. The number in brackets in the ratio 2.4(7) indicates the overall uncertainty which is dominated by systematic uncertainty. Naively, one would perhaps rather expect this ratio to be closer to a value of four given (i) the $n_c \propto \lambda^{-2}$ dependency of the critical electron density n_c on drive laser wavelength λ; (ii) the approximately linear scaling of the local emission intensity (which in steady state equals laser absorption and hence $\propto I$) with ion density n_i; and (iii) that $n_i \sim n_c$ at equal charge state distribution. This would lead to $n_i \sim n_c \propto \lambda^{-2}$. To achieve equal temperatures, one would thus expect a scaling of required laser intensity with wavelength $I \propto \lambda^{-2}$. Studies on quasi-stationary ablation fronts [41] relevant for our current investigations with

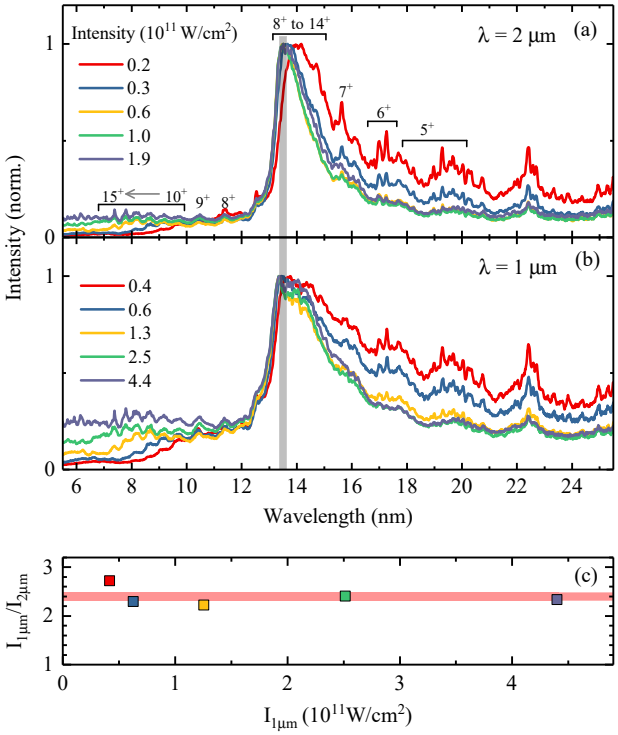

Figure 3.2: Spectra from plasma produced from a planar-solid tin target irradiated with laser pulses at various intensities of the (a) 2-μm-driver of 4.8 ns duration and Gaussian spot size of 72×128 μm. The emission features attributed to the various Sn ions are labeled by the respective charge state. (b) Spectra from tin plasma driven by a 1-μm-beam of 4.4 ns pulse duration and Gaussian spot size of 66×66 μm. The gray vertical band indicates a 2% bandwidth centered at 13.5 nm. (c) Ratio of intensities of 1- and 2-μm-drive laser beams needed to obtain spectra with matching short-wavelength features. The red line indicates the average ratio.

significant laser absorption in the underdense coronal region, before the critical surface, instead indicate a scaling of a typical density $n_i \propto \lambda^{-1}$ and, thus, $I \propto \lambda^{-1}$, all other factors remaining constant over the absorption path (see Eq. (31) in Ref. [41]). This latter scaling is fully in line with our current findings and sheds light on the physics origins of the plasma-emission of EUV light. Further radiation-hydrodynamic simulations are however required to investigate the details of the evolution of the relevant plasma conditions and their dependence on drive laser wavelength.

In Fig. 3.3(a) the CE is plotted versus drive laser intensity for the 1-μm and 2-μm cases. The measured in-band radiation is extrapolated from the measurement at 60° to the 2π steradian hemisphere facing the laser origin, assuming isotropic emission over this half-sphere. From literature, it is evident that the EUV emission from LPPs from planar-solid targets has a some angular anisotropy [49]. Several studies have indicated that the angular dependence of EUV emission is nearly independent on the focal spot size and the pulse duration [49, 52, 94]. For this reason, our observations are not expected to be dominated by any small remaining differences in laser beam characteristics which were carefully matched in our experiments. Changing the drive wavelength for a tin-LPP on a planar-solid target from 266 nm to 1 μm was found to lead to a reduced angular dependence of the in-band emission [75]. For droplet targets, a 10-μm-driven LPP was shown to exhibit only a slightly reduced angular dependence of the in-band emission in comparison to the 1-μm-driven LPP [95] and thus the relatively small step to 2-μm laser radiation is not expected to change the current EUV emission anisotropy significantly. We furthermore note that the observation under the current, relatively large angle of 60° constitutes a representative measure of the overall CE [49, 52, 84, 94].

The open markers in Fig. 3.3(a) indicate data obtained from the absolute in-band response of the spectrometer. Here, the in-band counts of the spectrometer are calibrated by means of the EUV photodiode. The CE of the 2-μm-LPP rises with beam intensity, up to a maximum value of 3.1% at a laser intensity of 1.0×10^{11} W/cm^2. When further increasing the laser intensity CE decreases. For the 1-μm case, a similar rise of CE with increasing beam intensity is observed, with a maximum CE reaching 1.7%, i.e., only about half that of the 2-μm case. The maximum CE for the 1-μm-LPP is reached at a laser intensity of 3.0×10^{11} W/cm^2. No decrease in CE is observed when moving to higher laser intensities, within the probed parameter space. Comparing the two drive laser cases, the relative difference in maximum CE amounts to a factor 1.8. The 1-μm-LPP requires significantly higher intensities to reach optimum CE. This is in line with the findings presented in Fig. 3.2(c).

Fig. 3.3(b) shows the spectral purity of both the 1-μm and the 2-μm-LPPs as a function of laser intensities. Both SP data sets show a behavior that is similar to that of the corresponding CE curves. Note again that SP is here defined as the ratio

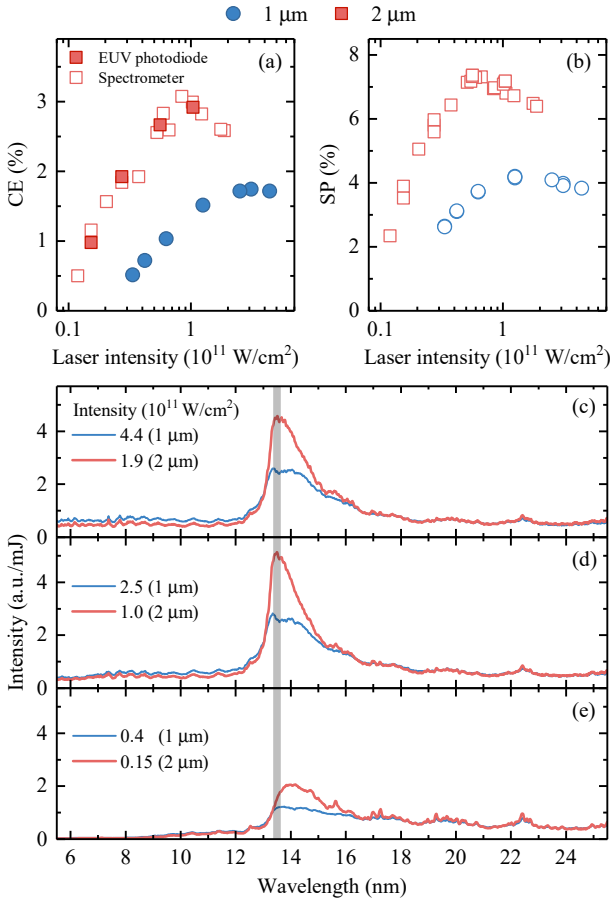

Figure 3.3: Comparison of tin plasma emission characteristics for the 1- and 2-µm-drivers: (a) Dependency of conversion efficiency (CE) on drive laser intensity for both drivers. The plot shows CE directly captured by a calibrated EUV photodiode, mounted under a 60 degree angle (cf. Fig. 3.1), as well as CE obtained from the absolute in-band response of the spectra, all assuming isotropic emission. (b) Spectral purity (SP) versus the intensity of the corresponding drive laser. (c)–(e) Juxtaposition of emission spectra for the two laser cases at three different intensities. The spectral counts of the spectrometer are divided by the drive laser energy.

of in-band EUV energy to the total energy emitted in the 5.5–25.5 nm range. The maximum SP of the 2-μm-LPP is at 7.4%, a factor 1.8 larger than the value of the 1-μm-LPP with a maximum of 4.2%. The ratio of the maximum SP's is identical to the ratio of the maximum CE's. This indicates that the discrepancy in conversion efficiency can be attributed to the decreased SP of the 1-μm-LPP. Figures 3.3(c)–3.3(e) show pairs of matching emission spectra, i.e., plasmas having similar ionicities. Panel 3.3(c) depicts the 2-μm-LPP spectrum with the highest CE. All spectra have been divided by the drive laser energy. The out-of-band features are seen to match well. It is apparent that a significant amount of spectral emission between 13 nm and 15 nm is missing in the 1-μm case compared to the 2-μm-LPP. This lack of emission in the unresolved transition array at 13.5 nm explains the reduced CE of the 1-μm-LPP.

To qualitatively explain the significant differences observed between the two drive laser cases, it is instructive to employ an intuitive two-zone radiation transport model. In this model, the emission from a hot plasma core zone ('zone 1') traverses a plasma zone ('zone 2') at a modestly lower density and temperature. Such a two-zone plasma approximates our experimental conditions using a laser beam with a Gaussian spatial intensity profile which inhomogeneously heats the plasma. The second zone will contribute to the overall emission but will also partially absorb the light emitted from the first zone [96, 97]. Following Ref. [89], the spectral radiance L_λ of a homogeneous, one-dimensional plasma is given by $L_\lambda = B_\lambda\,(1-e^{-\tau_\lambda})$. Here B_λ is the Planck source function, assuming local thermodynamic equilibrium (LTE) conditions. The subscript λ indicates the wavelength dependency of L_λ. In the exponent, τ_λ is the wavelength-specific optical depth [12, 89]. The expected density and temperature values support our LTE approach (see, e.g., Ref. [12]) and small deviations from it do not meaningfully impact our qualitative analysis in the following. We now expand the model by adding a second layer of plasma. The first plasma layer emits the spectral radiance $L_{\lambda,1}$ over an optical depth $\tau_{\lambda,1}$. This light subsequently traverses a second plasma layer with an optical depth $\tau_{\lambda,2}$. The total spectral radiance $L_{\lambda,2}$ exiting the second layer of plasma is given by

$$L_{\lambda,2} = B_{\lambda,1}\left(1-e^{-\tau_{\lambda,1}}\right)e^{-\tau_{\lambda,2}} + B_{\lambda,2}\left(1-e^{-\tau_{\lambda,2}}\right), \tag{3.1}$$

where $B_{\lambda,1}$ and $B_{\lambda,2}$ are the respective blackbody functions of the two plasma layers. Next, we take two spectra obtained from plasma driven by 2-μm-laser light. These two spectra serve as base spectra for the model's two plasma layers [89]. Both spectra are, for simplicity, assumed to be generated from a single density-temperature plasma layer with significant optical depth ($L \approx B$ at peak emission) of value $\tau_{\lambda,i} \cdot a_i$ ($i = 1, 2$ for zones 1 and 2) with a constant multiplication factor a_i accounting for differences in density or length scales following the approach of Schupp *et al.* [89].

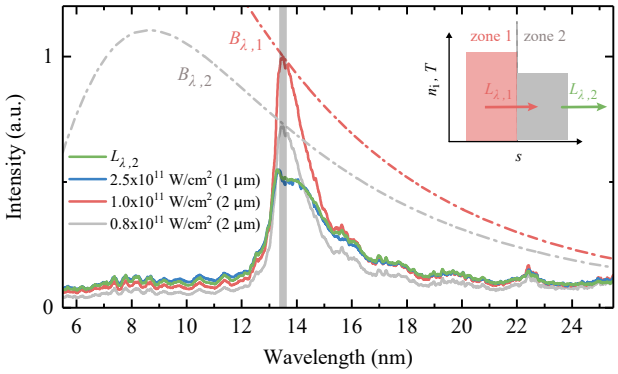

Figure 3.4: Tin spectra from plasmas driven by 1- and 2-µm-lasers. The blackbody functions $B_{\lambda,1}$ and $B_{\lambda,2}$ are divided by $B_{13.5\,\mathrm{nm},1}$. The 2-µm-LPP spectra are scaled to be confined by their respective blackbody functions. The 1-µm-LPP spectrum is scaled with the same factor as the 1.0×10^{11} W/cm^2, 2-µm spectrum (cf. Fig. 3.3(d)). The green curve depicts the fit result of Eq. (3.1) to the 1-µm-LPP spectrum (see main text). The inset schematically depicts the model.

In the following, the base spectrum of the first zone is associated with the maximum CE (cf. Fig. 3.3(d)). The base spectrum for the second zone is chosen from a modestly lower laser intensity, corresponding to a modestly lower plasma temperature conform our model. Following Ref. [12] the effective temperature of the first zone is set to 32 eV associated with optimum plasma conditions for producing in-band EUV light at the here expected plasma densities [12]. The plasma temperature of the second zone is subsequently found by matching the relative intensity values of the two base spectra at 13.5 nm wavelength (as $L \approx B$ at peak emission given the large optical depths involved [12, 89]). This results in a temperature of 29 eV for the second zone. The multiplication factors a_i are used as free fit parameters, including an additional overall amplitude scale factor. Fig. 3.4 shows the result of a least-squares fit of the model function Eq. (3.1) to the measured 1-µm-driven spectrum at a 2.5×10^{11} W/cm^2 laser intensity that reproduces the ionicity of the 2-µm-driven base spectrum (see Fig. 3.3(d)). The model is seen to excellently reproduce the data. The fit parameters obtained are $a_1 = 1.3$ and $a_2 = 0.7$, close to unity value such that the original base spectra are already representative of the emission of the two zones. A more quantitative interpretation of these fit values is not currently warranted given the qualitative nature of the model application. A comprehensive explanation of the generic effects of a two-zone plasma is provided in Ref. [96] albeit for hotter and denser plasma. EUV radiation, produced in the hottest part of the plasma, passes through regions of underheated plasma gener-

ated by the lower-intensity parts of the Gaussian laser intensity profile. The EUV emission in the case of the 1-μm-drive laser occurs at a higher plasma density than that of the 2-μm-driver and also its underheated plasma zone will have higher ion density. Hence, the 1-μm-LPP exhibits a higher EUV self-absorptivity in the underheated zone making the 2-μm-LPP here the more efficient emitter of in-band EUV radiation.

3.4 Conclusion

In conclusion, conversion efficiencies in excess of 3%, assuming isotropic emission of the in-band EUV radiation, have been achieved from a Sn plasma driven by a 2-μm-wavelength laser system, outperforming plasmas driven by a 1-μm-laser by a factor of two. The difference between the two drive laser cases can furthermore be qualitatively explained from self-absorption effects and their impact on spectral purity. Further increases in CE are to be expected when providing a homogeneous heating of the plasma, optimizing the spatio-temporal intensity profile of the drive laser. Such future studies, preferably executed on mass-limited droplet targets and including measurements of the full angularly resolved EUV emission characteristics, will further pave the way for the application of 2-μm drive lasers in industrial sources of EUV radiation powering tomorrow's nanolithography.

4 | Characterization of 1- and 2-μm-wavelength laser-produced microdroplet-tin plasma for generating extreme ultraviolet light

R. Schupp, L. Behnke, J. Sheil, Z. Bouza, M. Bayraktar, W. Ubachs, R. Hoekstra, and O. O. Versolato

Submitted

Experimental spectroscopic studies are presented, in a 5.5–25.5 nm extreme ultraviolet (EUV) wavelength range, of the light emitted from plasma produced by the irradiation of tin microdroplets by 5-ns-pulsed, 2-μm-wavelength laser light. Emission spectra are compared to those obtained from plasma driven by 1-μm-wavelength Nd:YAG laser light over a range of laser intensities spanning approximately $(0.3–5) \times 10^{11}$ W/cm^2, under otherwise identical conditions. Over this range of drive laser intensities, we find that similar spectra and underlying plasma charge state distributions are obtained when keeping the ratio of 1-μm to 2-μm laser intensities fixed at a value of 2.1(6), which is in good agreement with RALEF-2D radiation-hydrodynamic simulations. Our experimental findings, supported by the simulations, indicate an approximately inversely proportional scaling $\propto\lambda^{-1}$ of the relevant plasma electron density, and of the aforementioned required drive laser intensities, with drive laser wavelength λ. This scaling also extends to the optical depth that is captured in the observed changes in spectra over a range of droplet diameters spanning 16–51 μm at a constant laser intensity that maximizes the emission in a 2% bandwidth around 13.5 nm relative to the total spectral energy, the bandwidth relevant for EUV lithography. The significant improvement of the spectral performance of the 2-μm- vs 1-μm-driven plasma provides strong motivation for the development of high-power, high-energy near-infrared lasers to enable the development of more efficient and powerful sources of EUV light.

4.1 Introduction

Laser-driven microdroplet-tin plasma provides the extreme ultraviolet (EUV) light that is used in state-of-the-art EUV lithography [11, 18, 31, 32, 80–82]. Ever more powerful sources of EUV light are required for future lithography applications. This EUV light is generated from electronic transitions in multiply charged tin ions that strongly emit radiation in a narrow band around 13.5 nm [19, 21–27, 29, 30, 93]. EUV-emitting plasma in an industrial nanolithography machine is driven by CO_2-gas lasers with a 10-μm wavelength. Such plasma achieves particularly high conversion efficiencies (CE) of converting drive laser light into EUV radiation in a 2-% wavelength bandwidth around 13.5 nm, the so-called in-band radiation, that can be transported by the available Mo/Si multilayer optics [10, 40]. Near- or mid-infrared solid-state lasers may however soon become an attractive alternative to the CO_2-gas lasers because such modern solid-state lasers are expected to have a significantly higher efficiency in converting electrical power to laser light. Furthermore, they may reach much higher pulse energies and output powers, in turn enabling more EUV output. Big Aperture Thulium (BAT) lasers [16, 98] represent a particularly promising class of novel, powerful laser systems that have recently drawn significant attention. These lasers would operate at 1.9-μm wavelength, in between the well-known cases of 1- and 10-μm drive lasers. Recent simulation work indicates that a global CE optimum lies within this range of 1- and 10-μm drive laser wavelength [91]. Briefly, such studies point out that the longer-wavelength drivers are associated with sub-optimal absorption of the laser energy by the plasma whereas shorter-wavelength drivers may exhibit severe opacity broadening of the EUV spectrum out of the 2-% acceptance bandwidth [62, 89, 90]. To date, no experimental studies of mass-limited, microdroplet-tin-based plasmas driven by lasers in this wavelength range are however available to verify these claims.

In this article a study of the EUV emission spectrum of 2-μm-wavelength-laser-driven tin-microdroplet plasma is presented. The laser light is obtained from a master oscillator power amplifier setup that comprises a series of KTP crystals pumped by a ns-pulsed Nd:YAG laser ($\lambda \approx 1$ μm), enabling one to gauge the potential of, e.g., thulium lasers without the effort of building one. The recorded spectroscopic data are compared to those obtained from a 1-μm-driven plasma under otherwise identical conditions, over a wide range of droplet sizes and laser intensities. Radiation-hydrodynamic simulations using the RALEF-2D code [17], are presented to support the experimental findings. Following the recent work of Schupp *et al*. [89] on Nd:YAG-laser-pumped plasma, an analytical solution for radiation transport in an optically thick one-dimensional plasma is used to quantify the influence of optical depth on the broadening of the key emission feature at 13.5 nm.

4.2 Experiment

In the first set of experiments micrometer-sized liquid tin droplets are irradiated with high-intensity 2-μm-wavelength laser pulses produced in a master oscillator power amplifier (MOPA). Following the work of Arisholm *et al.* [92], the MOPA consists of a singly resonant optical parametric oscillator (OPO) in collinear alignment followed by an optical parametric amplifier (OPA). The latter comprises two 18-mm long KTP crystals operated in type II phase matching. The setup (see Fig. 4.1) is pumped by a seeded Nd:YAG laser with a spatially flat-top and a temporally Gaussian profile of 10 ns (FWHM). The OPO is pumped with 18 mJ of energy within a 1.5-mm-diameter beam resulting in an idler beam energy of 1.8 mJ at a wavelength of 2.17 μm. The OPO is operated slightly off its degeneracy point to minimize back conversion of signal and idler into the pump wavelength, a process which reduces beam quality of both beams. After the OPO the signal beam is removed and the idler beam expanded to 11 mm and amplified in the OPA. Using 1.3 J of pump energy within a beam diameter of 10 mm, 260 mJ of 2-μm radiation are obtained, summing signal and idler pulse energies. The pulse duration of both beams after amplification is 4.3 ns.

For the experiments the signal beam is removed via polarization optics and solely the idler beam is used. The idler beam is focused onto several ten-micrometer-sized liquid tin droplets created via coalescence of even smaller microdroplets from a tin jet in a vacuum chamber that is kept at or below 10^{-6} mbar. The diameter of the microdroplets is adjustable within a range from 16–51 μm. The focal spot is elliptical and has a size of 65×88 μm (FWHM) and laser intensities of up to 2.1×10^{11} W/cm^2 are obtained on the tin droplets. Data taken with this 2-crystal setup is used for Sec. 4.4 and is part of the data in Fig. 4.2(c). The intensity is defined as peak intensity in time and space and calculated to $I_\mathrm{L} = (2\sqrt{2\ln 2/2\pi})^3 E_\mathrm{L}/abt_\mathrm{p}$ with laser energy E_L, FWHMs a and b along the major and minor axis of the bivariate Gaussian and pulse duration t_p. The energy in the beam is adjusted by the combination of a half-waveplate and polarizer. The data displayed in Fig. 4.2(a) was taken in a later experiment and after installation of a third crystal in the OPA which increased the energy in signal and idler combined to 360 mJ while the pulse duration increased slightly to 4.7(3) ns (FWHM). The produced beam has a symmetric focal spot and measurements are obtained for three focal spot sizes of 106, 152 and 194 μm (FWHM) that are obtained using lenses of different focal distance length. The data obtained in the first and this later experiment is combined in Fig. 4.2(c).

To enable a direct comparison with plasmas driven by 1-μm wavelength laser pulses, light from the 1-μm pump laser is redirected before entering the MOPA and is focused onto the tin droplets instead. Again, a combination of a half-wave plate and polarizer allows for adjustment of the beam energy. The focal spot has

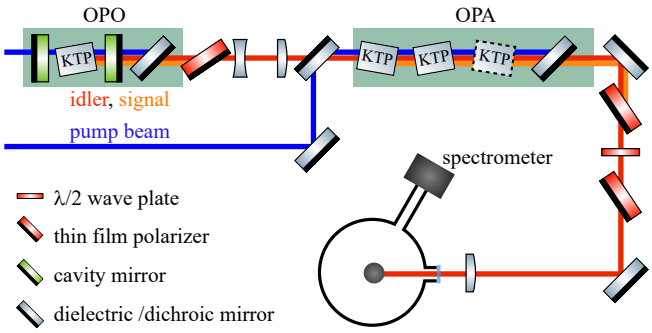

Figure 4.1: Schematic representation of the experimental setup. A master oscillator power amplifier (MOPA) setup, comprising an optical parametric oscillator (OPO) and an optical parametric amplifier (OPA), is pumped by a Nd:YAG laser (blue line). The signal beam is separated via polarization optics and the idler beam ($\lambda = 2.17\,\mu$m) is focused onto tin microdroplets within a vacuum chamber. EUV emission is captured by a transmission grating spectrometer positioned at 60° with respect to the laser axis. An additional, third KTP crystal (dashed outline) was used in the OPA in a subset of the experiments.

a symmetric Gaussian shape of 86 μm (FWHM). The EUV emission from the tin plasma is collected by a transmission grating spectrometer [68] set up under a 60° angle with respect to the incoming laser beam. The spectrometer was operated with a 10 000 lines/mm grating, a 25 μm slit and without filter. The measured spectra are corrected for the grating's first and second order diffraction efficiency as well as for the quantum efficiency of the camera. The wavelength is calibrated in a separate experiment using atomic line emission from an aluminum plasma. Spectral purity (SP), defined as the ratio of spectral energy in a 2% bandwidth around 13.5 nm to the total EUV energy, is used to characterize the EUV light source. All SP values provided are calculated with respect to the measured spectral range of 5.5–25.5 nm.

4.3 Scaling of spectral features with laser intensity and wavelength

For defining development targets regarding power and pulse energy of future 2-μm lasers for use in EUV light sources, it is particularly relevant to know the laser intensity needed to obtain a tin charge state balance optimal for the production of 13.5-nm light. In this section the laser intensity on the tin droplet is scanned and the optimal laser intensity determined as the value at which SP is highest, given that SP is the ultimate limit of CE as follows from energy conservation CE<SP/2

for isotropic emission [84]. To better understand the relevant plasma temperatures and densities, we study the ratio of 1- and 2-μm laser intensities at which plasmas of equal temperatures are established. Plasma temperature is experimentally established via the shape and amplitude of charge state specific spectral emission features [20, 76, 99, 100]. These features are indicative of the plasma's charge state distribution which is predominantly dependent on plasma temperature [41]. The experimental results are then compared to computer simulations using the radiation-hydrodynamic code RALEF-2D as well as to previous analytic work [41].

Spectral dependencies on drive laser intensity

In the experiments, first the idler beam from the MOPA is focused onto a 30-μm-diameter droplet and spectra are measured using the 106-μm spot size at multiple intensities within a range of $(0.1–2.2) \times 10^{11}$ W/cm^2 (see Fig. 4.2(a)). At the lowest laser intensity the plasma strongly emits around 14.5 nm and distinct $4d$–$4f$ transitions in Sn^{6+} are visible around 17 nm [100]. Emission between 18–20 nm can be mainly attributed to Sn^{5+}. At 15.7 nm, a strong emission feature from $4d$–$4f$ and $4p$–$4d$ transitions in Sn^{7+} is visible. Going up this 'ladder' of charge states, emission from $4d$–$4f$ and $4p$–$4d$ transitions in Sn^{8+} is visible at 14.8 nm and from Sn^{9+} at 14.2 nm. With increasing laser intensity the average charge state of the plasma increases and emission from Sn^{10+} is evident in the 9.5–10 nm region [76]. Increasing laser intensity beyond 10^{11} W/cm^2, the plasma strongly emits at 13.5 nm. This emission originates from the $4d$–$4f$, $4d$–$5p$ and $4p$–$4d$ unresolved transitions arrays (UTAs) in Sn^{8+}–Sn^{14+} [18, 21]. With the strong emission at 13.5 nm, charge state specific features become visible between 7 and 12 nm. These features belong to the same Sn^{8+}–Sn^{14+} ions and here the $4d$–$5f$, $4d$–$6p$ and $4p$–$5s$ transitions contribute strongest [20, 76]. With increasing laser intensity SP rises to values of 15% at 0.8×10^{11} W/cm^2 where charge state balance is optimal for in-band EUV emission, before reducing again at even higher intensity values (see inset in Fig. 4.2(b)).

Second, plasma is created using laser light of 1-μm wavelength. Spectra for laser intensities within the range of $(0.3–4.4) \times 10^{11}$ W/cm^2 are shown in Fig. 4.2(b). When compared to the 2-μm drive-laser case the spectra show very similar shape, albeit at an apparent increased overall width. Again the same emission features of charge states Sn^{5+}–Sn^{9+} are visible at the lowest laser intensity but with somewhat less prominent emission features. This reduction in prominence is particularly noticeable for the peaks of charge states Sn^{6+} and Sn^{7+} (between 14 and 16 nm). Further the Sn^{9+} peak at 14.2 nm is hardly visible (cf. 0.2×10^{11} W/cm^2 in the 2-μm case). The SP rises until it reaches values of 9.7% around 2×10^{11} W/cm^2 and subsequently decreases as the charge state balance becomes sub-optimal for emission of 13.5 nm light. The peak intensities used in this work agree well with previously published work, where the optimal SP was found at an intensity of

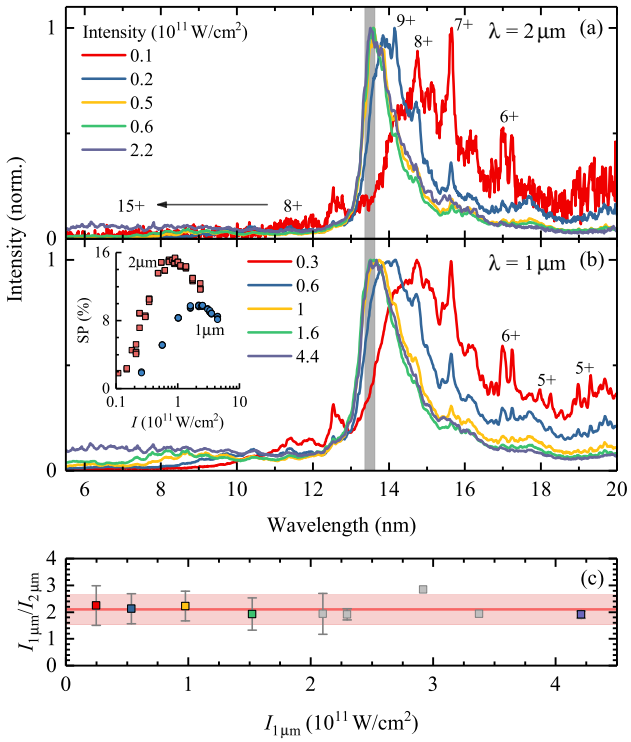

Figure 4.2: Spectra from tin droplet plasma observed at various intensities of the (a) 2-µm beam (4.7 ns pulse duration, 106 µm FWHM, 3 KTP crystals) and the (b) 1-µm Nd:YAG beam (10 ns pulse duration, 86 µm FWHM). The droplet size in both cases is 30 µm. (c) Ratio of the intensities of 1- and 2-µm drive laser beams needed to obtain spectra with similar spectral features. The data points represent the average intensity ratios from data taken with four different laser spot sizes of the 2-µm laser beam of 65×88, 106, 152 and 194 µm (FWHM), respectively. The error bars indicate the standard deviation per measurement. The red line represents the average over all data points and the shaded band the standard deviation of the average.

1.4×10^{11} W/cm^2 using a temporally and spatially box-like laser profile to illuminate the tin droplets [84]. The higher intensity value found in this work is attributed to the fact that, because of their spatial extent, the droplets experience a slightly lower average intensity compared to the peak values stated.

To obtain the sought-for laser-intensity ratio $I_{1\mu m}/I_{2\mu m}$, each spectrum of the 2-μm laser case at intensity $I_{2\mu m}$ is matched to a spectrum of the 1-μm case at intensity $I_{1\mu m}$ for which the resemblance of the relative amplitudes and shape of spectral features is best matching. As the spectral features are characteristic of individual tin charge states [99, 100] this comparison provides access to the scaling of the plasma's charge state distribution (and hence temperature) with laser wavelength. For each match of laser intensities the ratio $I_{1\mu m}/I_{2\mu m}$ is calculated and plotted as a function of $I_{1\mu m}$ in Fig. 4.2(c). The data points represent the average of comparisons made for multiple spot-size conditions and for two droplet size conditions. In all cases spectra were compared to the ones taken with the 1-μm wavelength laser beam size of 86 μm. More specifically, the comparison encompasses measurements with a 30-μm-diameter droplet for 2-μm case beam sizes of 65×88, 106×106, 152×152 and 194×194 μm and on a 19-μm-diameter droplet for the 65×88-μm beam. The red line shows the average $I_{1\mu m}/I_{2\mu m} = 2.1(6)$ of all measurements with the standard deviation (distribution width and not the error-on-the-mean) of the mean value as red shaded area. The depicted uncertainty is the standard deviation of the mean.

Theory and discussion

The temperature of a plasma can be expressed analytically if the equation of state (EOS) is sufficiently well known. The required EOS parameters will however depend on the location in the plasma where the laser light is absorbed. Two cases can be distinguished [41]. Case I: absorption of laser light dominantly occurs close to the critical surface where the plasma's electron density equals the critical density ($n_e \approx n_{crit} \propto \lambda^{-2}$). This case is relevant for long wavelength laser light, e.g., from CO_2 lasers. Case II: absorption is already significant in the underdense corona where the electron density is lower than the critical electron density. For laser absorption of 1- and 2-μm beams, case II applies and the tin plasma temperature can be written as [41]

$$T \propto \left(\frac{1}{R\lambda^2}\right)^{-0.19} [I(1-\phi_r)]^{0.44}, \tag{4.1}$$

with laser wavelength λ, laser intensity I, radiative loss fraction ϕ_r of the plasma and characteristic radius of the sonic surface R, defined as the contour at which the ion velocity equals the local sound velocity. The numerical values for the powers -0.19 and 0.44 originate from the EOS [41]. Differences in radiative losses of the plasmas are neglected in the following, as they may be small for similar density

and temperature plasmas. The sonic surface R is only slightly wavelength dependent and the small difference can be neglected. From Eq. (4.1), an intensity ratio $I_i/I_j = (\lambda_j/\lambda_i)^{0.86}$ here $I_{1\mu m}/I_{2\mu m} = 1.8$ is calculated for $\lambda = 1$ and 2 μm plasmas exhibiting equal plasma temperatures. The predicted ratio of 1.8 agrees well with the experimental one of 2.1(6) and well approximates a scaling with λ^{-1}.

Alongside this analytical approach, the radiation hydrodynamic code RALEF-2D [17] is used to determine the laser intensity ratio yielding equivalent plasma temperatures. RALEF-2D was developed to simulate laser plasma interaction and solves the equations of fluid dynamics in two dimensions (assuming cylindrical symmetry around the laser beam propagation axis) while including necessary physical mechanisms such as laser absorption, thermal conduction and radiation transport. The latter is needed for accurate predictions of a strongly radiating plasma, which is true for the current case. An extensive set of simulations has been performed at conditions close to the experimental ones. A 30-μm-diameter droplet is irradiated by temporally and spatially Gaussian beams. The 1- and 2-μm beams have pulse durations of 10 and 4.3 ns (FWHM) and sizes of 80 and 100 μm (FWHM), respectively. Laser intensities in the range spanning 10^{10}–10^{12} W/cm^2 are simulated. The plasma's peak temperature is plotted in Fig. 4.3. For the given laser intensities the maximum temperature is consistently higher in the 2-μm case. We note that the different pulse durations (10 vs. 4.3 ns) have a minimal impact on temperature and density scales. The maximum temperatures are seen to follow Eq. (4.1) fitted as $T[\mathrm{eV}] = a \cdot \lambda^{0.38}[\mu\mathrm{m}] \cdot I^{0.44}[10^{11}\,\mathrm{W/cm^2}]$, where a common amplitude $a = 43$ is determined by a global fit to all data. Eq. (4.1) captures the scaling of the peak plasma temperature over two decades in laser intensity.

Further shown in Fig. 4.3 are temperature and electron density lineouts along the laser axis away from the droplet at intensities relevant for the efficient emission of EUV light. The intensity of the 1- and 2-μm cases were chosen to have nearly identical peak electron temperature. This temperature strongly increases with distance from the droplet surface and peaks around 11 μm from the droplet surface before it reduces again at larger distances. The maximum temperature is obtained at a factor of 2.0 lower density in the 2-μm case. The point of highest temperature is much closer to the critical density in the 2-μm case indicating that the absorption of laser light occurs closer to critical density while the conditions for laser absorption of case II are still met. Following Ref. [41], and references therein, the scaling of the relevant plasma electron density with wavelength can also be approximated invoking a constant absorbed fraction of the laser light, $k_L R =$ constant. Inserting the Kramers' absorption coefficient for laser radiation k_L we obtain [41, 101]

$$(R\lambda^2)\rho^2\bar{z}^3T^{-3/2} = \text{constant}, \tag{4.2}$$

with the mass density ρ and the plasma's average charge state $\bar{z}$. Considering that

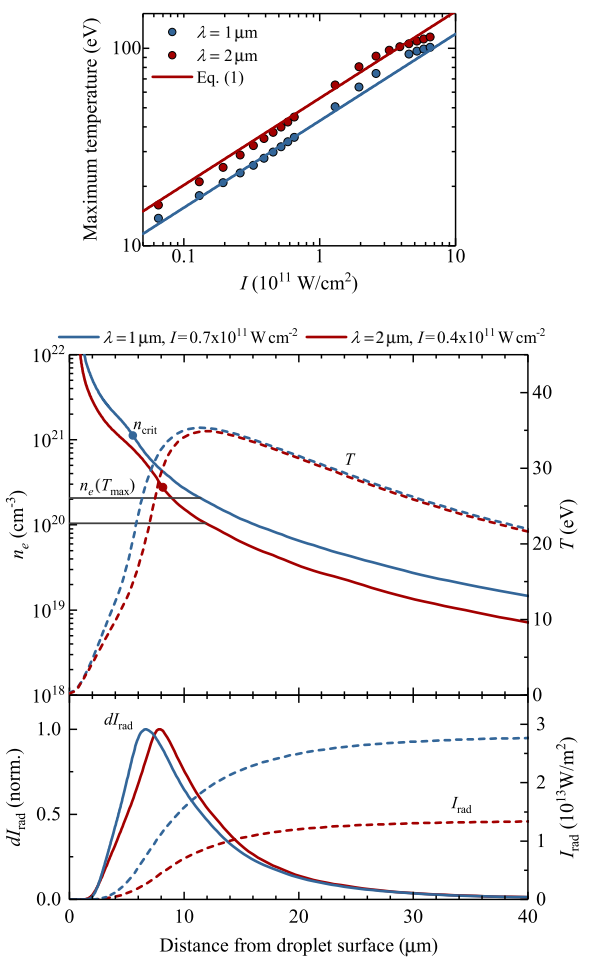

Figure 4.3: Top: maximum temperature of a tin plasma for various laser intensities calculated with the two-dimensional-radiation transport code RALEF-2D. A 30-μm-diameter droplet is illuminated with temporally and spatially Gaussian-shaped laser pulses of wavelengths 1 and 2 μm. Center: temperature and electron density lineout along the axis of the incoming laser beam. Bottom: frequency-integrated local radiation field intensity I_{rad} of the plasma and its normalized derivative dI_{rad}. The radiation field intensity is calculated from Eq (4.3) using the density and temperature lineouts depicted in the center panel. For more detail see text.

mass density ρ and ion density n_i follow the ratio of electron density and average charge state $\rho \propto n_\mathrm{i} = n_e/\bar{z}$, where $\bar{z} \approx 22.5T^{0.6}[\mathrm{heV}]$ (note that T is input here in units of 100 eV) [41], it becomes clear that the ratio of the electron densities lineouts displayed well approximates the ratio of mass density between the two laser wavelength cases. All other factors remaining constant in Eq. (4.2), a reciprocal scaling of mass density ρ and wavelength λ becomes directly apparent. The difference in mass density can thus be attributed to the difference in absorptivity of the laser radiation from Kramers' law [102]. This inversely proportional scaling of density with wavelength is the root cause of the observed intensity ratio.

The bottom panel of Fig. 4.3 shows the radiation field intensity I_rad and its normalized derivative dI_rad. The frequency-integrated radiation field intensity is calculated from

$$I_\mathrm{rad}(s) = I_0 e^{-\int_{s0}^{s}\alpha(s')ds'} + \int_{s0}^{s}\alpha(s')B(s')e^{-\int_{s'}^{s}\alpha(s'')ds''}ds' \tag{4.3}$$

with the Planck mean absorptivity $\alpha_p[\mathrm{m}^{-1}] = 3.3\times10^{-7}\cdot\rho[\mathrm{g/cm}^3]\cdot T^{-1}[\mathrm{eV}]$ using the temperature and electron density information in Fig. 4.3. For more information see Ref. [12]. The normalized derivatives dI_rad peak at 6.5 and 8 μm distance from the droplet surface for the 1- and 2-μm cases, respectively. They show that the typical length scales of emission are similar in both wavelength cases. This finding is in line with the similarity in length scales and indeed profiles of plasma temperature and density (shown in the center panel of Fig. 4.3). The point of largest change in radiation field intensity is located slightly closer to the droplet surface than the point of maximum temperature. The significantly higher density more than compensates for the drop in temperature. The point of largest change in the radiation field intensity of the 1-μm-driven plasma occurs relatively far from the critical density, whereas in the 2-μm-driven plasma this point lies close to the critical density, an observation explained by the distances between the respective maximum temperatures and critical densities. The radiation field intensity at large distances from the droplet surface is approximately a factor of two higher in the 1-μm case because of the factor of two higher (emitter) density compared to the 2-μm case.

4.4 Scaling of optical depth

The scaling of mass density with drive laser wavelength $\rho \propto \lambda^{-1}$ at similar length scales, as established by our simulations, indicates that the optical depth of the plasma, being a product of atomic opacity, mass density and path length, should scale similarly. If optical depth indeed reduces proportionally with drive laser wavelength, the step to a 2-μm laser system could be particularly beneficial. In the following, we perform an analysis of the optical depth associated with the EUV

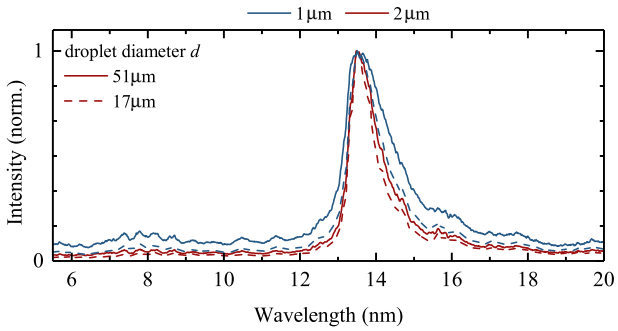

Figure 4.4: Spectral emission from tin plasmas produced with 1- and 2-µm laser wavelength for small and large droplet diameters at laser intensities of 2.4 and 1.1×10^{11} W/cm^2, respectively.

spectra by varying plasma size following the work of Schupp *et al.* [89]. This is accomplished by irradiating droplets having diameters in the range 16–51 µm.

Scaling of peak optical depth with droplet size and drive laser wavelength: examples

In our experiments the droplet diameter is changed in controlled steps from 16–51 µm and a constant laser intensity is used for both laser wavelength cases. First, droplets are illuminated with 2-µm laser light with an intensity of 1.1×10^{11} W/cm^2, close to optimal SP. The spot size is 65×88 µm. In Fig. 4.4 spectra for the smallest and largest droplet diameter are shown for both drive-laser cases. With increasing droplet diameter the main emission feature at 13.5 nm widens and more intense short-wavelength radiation is emitted relative to the 13.5-nm peak. Second, the same scan is repeated with 1-µm laser light at 2.4×10^{11} W/cm^2, an intensity chosen based on the intensity ratio in Fig. 4.2(c). Again, the main emission feature at 13.5 nm widens with increasing droplet diameter and more intense short wavelength radiation is emitted relative to the 13.5-nm peak. For the 1-µm driver these effects however are much stronger.

In the following, the spectra are analyzed regarding their optical depth similar to the analysis in Ref. [89]. The wavelength-dependent optical depth $\tau_\lambda := \int \kappa_\lambda \rho dx$ is defined as the spatial integration over the product of the plasma's opacity κ_λ and mass density ρ. In the instructive case of a one-dimensional plasma [86] in local thermodynamic equilibrium (LTE), the spectral radiance is given by $L_\lambda = B_\lambda (1 - e^{-\tau_\lambda})$, where B_λ is the Planck blackbody spectral radiance. We note that our high-density, strongly collisional 1- and 2-µm-driven plasmas are reason-

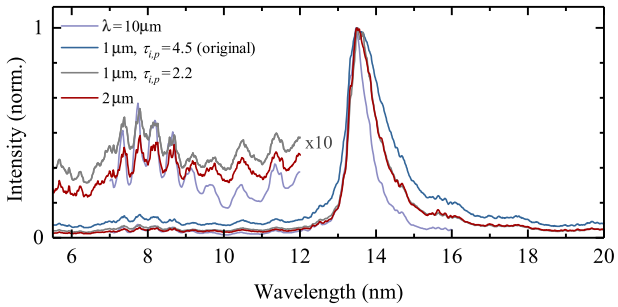

Figure 4.5: Spectrum produced with 2-μm laser light (red line) compared to the radiation-transported reference spectrum for a peak optical depth value of $\tau_p = 2.2$ (gray line, barely distinguishable from the red line). Reference and 2-μm-driven spectra were both obtained using a droplet diameter of 30 μm. Also shown is a spectrum obtained using a 10-μm CO_2 laser that represents the case of small optical depth (reproduced from Ref. [13]).

ably well approximated by LTE [12]. At equal temperatures, and thus average charge state (recall $\bar{z} \sim T^{0.6}$ [41]), this equation enables each measured spectrum $\sim L_{\lambda,i}$ to be well approximated by any other spectrum $\sim L_{\lambda,j}$ when taking into account the ratio of the corresponding peak optical depths $a = \tau_{p,i}/\tau_{p,j}$ as a single parameter independent of wavelength (see Ref. [89] and the Appendix for further details). Subsequently, if any peak optical depth $\tau_{p,j}$ is known in absolute terms, the optical depth of any other spectrum can be deduced. To be able to correct for systematic errors that could possibly occur for relatively low optical depth $\tau \lesssim 1$ we have suitably modified the equation used in Ref. [89] as is detailed in the Appendix.

As a reference spectrum, the spectrum measured at 1-μm laser wavelength, 10-ns pulse duration and 30-μm droplet size is chosen. The peak optical depth of this spectrum is determined by comparison of its 13.5-nm feature to opacity calculations in Ref. [12]. More specifically, radiation transport is applied to the opacity spectrum calculated in Ref. [12] for a here relevant mass density of $\rho = 0.002\,\mathrm{g/cm^3}$ and electron temperature of $T_e = 32\,\mathrm{eV}$. The difference between radiation transported opacity spectrum and experimental spectrum is then minimized by changing the optical depth parameter τ_p in a least-square fit routine. This procedure leads to an absolute peak optical depth of $\tau_{0,p} = 4.5$ for our reference spectrum.

Using Eq. (4.7) the peak optical depth $\tau_{i,p}$ of all spectra is fitted with respect to the reference spectrum. As expected, inserting the relative optical depth obtained from the fits into Eq. (4.6) leads to an excellent reproduction of the main emission feature, as is shown in Fig. 4.5 for a typical example spectrum (30-μm droplet with a 2-μm driver). A further reasonable reproduction of the 7–12 nm features is

established with the 2-μm driver outperforming the model spectrum with respect to the amount of radiation emitted out-of-band. Figure 4.5 also shows a spectrum from an industrial plasma produced by a 10-μm CO_2 driver which represents the limiting case of low optical depth. The step from a 1-μm to a 2-μm driver clearly significantly enhances the spectrum.

Scaling of peak optical depth with droplet size and drive laser wavelength: all results

Having demonstrated the ability of the model function to accurately reproduce spectra from a single reference spectrum, we show in Fig. 4.6(a) the fitted values for all spectra of the droplet size scans for 1- and 2-μm laser wavelength. In all cases the peak optical depth $\tau_{i,p}$ appears to linearly increase with droplet diameter and to strongly depend on the laser wavelength. Indeed, the peak optical depth of the 2-μm-driven plasma lies roughly a factor of 2 below that of the 1-μm one at largest droplet size, which may be expected from the lower plasma density (cf. Section 4.3). However, the 1-μm results were obtained with 10-ns-long pulses and are here compared to the results from approximately 5-ns-long, 2-μm pulses, and optical depth is known to increase with pulse length [84, 89]. To provide a comparison on more equal footing, we further compare in Fig. 4.6(a) our results to previous data [89], obtained using a 1-μm wavelength laser with a 5 ns temporally box-shaped laser pulse. One of these data sets is taken with a spatially flattop laser profile of 96-μm diameter [84, 89] while the other one is taken with a Gaussian laser beam profile of 66 μm FWHM which more closely resembles the experimental conditions for the 2-μm driver case. The spatial intensity distribution of the 1-μm laser beam is seen to impact the effective optical depth (see also Ref. [84]). On comparison of the spectra for the 2- and 1-μm cases at the most comparable temporal and spatial beam conditions, the clear reduction in peak optical depth parameter is maintained. This reduction, up to a factor 1.6 in optical depth, becomes more pronounced at larger droplet diameters. The small deviation from the factor of ∼2 from the $\rho \propto \lambda^{-1}$ scaling may originate from differences in plasma length scales, plasma temperature, or from the finite laser intensity gradient over the plasma length scale. Nevertheless, a very significant reduction in optical depth of up to 40% is demonstrated when using a 2-μm laser to drive the plasma.

With peak optical depth being the pertinent scaling parameter of 1- and 2-μm-driven tin plasmas the corresponding spectral purity of the emission spectrum is related to it in Fig. 4.6(b). All experimental SP values, calculated over the range of 5.5–25.5 nm, collapse onto the gray dashed curve obtained by calculating the SP of the radiation-transported reference spectrum. The 2-μm case is slightly offset towards higher SP values because of the reduced emission in the 7–12 nm wavelength band compared to the radiation transported reference spectrum (cf. Fig. 4.5) that

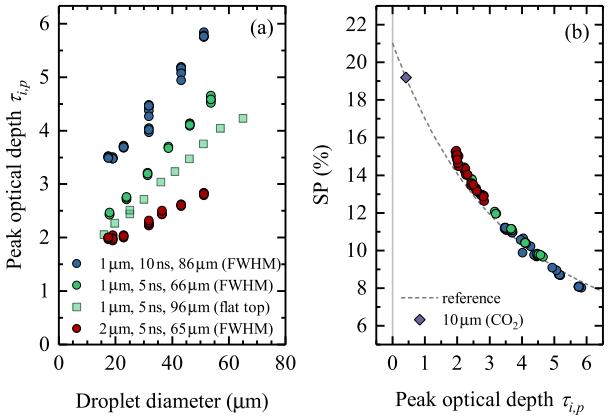

Figure 4.6: (a) Dependency of peak optical depth $\tau_{i,p}$ on droplet diameter for 5- and 10-ns laser pulse duration at 1-μm wavelength and for 4.3-ns pulse duration at 2-μm wavelength. Circles indicate Gaussian spatial laser profile and boxes indicate a homogeneous 'flattop' laser beam profile. Peak optical depth is fitted with respect to the spectrum obtained at 1-μm wavelength, 10-ns pulse duration and 30-μm droplet diameter with optical depth of $\tau_{0,p} = 4.5$. (b) Experimental values for spectral purity (SP) versus peak optical depth. The dashed line represents SP as calculated from the radiation-transported reference spectrum. The diamond symbol indicates the SP value of the radiation-transported reference spectrum for a peak optical depth value $\tau_{i,p} = 0.4$, obtained from comparison of the reference spectrum with the emission of the CO_2-laser-driven plasma spectrum illustrated in Fig. 4.4.

is not captured by the model with the same accuracy as that of the main emission feature at 13.5 nm. This difference between model and experiment may point to a small overestimation of the optical depth of the 2-μm-laser-produced tin plasma, which would explain both the observed overestimation of the short-wavelength out-of-band emission by the model as well as the offset in Fig. 4.6(b). This small overestimation of the optical depth may in turn be due to a broader charge state distribution in our measurements of the 2-μm case caused by, e.g., laser intensity gradients or the slightly lower beam pointing stability compared to the 1-μm case. This observation leads us to expect an even lower optical depth in the 2-μm case and brings our scaling ratio even closer to the expected factor of 2 from the λ^{-1} scaling. More importantly, it indicates that there are further opportunities for narrowing the charge state distribution by providing a more homogeneous heating of the plasma in time and space. Such a narrowing of the charge state distribution around the optimum charge states Sn^{11+}–Sn^{14+} would lead to further improvements of SP and

thus CE.

4.5 Conclusions

In conclusion, the effects of optical depth, plasma density, and laser intensity on the emission spectra of a 2-μm-LPP source of tin microdroplets are investigated. The results are compared to the case of a 1-μm-driven plasma. It is found that the laser intensity required to maintain a common plasma temperature, scales approximately inversely with laser wavelength in going from a 1- to a 2-μm drive laser, a result that will help defining development goals for future 2-μm drive lasers for LPP light sources. The reciprocal scaling with laser wavelength ($\propto\lambda^{-1}$) has its origin in Kramers' law of inverse bremsstrahlung, the main laser absorption mechanism in the tin plasmas investigated. Because of its reduced plasma density, the optical depth of the 2-μm-driven plasma is significantly reduced, allowing for efficient out-coupling of 13.5-nm radiation from the plasma even at larger plasma sizes. In future experiments it will be of interest to use large, preformed targets and investigate the full CE potential of a 2-μm source in a setting more similar to the current industrial one. Our results indicate that there are further opportunities for narrowing the charge state distribution by providing a more homogeneous heating of the plasma in time and space which would lead to further improvements of SP and thus CE. Looking further, it is of interest to experimentally investigate plasma generation using even longer-wavelength laser systems between 2 and 10 μm to find the mid-infrared wavelength optimally suited to drive EUV light sources at 13.5 nm.

4.A Appendix

Radiation transport model

To determine peak optical depth in this work, the recorded spectra are analyzed in a manner similar to that presented in Ref. [89]. In the following, the method from Ref. [89] is first outlined briefly and is subsequently generalized for use with plasmas that are optically thin. The wavelength-dependent optical depth $\tau_\lambda := \int \kappa_\lambda \rho dx$ is defined as the spatial integration over the product of the plasma's opacity κ_λ and mass density density ρ. The spectral radiance L_λ of an extended one-dimensional plasma can be calculated by means of its optical depth as [86]

$$L_\lambda = S_\lambda \left(1 - e^{-\tau_\lambda}\right). \tag{4.4}$$

In local thermodynamic equilibrium (LTE), where collisional processes drive atomic level populations, the source function S_λ equals the Planck blackbody function B_λ. Rearranging Eq. (4.4), the optical depth of the recorded plasma spectrum can be obtained from its relative spectral radiance L_λ / B_λ

$$\tau_\lambda = -\ln\left(1 - \frac{L_\lambda}{B_\lambda}\right). \tag{4.5}$$

The optical depths of two plasmas of similar temperatures, but with modestly different densities and length scales, may differ (in first approximation) only by a single wavelength-independent multiplicative factor a_i, relating the plasmas' optical depths via $\tau_{\lambda,i} = a_i \, \tau_{\lambda,0}$. Here τ_0 and τ_i are the two wavelength-dependent optical depths of the reference spectrum and any other spectrum i, respectively. The relative spectral radiances of these two plasmas can be related to each other via Eq. (4.5)

$$\frac{L_{\lambda,i}}{B_\lambda} = 1 - \left(1 - \frac{L_{\lambda,0}}{B_\lambda}\right)^{\tau_i/\tau_0}. \tag{4.6}$$

In order to apply Eq. (4.6) to the spectra measured, the relative spectral radiance of the spectra must be known. To obtain the relative spectral radiance, the ratio of observed spectrum O_λ (meaning the spectrum as recorded with the spectrometer) and blackbody function is normalized to the peak value at 13.5-nm wavelength (subscript p) by replacing L with $\tilde{L}_\lambda = O_\lambda B_p / O_p$. The normalized ratio $\tilde{L}_\lambda / B_\lambda$ is then multiplied by the amplitude factor $1 - e^{-\tau_p}$ obtained from Eq. (4.5)

$$\frac{\tilde{L}_{\lambda,i}}{B_\lambda} = \frac{1 - \left(1 - \frac{\tilde{L}_{\lambda,0}}{B_\lambda}(1 - e^{-\tau_{0,p}})\right)^{\tau_{i,p}/\tau_{0,p}}}{1 - e^{-\tau_{i,p}}}. \tag{4.7}$$

Note that the wavelength-dependent optical depth values ($\tau_{0,\lambda}$) from Eq. (4.6) have been exchanged by their peak values ($\tau_{0,p}$). This generalized equation allows for determination of peak optical depth in optically thin plasmas in LTE if the peak optical depth of one of the spectra is known. In the current analysis the use of Eq. (4.7) results in optical depth values that are mostly very similar, but some of which are up to 25% lower for the smallest optical depths cases ($\tau \sim 2$), than when using Eq. (4.6). Using Eq. (4.7) the peak optical depths $\tau_{i,p}$ of all spectra are fitted with respect to a reference spectrum of known peak optical depth (see main text).

5 | Characterization of angularly resolved EUV emission from 2-μm-wavelength laser-driven Sn plasma using preformed liquid disk targets

R. Schupp, L. Behnke, Z. Bouza, J. Sheil, M. Bayraktar, W. Ubachs, R. Hoekstra, and O. O. Versolato

To be submitted

The emission properties of tin plasmas, produced by the irradiation of preformed liquid tin targets by several-ns-long, 2-μm-wavelength laser pulses, are studied in the extreme ultraviolet (EUV) regime. In a two-pulse scheme, a pre-pulse laser is first used to deform tin microdroplets into thin, extended disks before the main (2 μm) pulse creates the EUV-emitting plasma. Irradiating 30- to 350-μm-diameter targets with 2-μm laser pulses, we find that the efficiency in creating EUV light around 13.5 nm follows the fraction of laser light that overlaps with the target. Next, the effects of a change in 2-μm drive laser intensity ($0.6–1.8 \times 10^{11}$ W/cm^2) and pulse duration (3.7–7.4 ns) are studied. It is found that the angular dependence of the emission of light within a 2% bandwidth around 13.5 nm and within the backward 2π hemisphere around the incoming laser beam is almost independent of intensity and duration of the 2-μm drive laser. With increasing target diameter, the emission in this 2% bandwidth becomes increasingly anisotropic, with a greater fraction of light being emitted into the hemisphere of the incoming laser beam. For direct comparison a similar set of experiments is performed with a 1-μm-wavelength drive laser. Emission spectra, recorded in a 5.5–25.5 nm wavelength range, show significant self-absorption of light around 13.5 nm in the 1-μm case, while in the 2-μm case only an opacity-related broadening of the spectral feature at 13.5 nm is observed. This work demonstrates the enhanced capabilities and performance of 2-μm-driven plasmas compared to 1-μm-driven plasmas providing strong motivation for the use of 2-μm lasers as drive lasers in future high-power sources of EUV light.

5.1 Introduction

Laser-produced plasmas containing highly charged tin ions are the light source of choice for state-of-the-art extreme ultraviolet (EUV) lithography [11, 18, 31, 32, 63, 65, 80–82, 90, 103]. Tin is used because no less than five of its charge states (Sn^{10+}–Sn^{14+}) strongly emit in a narrow band around 13.5 nm [19, 21–27, 29, 30, 93] that matches the peak reflectivity of available multilayer optics [10, 40]. The tin ions are bred in a hot (∼30–60 eV) and dense (10^{19}–10^{21} e^-/cm^3) plasma. Starting from mass-limited tin-microdroplets, a low intensity *pre-pulse* deforms the droplets into a shape better suited for interaction with a second high-intensity *main pulse*, used to create the EUV-emitting plasma. This two-step process is crucial for reaching source efficiencies and power levels that allow for the industrial utilization of EUV lithography [34, 69, 104, 105]. Currently, 10.6-μm-wavelength CO_2 gas lasers are used to drive the plasma. Recent simulation studies however have drawn significant attention to the use of a 2 μm main pulse, a wavelength at which high-power solid-state lasers may soon become available [15]. Typical advantages of near-to-mid infrared solid state over gas lasers are their more compact build and higher wall-plug efficiency. Shorter drive laser wavelengths have the additional advantage of a higher coupling efficiency of laser light with the tin plasma. Given a higher critical electron density ($n_c \propto \lambda^{-2}$), the shorter wavelength laser light is absorbed in regions with higher emitter and absorber density. This may benefit the obtainable source brightness but an associated increase in optical depth [89, 106] leads to increased broadening of spectral features outside of the for EUV lithography relevant *in-band* region, defined as a 2% bandwidth centered at 13.5 nm. This broadening may limit the obtainable conversion efficiency (CE) of laser energy into in-band radiation into the backward hemisphere towards the laser origin. Limitations on the spectral performance of EUV sources imposed by optical depth have been studied in detail for plasmas driven by 1-μm Nd:YAG lasers [44, 84, 89]. A 2-μm wavelength, between the widely investigated 1 and 10 μm, is an interesting candidate providing intermediate plasma densities and hence optical depth. In addition to 2-μm systems based on difference frequency generation [92, 106, 107], high-power Big Aperture Thulium (BAT) laser systems, operating at 1.9-μm wavelength, are currently under development [16, 98].

Despite its importance for EUV lithography, literature on the production of in-band radiation from mass-limited, pre-pulse deformed targets remains rather scarce, with the majority of studies to-date focusing on $\lambda = 10\,\mu m$ main pulses (see, e.g., [105, 108–110]). A broad body of literature has investigated experimentally the emission from undeformed liquid tin droplet targets [64, 65, 84, 94], coated spheres [59] or solid-planar targets [49, 52, 62, 111] using 1-μm solid-state lasers. First results from experiments using 2-μm laser light driving plasma from solid-planar tin targets [107] as well as from undeformed liquid tin droplet targets

[106] have recently been presented. Both works demonstrate the potential of the 2-μm drive wavelength, showing a doubling of the obtainable CE over the 1-μm driver, to a 3% level for the solid-planar tin target. At this 3% level the overall conversion efficiency of wall plug power to in-band EUV may be at par with the current CO_2-driven industrial solutions. Literature on industrially-relevant mass-limited deformed targets interacting with either 1- or 2-μm main pulse beams at high CE is however not yet available.

In this chapter, EUV light production from mass-limited tin targets, suitably shaped by a 1-μm laser pre-pulse, is investigated using 1- and 2-μm main pulse laser systems to drive the plasma. First, plasma produced with a 2-μm laser beam is investigated for three different laser intensities and three laser pulse durations. For each laser parameter set a wide range of target diameters (30–350 μm) is investigated and the resulting angular distribution of in-band emission, the efficiency of converting laser light into in-band EUV radiation and overall EUV radiation, as well as the spectral performance of the plasma, are characterized. Secondly, plasmas generated by 1- and 2-μm drive laser light are characterized and compared.

5.2 Experiment

In the experiments, micrometer-sized liquid tin droplets are first irradiated with a relatively low intensity ($\sim 10^9$ W/cm^2), 1-μm wavelength pre-pulse (PP, see Fig. 5.1(a)) from an Nd:YAG laser. The spatial beam profile of this pre-pulse laser is Gaussian with a size of 120 μm at full width at half maximum (FWHM). Its temporal pulse shape has a FWHM of 25.9 ns (see Fig. 5.1(d)). A constant pre-pulse energy of 8.4 mJ was used throughout the experiments. The pre-pulse propels the droplets and deforms them into extended, disk-like targets of diameter d_T [35, 70, 112, 113]. The deformation of droplets having a diameter D and a propulsion velocity U happens on an inertial time scale D/U while the action of surface tension reduces the expansion speed on a longer capillary time scale, eventually causing the collapse of the disk after several microseconds [35]. Typical radial expansion speeds of ∼90 m/s and propulsion velocities of ∼70 m/s are reached in the case of 30 μm droplets.

The produced targets are radially symmetric and thickest in their center with a radially decreasing thickness [112, 113]. Furthermore, target thickness reduces with increasing expansion time. Using the results of Ref. [112], we deduce that targets are produced with thicknesses ranging from $D = 30$ μm at zero expansion time down to ∼50 nm for the largest target diameters obtained at the longest expansion time. The target diameter d_T is precisely controlled via the time delay between pre- and main pulse. The so-produced tin targets are observed under angles of 90° (side view) and 150° (front view) with respect to the laser beam using combina-

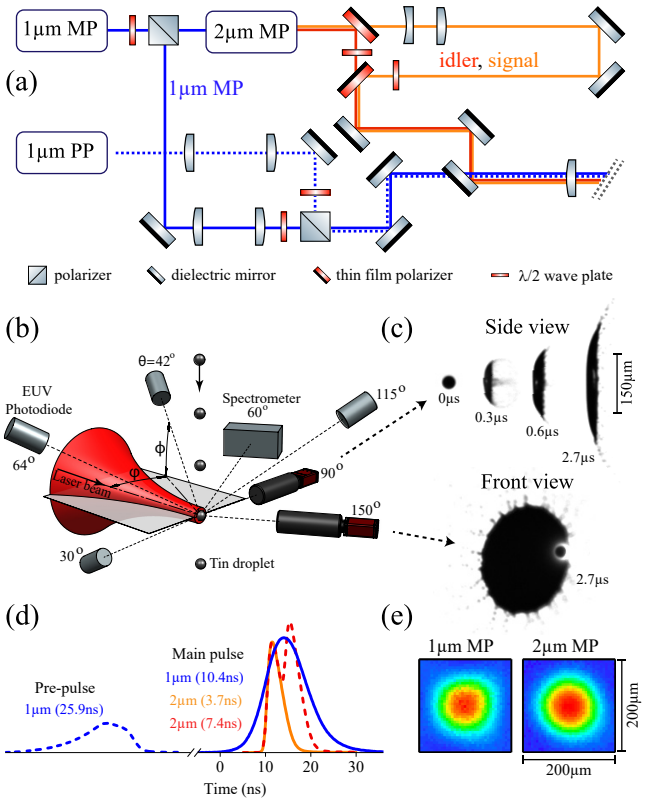

Figure 5.1: (a) Schematic representation of the laser beam setup with pre-pulse (PP) and main pulse (MP) lasers shown. (b) Continuation from (a) showing the locations and angles of the detectors. All angles θ are calculated with respect to the laser-beam propagation axis, with $\cos\theta = \cos\phi\cos\varphi$. (d) Selection of front and side view shadowgraphs of the tin targets used for plasma generation, recorded by the two cameras indicated in (b). (d) Temporal and (e) spatial profiles of the laser beams. For more detail see text.

tions of CCD cameras and long-distance microscopes (see Fig. 5.1(b)). Temporal resolution is achieved by back-lighting the tin targets with spatially and temporally incoherent 560-nm-wavelength pulses of 6 ns duration. Examples of typical targets are shown in Fig. 5.1(c).

After a set time delay the targets are irradiated with high-intensity 2-μm-wavelength laser pulses. The pulses are produced in a master oscillator power amplifier (MOPA) [106, 107] that was built following the work of Arisholm *et al.* [92]. Signal and idler pulses having energies up to 180 mJ each are produced at wavelengths of 1.9 and 2.1 μm, respectively. Depending on the precise experimental conditions, the pulse duration of the MOPA system can vary between 3.7 to 4.6 ns, and the exact, measured pulse durations are stated for each measurement in the following.

For the first set of experiments, the signal beam is removed via polarization optics and only the idler beam of the MOPA is focused onto the tin droplets. The focal spot of the idler beam is Gaussian and has a FWHM of 106 μm (see Fig. 5.1(e)).

In a second set of experiments, the pulse duration of the 2 μm beam is varied between 3.7 ns (idler only) and 7.4 ns (idler and signal) at equal laser intensity. To achieve the longer pulse duration, the signal beam, which is separated from the idler via a thin film polarizer (TFP), is sent into an optical delay line of 1.2 m length. The focusing conditions of the delayed signal beam are matched to those of the idler by adjustment of beam size and collimation via a telescope within the delay line, resulting in a Gaussian focal spot size of 106 μm FWHM for both beams. After collimation adjustment the beams are combined again with a second TFP. The signal energy is adjusted via a $\lambda/2$-waveplate before this second TFP.

To enable a direct comparison of plasmas driven by 1- and 2-μm-wavelength laser pulses, the 1-μm beam of the MOPA pump laser is focused on the tin targets in a third and final set of experiments. The pump laser is a seeded Nd:YAG laser with a temporal Gaussian profile of 10.4 ns (FWHM). Using a telescope the 1-μm pulses are adjusted in size and collimation and a focal spot size of 94×101 μm is achieved close to the dimensions of the 2-μm beam spot. Before focusing on the droplets, the beam energy is adjusted by a combination of a $\lambda/2$ plate and polarizer after which the 1-μm beam is overlapped with the 2-μm beam, just before the final focusing element. Laser intensity is calculated with respect to its peak in space and time according to $I_\mathrm{L} = (2\sqrt{2\ln 2/2\pi})^3 E_\mathrm{L}/abt_\mathrm{p}$, where E_L is the laser energy, a and b are the major and minor axis of the slightly elliptical beam given as FWHM, and t_p is the pulse duration.

The spectral emission from the plasma is recorded using a transmission grating spectrometer [68]. The spectrometer is mounted at an angle of 60° with respect to the laser axis (see Fig. 5.1(b)) and is operated with a 25 μm slit and a 10 000 lines/mm grating. Subsequent to recording the spectra with a CCD camera, a dark exposure is subtracted from the images in order to account for thermal and readout counts on the CCD. Next, spectra are corrected for second-order diffraction

from the grating, the grating's first order diffraction efficiency and the quantum efficiency of the CCD.

The absolute amount of in-band radiation is measured with four photodiode assemblies installed under angles of $\theta = 30$, 42, 64 and 115° with respect to the target's surface normal. The photodiode assemblies use a multilayer mirror near normal incidence to reflect the in-band light onto the photodiode detectors. Remaining optical radiation is filtered by a transmissive Si/Zr coating on the photodiodes. Next, following the approach of Ref. [84] (and analogously to [49] and [75]) the measured in-band energy values are corrected for the respective solid angle and fitted with the monotonous smooth function

$$f(\theta) = (\alpha - \beta)\cos(\theta/2)^{\gamma} + \beta, \tag{5.1}$$

with amplitude α, offset β and power γ. We note that this function differs from the fit function $\sim\cos(\theta)^{\gamma}$ used in Schupp *et al.* [84] in order to capture here the emission under angles $\theta > 90°$ also in cases $\gamma < 1$. The resulting fitted curves, using either fit function, are found to be indistinguishable over the backward hemisphere where $\theta < 90°$. The integral amount of in-band radiation over the hemisphere around the incoming laser beam is then calculated by integration of Eq. (5.1)

$$E_{\mathrm{IB},2\pi} = 2\pi \int_0^{\pi/2} f(\theta)\sin\theta\, d\theta. \tag{5.2}$$

Using this value, CE is defined as $E_{\mathrm{IB},2\pi}/E_{\mathrm{L}}$. We further define an anisotropy factor of the in-band emission to gauge which fraction of in-band light is emitted into the backward hemisphere via $E_{\mathrm{IB},2\pi}/E_{\mathrm{IB},4\pi}$, where $E_{\mathrm{IB},4\pi}$ is obtained by changing the upper integration boundary in Eq. 5.2 to π, hence integrating over all angles. A large anisotropy factor is favorable for industrial application as light-collecting optics typically cover the backward hemisphere.

A second measure for source performance is the spectral purity (SP), defined as the ratio of in-band energy to the total EUV energy. All SP values provided in the following are calculated with respect to the spectral range of 5.5–25.5 nm measured under a 60 degree angle. A third measure, the radiative efficiency η_{rad} of the plasma is defined as the ratio of CE over SP following Ref. [84] and yields the total amount of EUV light emitted in the 5.5–25.5 nm wavelength band per incoming laser energy. In the current work, and in contrast to Ref. [84], η_{rad} is defined using the values measured at 60°, i.e., using the in-band EUV energy emitted per steradian under an angle of 60° (this value is subsequently multiplied with 2π), meaning $(E_{\mathrm{IB},60°}/E_{\mathrm{L}})/\mathrm{SP}$, instead of using CE that is defined over the entire laser-facing hemisphere. This is undertaken because the spectra and hence the SP values are expected to show strong angular dependence for expanded targets [46, 52], a dependence that is further expected to be influenced by the target diameter.

5.3 EUV generation using 2-μm light on preformed targets

In the following, the influence of target diameter, laser intensity and laser pulse duration on CE, SP, η_{rad}, $E_{\mathrm{IB},2\pi}$ and $E_{\mathrm{IB},2\pi}/E_{\mathrm{IB},4\pi}$ are investigated. Further, the spectral emission and angular distribution of the in-band emission are discussed.

5.3.1 Target diameter

To investigate the influence of target size, tin targets of various sizes as produced from pre-pulse-impacted 27-μm-diameter droplets are irradiated with laser pulses having an intensity of 0.6×10^{11} W/cm^2 and a pulse duration of 4.5 ns (downward triangles in Fig. 5.2). Data recorded using higher laser intensities and different pulse lengths are also shown but will be discussed in Sections 5.3.2 and 5.3.3, respectively. Starting from an undeformed droplet target, CE has a low value of approximately 0.15% that almost linearly increases with target diameter (see Fig. 5.2(a)). At diameters of 180 μm and above, CE starts to plateau at a value of approximately 2.6%. This plateau sets in where the target is roughly a factor of 2 larger than the FWHM size of the beam. A similar result was observed for 1-μm-driven plasmas from tin coated glass spheres by Yuspeh *et al.* [60].

An increase in CE with target diameter is expected as an enlarged target diameter increases the geometrical overlap of laser beam and target. This overlap fraction is referred to as energy-on-target (EoT, following the definition in Refs. [35] and [70]). We note that there is a near complete absorption of laser light by the efficient inverse bremsstrahlung mechanism for this wavelength laser light at the here-relevant intensities [70], where laser light geometrically overlaps with the target. For a circular spot, EoT is given by the function $A(1-2^{-d_{\mathrm{T}}^2/d_{\mathrm{L}}^2})$ which is an excellent approximation for the current focal spot shapes (cf. Fig. 5.1(e)), where $d_{\mathrm{L}} = (a+b)/2$. The free fit factor A, the amplitude of the EoT curve, is obtained from a global fit to the asymptotic CE value of all data presented in Fig. 5.2(a) and 5.2(e). The observed dependence of CE on target size is seen to be well approximated by the geometric overlap function (dashed line in Fig. 5.2(a)).

All CE values are calculated from angular-resolved measurements of the plasma's in-band emission and all data points represent the mean over 300 individual laser shots. The angular dependence of the measured in-band energies (see Fig. 5.2(k)) is first fitted with Eq. (5.1) and the CE value is subsequently calculated using the integration result from Eq. (5.2). For better visibility, all curves in Fig. 5.2(k) are normalized at 0°. Eq. (5.1) is seen to accurately describe the angular dependence of the in-band EUV emission. The increase of in-band light observed at a target diameter of 94 μm and under an angle of 42° is however not fully captured by the fit function and this data point may in fact be an outlier.

The reduced emission in the propagation direction of the laser at 180° with

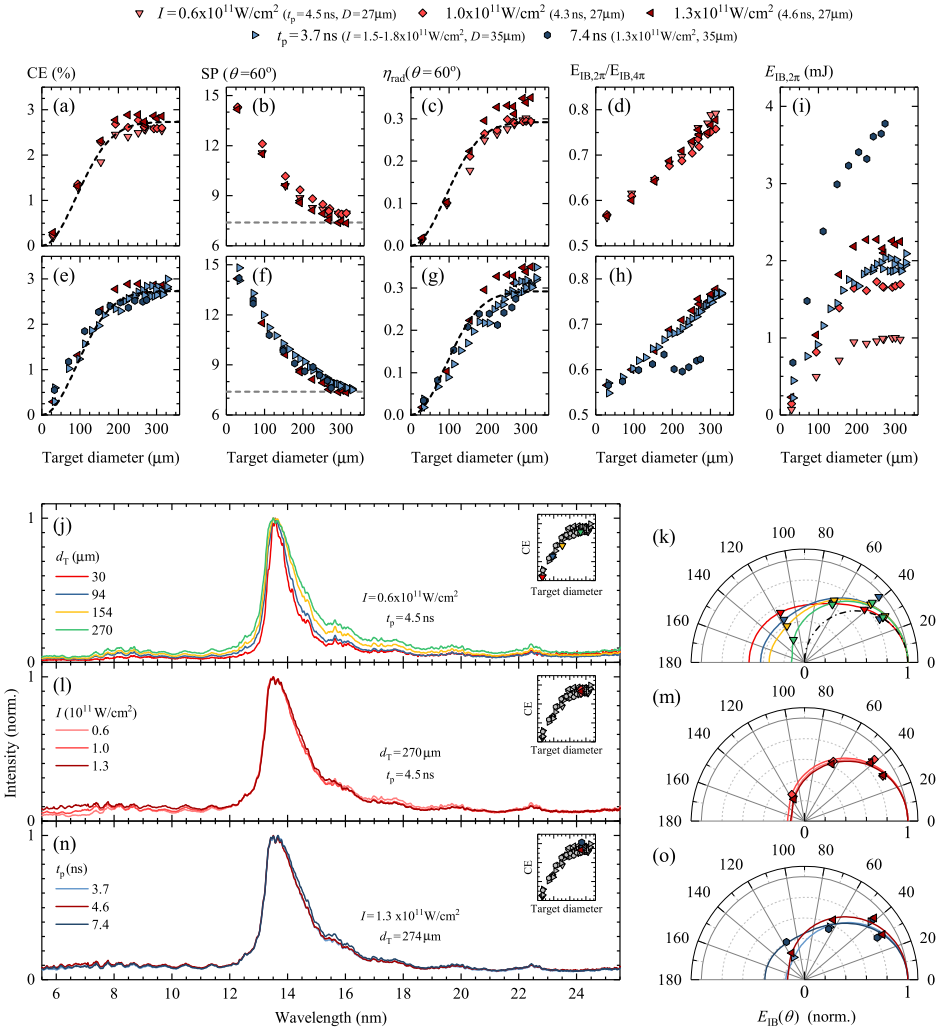

Figure 5.2: Caption on the following page.

Figure 5.2: (Figure on the previous page) Results obtained with a 2-μm drive laser wavelength. (a), (e) CE, (b), (f) SP, (c), (g) η_{rad}, (d), (h) anisotropy factor $E_{\mathrm{IB},2\pi}/E_{\mathrm{IB},4\pi}$ and (i) $E_{\mathrm{IB},2\pi}$, as function of target diameter, for three different intensities and laser pulse durations. SP and η_{rad} are obtained from measurements of the spectrum and in-band energy under a 60° angle. During the intensity scans the idler beam had a slightly longer pulse duration of 4.5 ns (cf. 3.7 ns during pulse duration scan) and the 1.3×10^{11} W/cm^2 scan is shown in the pulse duration scan also. The dashed lines in panels (a), (c), (e), and (g) represent the results of a fit of the geometrical overlap of laser beam and target (EoT). The gray dashed lines in (b) and (f) indicate the SP values from measurements on planar-solid tin targets obtained from [107]. Also shown are normalized spectra versus (j) target size, (l) laser intensity and (n) pulse duration. The corresponding angular dependence of in-band emission, normalized at 0°, is shown in panels (k), (m) and (o). The solid lines depict fits of Eq. (5.1) to the data; the dash-dotted line in (k) indicates the $\cos(\theta)$ dependence of the Lambert cosine law.

increasing target size may be caused by the one-sided heating of the expanded tin target by the laser beam. Plasma emission in this direction is shielded by the target (which is still thought to be present in liquid form during the laser pulse) and only plasma formed on the edge of the target presumably contributes to in-band emission under angles larger than 90°. The dashed line in Fig. 5.2(k) shows Lambert's cosine law for the angular emission from a planar surface. With increasing target diameter the in-band emission starts to converge to this $\cos(\theta)$ dependence, however without fully reaching it. This might be expected because of the 3-dimensional extent of the plasma, causing departure of the emission characteristics from a Lambert-type distribution. Furthermore, emission will always exist at angles larger than 90° from the edge of the plasma unless $d_{\mathrm{T}} \gg d_{\mathrm{L}}$.

Next, the angular in-band distribution is quantified via an anisotropy factor, defined as the ratio of $E_{\mathrm{IB},2\pi}/E_{\mathrm{IB},4\pi}$, meaning the fraction of *all* in-band energy that is emitted into the backward hemisphere of the incoming laser beam, relevant for EUV lithography applications. The anisotropy factor starts at a value of 0.57 for the droplet target, where 0.5 indicates an equal split between both hemispheres (see Fig. 5.2(d)). The anisotropy factor then linearly increases with target diameter up to a value of 0.79, meaning that an ever-larger fraction of the in-band EUV is emitted into the backward hemisphere.

The in-band energy emitted in the 2π hemisphere towards the laser (obtained from multiplying the CE with the laser pulse energy) is shown in Fig. 5.2(i). Naturally, the same trends are observed than in the case of CE. A maximum of ∼1 mJ of in-band EUV energy is produced (per laser shot) for this lowest intensity case.

Fig. 5.2(j) depicts spectra from the lowest intensity case for a succession of four

target diameters. For visibility and ease of comparison the spectra are normalized to their respective maximum values. Similar to previously published work, where a 2-μm laser was used to produce plasma from spherical, undisturbed droplet targets [106], all spectra show a strong emission feature at 13.5 nm originating from transitions in Sn^{8+}–Sn^{14+} ions [18]. Transitions in these charge states further lead to the radiation observed in the 6–12 nm wavelength region [76]. With increasing target diameter, the feature at 13.5 nm widens significantly from 0.8 to 1.5 nm (FWHM). These are values between those of 1-μm-driven low-density plasmas from planar SnO_2 targets of 0.5–1.5 nm [111, 114] and plasmas from solid-planar tin targets of typically 2–3 nm [46]. In Ref. [84] a FWHM of 0.9 nm was reached in the case of a 1-μm-driven plasma on a tin microdroplet target. 10-μm laser-driven tin plasmas typically have a narrower 13.5-nm feature, reaching 0.6 nm (FWHM) [13]. The 2-μm-driven plasma is thus seen to produce spectra with spectral widths typically in between those produced with 1- and 10-μm laser-driven pure tin plasmas.

In contrast to the scaling of CE, SP has its maximum at the smallest target diameter. The highest value shown in Fig. 5.2(b) is 11.5% at a 90 μm diameter down from a maximum value of ∼14% for the case of an undeformed droplet. SP for the undisturbed droplet target for this lowest intensity case is omitted from Fig. 5.2(b) due to the low signal-to-noise ratio in the recorded spectrum. With increasing target diameter SP is observed to decrease monotonously, an effect previously observed for 1-μm beams on droplet targets [84]. Above 200 μm diameter the decrease in SP plateaus towards a value of 7.5% at a 300 μm diameter. These SP values are consistent with Ref. [107], where the SP for planar-solid tin target plasmas was measured at 7.4% (dashed line in panel (b)).

Using these SP values as input, a monotonic increase of η_{rad} with target diameter is observed up to a value of ∼0.3 at a 300 μm target diameter (cf. Fig. 5.2(c)). Also indicated is the dependence of EoT on target size, now with an amplitude fit value of 0.29 (dashed curve). The here measured maximum radiative efficiency at 60° is slightly lower than a value of approximately 0.4 measured for an extended solid-planar target [107]. This difference originates from the slightly higher in-band emission at 60° measured on the planar target and may be explained by the smaller beam-spot size in the planar target case that allows for the in-band emission to escape more freely. Over the entire range of target diameters, the radiative efficiency qualitatively follows the EoT trend.

At this point, it is worthwhile to consider the fact that both overall CE and η_{rad} qualitatively follow the EoT curve, describing the increasing geometrical overlap between an enlarging target and laser beam spot. However, we also note that the SP, which serves as input for calculating η_{rad}, monotonically decreases with increasing target size. This apparent contradiction is resolved when considering the angular dependence of the plasma emission, with the increasing anisotropy factor serving to offset the decrease in SP with increasing target size (cf. Fig. 5.2(b)

and 5.2(d)).

5.3.2 Laser intensity

Next, target diameter scans are performed for two higher laser intensities of 1.0 and 1.3×10^{11} W/cm^2. The CE curves for all three laser intensities show a trend very similar to the 0.6×10^{11} W/cm^2 intensity case presented in Sec. 5.3.1 (see Fig. 5.2(a)). For all target diameters, CE values are found to be slightly higher at higher laser intensities. The maximum CE value at large target diameters increases modestly from 2.6 to 2.9%. The angular distribution of in-band emission is observed to be independent of laser intensity within the scanned range (cf. Fig. 5.2(m)). Given the constant maximum CE values, the amount of in-band radiation increases linearly with increasing laser intensity, with up to 2.3 mJ of in-band light obtained for the highest intensity case (see Fig. 5.2(i)).

In Fig. 5.2(l) normalized spectra for a target diameter of 270 μm are shown. For all spectra, the 8–25 nm region looks remarkably alike. The most prominent difference between the spectra is seen in the 5–8 nm region where the amount of radiation is observed to increase with increasing laser intensity. This emission could stem from charge states Sn^{14+} (and above) as well as from an increased fraction of light being emitted from electronic states having higher excitation energies. The corresponding SP values are shown in Fig. 5.2(b). All laser intensity cases follow the same trend. The maximum SP value for the two higher intensities is 14.5% and is reached at the smallest target diameter, i.e., the undeformed droplet target. SP steadily decreases with increasing target size, and levels off at a value of up to 8% depending on intensity. Even though the differences in SP are small, we do note that optimum SP values are observed for an intermediate intensity of 1.0×10^{11} W/cm^2.

Given the similar scaling of CE and SP with target diameter for the three laser intensities, the radiative efficiency in Fig. 5.2(c) closely follows the 0.6×10^{11} W/cm^2 results, with a slightly higher value of 0.35 obtained for the highest intensity case.

No significant changes are thus observed in the scaling of emission characteristics with target size when changing laser intensity and in-band EUV emission is seen to exhibit a linear dependence on laser energy.

5.3.3 Pulse duration

Lastly, the laser pulse duration is varied from 3.7 to 7.4 ns (blue markers in Fig. 5.2) by combining signal and idler beams while delaying the signal with respect to the idler pulse. To obtain identical focal spot conditions for both beams, the beam size of the signal beam is carefully matched to that of the idler beam by means of a telescope. The energy of both beams is individually controlled via combinations of

$\lambda/2$-plates and TFPs. Signal and idler beams are set to have equal energies. The resulting temporal pulse profile is shown in Fig. 5.1(d). Measurements are taken with 35-μm-diameter droplets, slightly larger than those used during the laser intensity scan. We note that no dependence of CE with initial droplet diameter is observed for target size scans performed for a range of droplet diameters from 19–45 μm diameter as long as the target thickness is sufficient to supply tin throughout the laser pulse. As an additional data set for the laser pulse duration we add the high-intensity (1.3×10^{11} W/cm^2) scan from the previous Sec. 5.3.2 that had slightly longer idler pulse duration of 4.6 ns due to slightly different settings of the MOPA system.

Again, CE is found to follow the same trend with increasing target diameter as described in Sec. 5.3.1. A slightly higher maximum CE value of 2.9% is observed for the short and intermediate pulse durations, compared with a value of 2.6% obtained for the longest pulse duration. We note that the small observed changes in CE may lie within the systematic uncertainties of the experiment. The rather small changes in CE with pulse duration, as well as laser intensity, imply a near-linear scaling of in-band energy with laser energy. The in-band energy (Fig. 5.2(i)) indeed almost doubles when doubling the laser pulse duration, and up to 3.8 mJ of in-band energy are measured per pulse. The angular distributions of in-band EUV emission are all rather similar up to an angle of 64° from which point the 7.4-ns case shows increased emission. The anisotropy factor in this 7.4-ns case (see Fig. 5.2(h)) roughly follows the one of the short and medium pulse duration cases up to a target diameter of 180 μm, after which it remains roughly constant at values around 0.6. This observed difference may be attributed to an increased EUV emission volume (which increases pulse duration), partially extending beyond the liquid disk target, which enables radiating into the forward hemisphere.

The recorded spectra, shown in Fig. 5.2(n), are remarkably similar when comparing the different laser pulse lengths. The only minor visible difference is the slightly wider main emission feature in the 7.4 ns case. SP also remains virtually independent of laser pulse duration and follows the same trend as discussed as in Sec. 5.3.1. For the longest pulse duration case, we note that the decrease in SP with increasing target size is no longer fully compensated by increases in the anisotropy factor and this is reflected in slightly lower overall CE values.

No major changes were thus observed in the scaling of emission characteristics with target size when changing laser pulse length, besides a levelling off of the anisotropy factor for the longest pulse length. In-band EUV emission is also here seen to follow linearly the input laser energy.

5.4 EUV generation using 1- and 2-μm laser light

In the second experiment, plasma is produced using the 1-μm laser beam at an intensity of 2.3×10^{11} W/cm^2. This choice of laser intensity yields identical emission features in the 5–12 nm region compared to the 1.0×10^{11} W/cm^2 intensity at 2 μm. Equivalent spectral features ensure a similar charge state distribution of the plasma as each feature is charge-state specific. The factor of 2.3 difference in relative intensity is in agreement with the intensity ratios observed for droplet targets [106] as well as for planar-solid targets [107]. Given the fact that no significant impact of pulse duration on CE, SP, and η_{rad} was established for the 2-μm data (Sec. 5.3), the current comparison of a 4.3 ns, 2 μm pulse with a 10.4 ns, 1 μm one is apt.

As shown in Fig. 5.3(a), CE is found to increase monotonically with increasing target size in the 2-μm case until the laser beam reaches full overlap with the target, as described in Sec. 5.3. For the smallest target diameter, i.e. an undeformed droplet, CE is significantly higher in the 1-μm case because of an increase in absorbed laser light fraction caused by the longer 10.4 ns laser pulse duration [84] and similar CE values are expected on an undeformed droplet for identical laser conditions [115]. In addition to the longer pulse duration, differences in the temporal shape may contribute to the observed difference in CE for the smallest target sizes: the slowly rising intensity of the Gaussian profile of the 1-μm pulse would lead to further plasma expansion and, thus, to an increased overlap between absorbing material and the laser beam spot. This effect becomes insignificant with increasing target diameter, with CE values exceeding the 1-μm case for target diameters greater than 50 μm. The 1-μm CE is found to increase in a near-linear fashion up to a value of close to 1% at 156 μm target diameter, where the scan ends because of technical problems of the PP laser. From measurements on planar-solid targets, CE values of 1.8% were inferred from measurements performed at a representative angle of 60° for a shorter 4.8 ns pulse duration and a slightly smaller circular 66 μm diameter (FWHM) spot [107]. Following the trend of the EoT curve fit to the data (dashed line), from which the prefactor is obtained, slightly lower CE values of 1.2% are expected in the current case, which may be explained by the longer duration and larger spot size in this study. In the 2-μm case, CE values measured on planar-solid targets (effectively an infinitely extended disk target) reach 3%, in line with the here-observed values of up to 2.9%.

The angular dependence of the in-band EUV emission for the droplet target (see Fig. 5.3(g)) is very similar for both drive lasers and is consistent with previous studies where a 1-μm laser was used to drive the LPP from a droplet target [64, 75, 84]. The similarities in the angular distributions is in line with a previous study by Chen *et al.* [66] where only minor changes in emission anisotropy were found between 1- and 10-μm-driven droplet plasmas.

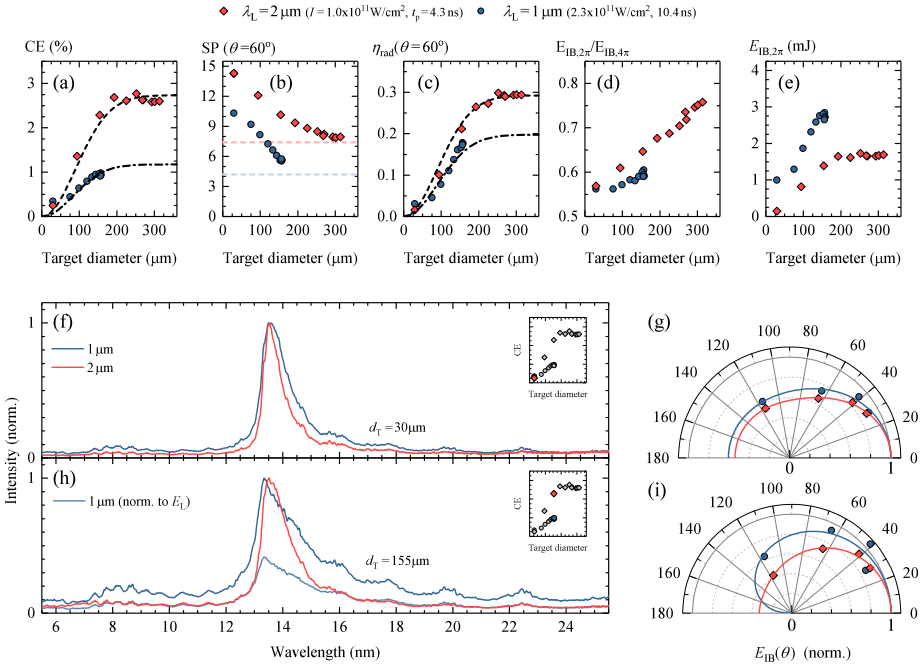

Figure 5.3: Comparison of results for drive laser beams of 1- and 2-µm wavelength at intensities of 2.3 and 1.0×10^{11} W/cm^2, respectively. (a) CE, (b) SP, (c) η_{rad}, (d) anisotropy factor $E_{\mathrm{IB},2\pi}/E_{\mathrm{IB},4\pi}$ and (e) $E_{\mathrm{IB},2\pi}$, as function of target diameter. The dash-dotted and dashed lines in panels (a) and (c) represent the results of a fit of the geometrical overlap of laser beam and target. The dashed lines in (b) indicate the SP values from planar-solid tin targets [107]. The spectral emission of plasmas for a target diameter of (f) 30 µm (droplet target) and (h) 155 µm (disk target) are shown normalized to their respective peak intensities. In (h) the 1-µm spectrum is shown a second time, now normalized to laser energy (light blue curve). The at 0° normalized angular dependencies of the in-band EUV emission, corresponding to the spectra shown in (f) and (h), are shown in (g) and (i), respectively. Solid lines depict fits of Eq. (5.1) to the data.

For the 270 μm target diameter in the 2-μm case (see Fig. 5.3(i)), the in-band emission monotonously decreases with increasing angle whereas in the 1-μm case the maximum in-band emission is observed not at 0°, but at larger angles between 30° and 115°. A similar preference for emission of in-band radiation at an angle of 45° over a 30° angle was also observed for a planar-solid target [94].

For the droplet target the anisotropy factor attains a value of 0.57, identical for both laser wavelength cases (see Fig. 5.3(d)). The anisotropy factor in the 2-μm case linearly increases with increasing target diameter as discussed in Sec. 5.3.2. In the 1-μm case the anisotropy factor increases more modestly with target diameter. Uncertainties related to the relatively poor fit of the anisotropy function to the 1-μm data, which unexpectedly converges to 0 at 180°, may lead to a slight systematic overestimation of the anisotropy factor.

The in-band energy values displayed in Fig. 5.3(e) trivially follow the scaling of CE. In the 1-μm case, values of almost 3 mJ per pulse are achieved as a result of the large pulse energies. We note that higher in-band energy was obtained in Sec. 5.3 for the 2-μm driver using significantly less laser energy (viz. 123 vs 291 mJ pulse energy) at equal target diameters demonstrating here the significant advantage of the 2x longer drive laser wavelength.

For undeformed droplet targets, the spectra for the 2-μm case show a much narrower main emission feature and, relative to the 13.5-nm peak, less out-of-band radiation is emitted in the 2-μm case (see Fig 5.3(f)). These observations are consistent with earlier results [84, 106]. With increasing target diameter the differences in the spectral emission between the two drive laser wavelengths become even more pronounced. In the 2-μm case, the main emission feature simply broadens with target diameter (see Fig. 5.2(h)), in line with expectations from an associated increase in optical depth [89]. In the 1-μm case, the shape of the main emission feature changes drastically due to strong self-absorption, causing the emission maximum to shift to shorter wavelength. This 'missing' emission in the main feature in the 1-μm case is qualitatively well explained by absorption of in-band radiation from a hotter plasma zone by a colder less emissive plasma zone [96, 107].

SP is found to decrease monotonously with increasing target diameter for both wavelength cases (see Fig. 5.3(b)). In the 1-μm case, the SP for small target diameters is on the order of 10%, and is observed to decrease more rapidly than its 2-μm counterpart down to 5.5% at a 156 μm diameter. From measurements on planar-solid tin targets, SP values as low as 4% are expected in the 1-μm case which may be taken as the asymptotic value of SP towards infinite target size [107].

Radiative efficiency, measured at an angle of 60°, is very similar in both wavelength cases (see panel (c)). For the 1-μm case, the fit of the EoT function (dash-dotted line) does not fully capture the data and an amplitude greater than a value of 0.2 obtained from the fit cannot be excluded.

No major differences between the radiative efficiencies and the anisotropy factors are observed. Comparing the two drive laser wavelength cases, the differences in CE are largely attributable to the decrease in SP. This link between CE and SP further supports the findings of Behnke *et al.* [107], where experiments on solid tin targets demonstrated that plasmas driven by 1-μm laser light exhibit strong EUV self-absorption which is absent in the 2-μm spectra. This makes 2-μm-driven plasmas the more efficient emitter of in-band EUV radiation. We note that conversion efficiencies of up to 3% can in fact be achieved for the 1-μm drive laser case for a homogeneous heating of undeformed droplet targets with several 10-ns-long, spatially flattop-shaped laser pulses [84]. Thus, on one hand, the current limitations to CE for the 1-μm drive laser case for extended disk targets may be eased using alternate target and illumination designs. On the other hand, even larger CE values for the 2-μm drive laser case may be obtained from optimally shaped targets homogeneously heated by a long, flattop laser pulse.

5.5 Conclusions

We have studied plasmas produced from laser pre-pulse preformed liquid tin disk targets with diameters ranging 30–350 μm using 1- and 2-μm drive laser systems. For the 2-μm driver, the conversion efficiency of laser energy to EUV radiation closely follows the fraction of the laser energy absorbed by the tin target and CE values of up to 3% are obtained for the largest targets. Conversion efficiency (CE), spectral purity (SP), radiative efficiency (η_{rad}), and spectral emission are found to be nearly independent of laser intensity and laser pulse duration in the here-studied parameter range. Consequently, a linear increase of in-band radiation towards the backward hemisphere with laser energy is observed when increasing either parameter and further scaling of in-band output per tin target with laser intensity and pulse duration may be possible at little to no cost regarding CE.

Direct comparison of the emission characteristics of 1- and 2-μm-driven plasmas reveals significantly lower CE values for the 1-μm driver under the current experimental conditions when using extended disk targets. The lower 1-μm CE is explained by the particularly strong self-absorption of the emitted EUV radiation in the 1-μm-driven plasma. Further improvements in terms of CE may be obtainable by homogeneous heating of suitably shaped tin targets with longer laser pulses leading to full evaporation of the then truly 'mass-limited' tin target. Such future studies should include research on the influence of laser pulse duration, intensity and laser wavelength on any possible fast ionic or liquid debris that may harm nearby optics elements in possible future industrial EUV light sources based on 2-μm-laser-driven tin plasmas.

References

[1] R. G. Arns, "The other transistor: early history of the metal-oxide semiconductor field-effect transistor", Eng. Sci. Educ. J. **7**, 233–240 (1998).

[2] L. J. Edgar, *Method and apparatus for controlling electric currents*, US Patent 1,745,175, Jan. 1930.

[3] J. Bardeen and W. H. Brattain, "The transistor, a semi-conductor triode", Phys. Rev. **74**, 230–231 (1948).

[4] C.-T. Sah, "Evolution of the MOS transistor—from conception to VLSI", Proc. IEEE **76**, 1280–1326 (1988).

[5] G. E. Moore, "Progress in digital integrated electronics", Proc. IEDM Tech. Dig. **11**, 11–13 (1975).

[6] G. E. Moore, "Cramming More Components Onto Integrated Circuits", Proc. IEEE **86**, 82–85 (1998).

[7] T. N. Theis and H.-S. Philip Wong, "The end of moore's law: A new beginning for information technology", Comput. Sci. Eng. **19**, 41–50 (2017).

[8] I. Fomenkov, *EUV Source for Lithography in HVM: performance and prospects*, EUV Source Workshop 2019, presented: November 5, 2019.

[9] C. De Young, *EUV: Enabling cost efficiency, tech innovation and future industry growth*, BAML 2019 APAC TMT Conference, presented: March 20, 2019.

[10] S. Bajt, J. B. Alameda, T. W. Barbee Jr., W. M. Clift, J. A. Folta, B. B. Kaufmann, and E. A. Spiller, "Improved reflectance and stability of Mo/Si multilayers", Opt. Eng. **41**, 1797–1804 (2002).

[11] M. Purvis, I. V. Fomenkov, A. A. Schafgans, M. Vargas, S. Rich, Y. Tao, S. I. Rokitski, M. Mulder, E. Buurman, M. Kats, J. Stewart, A. D. LaForge, C. Rajyaguru, G. Vaschenko, A. I. Ershov, R. J. Rafac, M. Abraham, D. C. Brandt, and D. J. Brown, "Industrialization of a robust EUV source for high-volume manufacturing and power scaling beyond 250 W", in EUV Lithography IX, Vol. 10583 (SPIE, 2018), 1058327.

[12]F. Torretti, J. Sheil, R. Schupp, M. M. Basko, M. Bayraktar, R. A. Meijer, S. Witte, W. Ubachs, R. Hoekstra, O. O. Versolato, A. J. Neukirch, and J. Colgan, "Prominent radiative contributions from multiply-excited states in laser-produced tin plasma for nanolithography", Nat. Commun. **11**, 2334 (2020).

[13]M. van de Kerkhof, F. Liu, M. Meeuwissen, X. Zhang, M. Bayraktar, R. de Kruif, and N. Davydova, "High-power EUV lithography: spectral purity and imaging performance", J. Micro Nanolithogr. MEMS MOEMS **19**, 033801 (2020).

[14]M. M. Marinak, G. D. Kerbel, N. A. Gentile, O. Jones, D. Munro, S. Pollaine, T. R. Dittrich, and S. W. Haan, "Three-dimensional HYDRA simulations of National Ignition Facility targets", Phys. Plasmas **8**, 2275–2280 (2001).

[15]S. Langer, H. Scott, T. Galvin, E. Link, B. Regan, and C. Siders, *Simulations of Laser Driven EUV Sources – the Impact of Laser Wavelength*, EUVL Workshop 2020, presented: June 11, 2020.

[16]E. Sistrunk, D. A. Alessi, A. Bayramian, K. Chesnut, A. Erlandson, T. C. Galvin, D. Gibson, H. Nguyen, B. Reagan, K. Schaffers, C. W. Siders, T. Spinka, and C. Haefner, "Laser Technology Development for High Peak Power Lasers Achieving Kilowatt Average Power and Beyond", in *Short-pulse High-energy Lasers and Ultrafast Optical Technologies*, Vol. 11034, edited by P. Bakule and C. L. Haefner (SPIE, 2019), 1–8.

[17]M. M. Basko, J. Maruhn, and A. Tauschwitz, "Development of a 2D radiation-hydrodynamics code RALEF for laser plasma simulations", GSI report **1**, 410 (2010).

[18]G. O'Sullivan, B. Li, R. D'Arcy, P. Dunne, P. Hayden, D. Kilbane, T. McCormack, H. Ohashi, F. O'Reilly, P. Sheridan, E. Sokell, C. Suzuki, and T. Higashiguchi, "Spectroscopy of highly charged ions and its relevance to EUV and soft x-ray source development", J. Phys. B: At. Mol. Opt. Phys. **48**, 144025 (2015).

[19]V. I. Azarov and Y. N. Joshi, "Analysis of the $4d^7$–$4d^6 5p$ transition array of the eighth spectrum of tin: Sn VIII", J. Phys. B: At. Mol. Opt. Phys. **26**, 3495–3514 (1993).

[20]W. Svendsen and G. O'Sullivan, "Statistics and characteristics of xuv transition arrays from laser-produced plasmas of the elements tin through iodine", Phys. Rev. A **50**, 3710–3718 (1994).

[21]S. S. Churilov and A. N. Ryabtsev, "Analyses of the Sn IX–Sn XII spectra in the EUV region", Phys. Scr. **73**, 614–619 (2006).

[22]S. S. Churilov and A. N. Ryabtsev, "Analysis of the $4p^6 4d^7$–$(4p^6 4d^6 4f + 4p^5 4d^8)$ transitions in the Sn VIII spectrum", Opt. Spectrosc. **100**, 660–666 (2006).

[23]S. S. Churilov and A. N. Ryabtsev, "Analysis of the spectra of In XII–XIV and Sn XIII–XV in the far-VUV region", Opt. Spectrosc. **101**, 169–178 (2006).

[24]A. N. Ryabtsev, É. Ya. Kononov, and S. S. Churilov, "Spectra of rubidium-like Pd X–Sn XIV ions", Opt. Spectrosc. **105**, 844–850 (2008).

[25]I. Yu. Tolstikhina, S. S. Churilov, A. N. Ryabtsev, and K. N. Koshelev, "Atomic tin data", in *EUV sources for lithography*, edited by V. Bakshi (SPIE press Bellingham, Washington, 2006) Chap. 4, 113–148.

[26]R. D'Arcy, H. Ohashi, S. Suda, H. Tanuma, S. Fujioka, H. Nishimura, K. Nishihara, C. Suzuki, T. Kato, F. Koike, J. White, and G. O'Sullivan, "Transitions and the effects of configuration interaction in the spectra of Sn XV–Sn XVIII", Phys. Rev. A **79**, 042509 (2009).

[27]H. Ohashi, S. Suda, H. Tanuma, S. Fujioka, H. Nishimura, A. Sasaki, and K. Nishihara, "EUV emission spectra in collisions of multiply charged Sn ions with He and Xe", J. Phys. B: At. Mol. Opt. Phys. **43**, 065204 (2010).

[28]A. Windberger, F. Torretti, A. Borschevsky, A. Ryabtsev, S. Dobrodey, H. Bekker, E. Eliav, U. Kaldor, W. Ubachs, R. Hoekstra, J. R. Crespo López-Urrutia, and O. O. Versolato, "Analysis of the fine structure of Sn^{11+}–Sn^{14+} ions by optical spectroscopy in an electron-beam ion trap", Phys. Rev. A **94**, 012506 (2016).

[29]J. Colgan, D. P. Kilcrease, J. Abdallah, M. E. Sherrill, C. J. Fontes, P. Hakel, and G. S. J. Armstrong, "Atomic structure considerations for the low-temperature opacity of Sn", High Energy Density Phys. **23**, 133–137 (2017).

[30]F. Torretti, A. Windberger, A. Ryabtsev, S. Dobrodey, H. Bekker, W. Ubachs, R. Hoekstra, E. V. Kahl, J. C. Berengut, J. R. Crespo López-Urrutia, and O. O. Versolato, "Optical spectroscopy of complex open-4*d*-shell ions Sn^{7+}–Sn^{10+}", Phys. Rev. A **95**, 042503 (2017).

[31]V. Y. Banine, K. N. Koshelev, and G. H. P. M. Swinkels, "Physical processes in EUV sources for microlithography", J. Phys. D: Appl. Phys. **44**, 253001 (2011).

[32]J. Benschop, V. Banine, S. Lok, and E. Loopstra, "Extreme ultraviolet lithography: Status and prospects", J. Vac. Sci. Technol. B **26**, 2204–2007 (2008).

[33]Y. Kawasuji, K. M. Nowak, T. Hori, T. Okamoto, H. Tanaka, Y. Watanabe, T. Abe, T. Kodama, Y. Shiraishi, H. Nakarai, T. Yamazaki, S. Okazaki, T. Saitou, H. Mizoguchi, and Y. Shiraishi, "Key components technology update of the 250W high-power LPP-EUV light source", in SPIE Advanced Lithography, Vol. 10143 (SPIE, 2017), 101432G.

[34]I. Fomenkov, D. Brandt, A. Ershov, A. Schafgans, Y. Tao, G. Vaschenko, S. Rokitski, M. Kats, M. Vargas, M. Purvis, R. Rafac, B. La Fontaine, S. De Dea, A. LaForge, J. Stewart, S. Chang, M. Graham, D. Riggs, T. Taylor, M. Abraham, and D. Brown, "Light sources for high-volume manufacturing EUV lithography: technology, performance, and power scaling", Adv. Opt. Techn. **6**, 173–186 (2017).

[35]D. Kurilovich, A. L. Klein, F. Torretti, A. Lassise, R. Hoekstra, W. Ubachs, H. Gelderblom, and O. O. Versolato, "Plasma propulsion of a metallic microdroplet and its deformation upon laser impact", Phys. Rev. Appl. **6**, 014018 (2016).

[36]D. Kurilovich, T. de Faria Pinto, F. Torretti, R. Schupp, J. Scheers, A. S. Stodolna, H. Gelderblom, K. S. E. Eikema, S. Witte, W. Ubachs, R. Hoekstra, and O. O. Versolato, "Expansion Dynamics after Laser-Induced Cavitation in Liquid Tin Microdroplets", Phys. Rev. Applied **10**, 054005 (2018).

[37]M. S. Krivokorytov, A. Yu. Vinokhodov, Yu. V. Sidelnikov, V. M. Krivtsun, V. O. Kompanets, A. A. Lash, K. N. Koshelev, and V. V. Medvedev, "Cavitation and spallation in liquid metal droplets produced by subpicosecond pulsed laser radiation", Phys. Rev. E **95**, 031101 (2017).

[38]S. Yu. Grigoryev, B. V. Lakatosh, M. S. Krivokorytov, V. V. Zhakhovsky, S. A. Dyachkov, D. K. Ilnitsky, K. P. Migdal, N. A. Inogamov, A. Yu. Vinokhodov, V. O. Kompanets, Yu. V. Sidelnikov, V. M. Krivtsun, K. N. Koshelev, and V. V. Medvedev, "Expansion and Fragmentation of a Liquid-Metal Droplet by a Short Laser Pulse", Phys. Rev. Appl. **10**, 064009 (2018).

[39]V. Bakshi, ed., *EUV Lithography*, 2nd Edition (SPIE press Bellingham, Washington, 2018).

[40]Q. Huang, V. Medvedev, R. van de Kruijs, A. Yakshin, E. Louis, and F. Bijkerk, "Spectral tailoring of nanoscale EUV and soft x-ray multilayer optics", Appl. Phys. Rev. **4**, 011104 (2017).

[41]M. M. Basko, V. G. Novikov, and A. S. Grushin, "On the structure of quasi-stationary laser ablation fronts in strongly radiating plasmas", Phys. Plasmas **22**, 053111 (2015).

[42]P. Mora, "Theoretical model of absorption of laser light by a plasma", Phys. Fluids **25**, 1051–1056 (1982).

[43]T. W. Johnston and J. M. Dawson, "Correct values for high-frequency power absorption by inverse bremsstrahlung in plasmas", Phys. Fluids **16**, 722–722 (1973).

[44]S. Fujioka, H. Nishimura, K. Nishihara, A. Sasaki, A. Sunahara, T. Okuno, N. Ueda, T. Ando, Y. Tao, Y. Shimada, K. Hashimoto, M. Yamaura, K. Shigemori, M. Nakai, K. Nagai, T. Norimatsu, T. Nishikawa, N. Miyanaga, Y. Izawa, and K. Mima, "Opacity Effect on Extreme Ultraviolet Radiation from Laser-Produced Tin Plasmas", Phys. Rev. Lett. **95**, 235004 (2005).

[45]H. Tanaka, A. Matsumoto, K. Akinaga, A. Takahashi, and T. Okada, "Comparative study on emission characteristics of extreme ultraviolet radiation from CO_2 and Nd:YAG laser-produced tin plasmas", Appl. Phys. Lett. **87**, 041503 (2005).

[46]P. Hayden, A. Cummings, N. Murphy, G. O'Sullivan, P. Sheridan, J. White, and P. Dunne, "13.5 nm extreme ultraviolet emission from tin based laser produced plasma sources", J. Appl. Phys. **99**, 093302 (2006).

[47]J. White, P. Dunne, P. Hayden, F. O'Reilly, and G. O'Sullivan, "Optimizing 13.5 nm laser-produced tin plasma emission as a function of laser wavelength", Appl. Phys. Lett. **90**, 181502 (2007).

[48]R. C. Spitzer, T. J. Orzechowski, D. W. Phillion, R. L. Kauffman, and C. Cerjan, "Conversion efficiencies from laser-produced plasmas in the extreme ultraviolet regime", J. Appl. Phys. **79**, 2251–2258 (1996).

[49]T. Ando, S. Fujioka, H. Nishimura, N. Ueda, Y. Yasuda, K. Nagai, T. Norimatsu, M. Murakami, K. Nishihara, N. Miyanaga, Y. Izawa, K. Mima, and A. Sunahara, "Optimum laser pulse duration for efficient extreme ultraviolet light generation from laser-produced tin plasmas", Appl. Phys. Lett. **89**, 151501 (2006).

[50]Y. Tao, S. S. Harilal, M. S. Tillack, K. L. Sequoia, B. O'Shay, and F. Najmabadi, "Effect of focal spot size on in-band 13.5 nm extreme ultraviolet emission from laser-produced Sn plasma", Opt. Lett. **31**, 2492–2494 (2006).

[51]S. A. George, W. T. Silfvast, K. Takenoshita, R. T. Bernath, C.-S. Koay, G. Shimkaveg, and M. C. Richardson, "Comparative extreme ultraviolet emission measurements for lithium and tin laser plasmas", Opt. Lett. **32**, 997–999 (2007).

[52]O. Morris, F. O'Reilly, P. Dunne, and P. Hayden, "Angular emission and self-absorption studies of a tin laser produced plasma extreme ultraviolet source between 10 and 18 nm", Appl. Phys. Lett. **92**, 231503 (2008).

[53]K. L. Sequoia, "Extreme-ultraviolet radiation transport in small scale length laser-produced tin plasmas", PhD thesis (UC San Diego, 2009).

[54]Y. Tao, Y. Ueno, S. Yuspeh, R. Burdt, M. S. Tillack, and F. Najmabadi, "Investigation on the interaction of long duration Nd:YAG laser pulse with Sn plasma for an EUV metrology source", in EUV Lithography II, Vol. 7969 (SPIE, 2011), 796930.

[55]A. Roy, S. Murtaza Hassan, S. S. Harilal, A. Endo, T. Mocek, and A. Hassanein, "Extreme ultraviolet emission and confinement of tin plasmas in the presence of a magnetic field", Phys. Plasmas **21**, 053106 (2014).

[56]A. Roy, G. Arai, H. Hara, T. Higashiguchi, H. Ohashi, A. Sunahara, B. Li, P. Dunne, G. O'Sullivan, T. Miura, T. Mocek, and A. Endo, "Evolution of laser-produced Sn extreme ultraviolet source diameter for high-brightness source", Appl. Phys. Lett. **105**, 074103 (2014).

[57]M. G. Su, Q. Min, S. Q. Cao, D. X. Sun, P. Hayden, G. O'Sullivan, and C. Z. Dong, "Evolution analysis of EUV radiation from laser-produced tin plasmas based on a radiation hydrodynamics model", Sci. Rep. **7**, 45212 (2017).

[58]S. Fujioka, H. Nishimura, K. Nishihara, M. Murakami, Y.-G. Kang, Q. Gu, K. Nagai, T. Norimatsu, N. Miyanaga, Y. Izawa, and K. Mima, "Properties of ion debris emitted from laser-produced mass-limited tin plasmas for extreme ultraviolet light source applications", Appl. Phys. Lett. **87**, 241503 (2005).

[59]Y. Shimada, H. Nishimura, M. Nakai, K. Hashimoto, M. Yamaura, Y. Tao, K. Shigemori, T. Okuno, K. Nishihara, T. Kawamura, A. Sunahara, T. Nishikawa, A. Sasaki, K. Nagai, T. Norimatsu, S. Fujioka, S. Uchida, N. Miyanaga, Y. Izawa, and C. Yamanaka, "Characterization of extreme ultraviolet emission from laser-produced spherical tin plasma generated with multiple laser beams", Appl. Phys. Lett. **86**, 051501 (2005).

[60]S. Yuspeh, K. L. Sequoia, Y. Tao, M. S. Tillack, R. Burdt, and F. Najmabadi, "Optimization of the size ratio of Sn sphere and laser focal spot for an extreme ultraviolet light source", Appl. Phys. Lett. **93**, 221503 (2008).

[61]S. Yuspeh, Y. Tao, R. A. Burdt, M. S. Tillack, Y. Ueno, and F. Najmabadi, "Dynamics of laser-produced Sn microplasma for a high-brightness extreme ultraviolet light source", Appl. Phys. Lett. **98**, 201501 (2011).

[62]J. R. Freeman, S. S. Harilal, B. Verhoff, A. Hassanein, and B. Rice, "Laser wavelength dependence on angular emission dynamics of Nd:YAG laser-produced Sn plasmas", Plasma Sources Sci. Technol. **21**, 055003 (2012).

[63]A. Yu. Vinokhodov, M. S. Krivokorytov, Yu. V. Sidelnikov, V. M. Krivtsun, V. V. Medvedev, and K. N. Koshelev, "Droplet-based, high-brightness extreme ultraviolet laser plasma source for metrology", J. Appl. Phys. **120**, 163304 (2016).

[64]A. Z. Giovannini and R. S. Abhari, "Three-dimensional extreme ultraviolet emission from a droplet-based laser-produced plasma", J. Appl. Phys. **114**, 033303 (2013).

[65]A. Z. Giovannini and R. S. Abhari, "Effects of the dynamics of droplet-based laser-produced plasma on angular extreme ultraviolet emission profile", Appl. Phys. Lett. **104**, 194104 (2014).

[66]H. Chen, X. Wang, L. Duan, H. Lan, Z. Chen, D. Zuo, and P. Lu, "Angular distribution of ions and extreme ultraviolet emission in laser-produced tin droplet plasma", J. Appl. Phys. **117**, 193302 (2015).

[67]S. J. Goh, H. J. M. Bastiaens, B. Vratzov, Q. Huang, F. Bijkerk, and K. J. Boller, "Fabrication and characterization of free-standing, high-line-density transmission gratings for the vacuum UV to soft X-ray range", Opt. Express **23**, 4421–4434 (2015).

[68]M. Bayraktar, H. M. Bastiaens, C. Bruineman, B. Vratzov, and F. Bijkerk, "Broadband transmission grating spectrometer for measuring the emission spectrum of EUV sources", NEVAC blad **54**, 14–19 (2016).

[69]M. M. Basko, "On the maximum conversion efficiency into the 13.5-nm extreme ultraviolet emission under a steady-state laser ablation of tin microspheres", Phys. Plasmas **23**, 083114 (2016).

[70]D. Kurilovich, M. M. Basko, D. A. Kim, F. Torretti, R. Schupp, J. C. Visschers, J. Scheers, R. Hoekstra, W. Ubachs, and O. O. Versolato, "Power-law scaling of plasma pressure on laser-ablated tin microdroplets", Phys. Plasmas **25**, 012709 (2018).

[71]B. O'Shay, F. Najmabadi, S. S. Harilal, and M. S. Tillack, "Nanosecond spectroscopy of expanding laser-produced tin plasma", in J. Phys. Conf. Ser. Vol. 59, 1 (2007), 165.

[72]M. S. Tillack, K. L. Sequoia, and Y. Tao, "Geometric effects on EUV emissions in spherical and planar targets", in J. Phys. Conf. Ser. Vol. 112, 4 (IOP Publishing, 2008), 042060.

[73]R. A. Meijer, A. S. Stodolna, K. S. E. Eikema, and S. Witte, "High-energy Nd:YAG laser system with arbitrary sub-nanosecond pulse shaping capability", Opt. Lett. **42**, 2758–2761 (2017).

[74]A. Kramida, Y. Ralchenko, J. Reader, and and NIST ASD Team, NIST Atomic Spectra Database (ver. 5.3), [Online]. Available: `http://physics.nist.gov/asd` [2016, February 2]. National Institute of Standards and Technology, Gaithersburg, MD., 2015.

[75]M. Yamaura, S. Uchida, A. Sunahara, Y. Shimada, H. Nishimura, S. Fujioka, T. Okuno, K. Hashimoto, K. Nagai, T. Norimatsu, K. Nishihara, N. Miyanga, Y. Izawa, and C. Yamanaka, "Characterization of extreme ultraviolet emission using the fourth harmonic of a Nd:YAG laser", Appl. Phys. Lett. **86**, 181107 (2005).

[76]F. Torretti, R. Schupp, D. Kurilovich, A. Bayerle, J. Scheers, W. Ubachs, R. Hoekstra, and O. O. Versolato, "Short-wavelength out-of-band EUV emission from Sn laser-produced plasma", J. Phys. B: At. Mol. Opt. Phys. **51**, 045005 (2018).

[77]C. R. Phipps Jr., T. P. Turner, R. F. Harrison, G. W. York, W. Z. Osborne, G. K. Anderson, X. F. Corlis, L. C. Haynes, H. S. Steele, K. C. Spicochi, and T. R. King, "Impulse coupling to targets in vacuum by KrF, HF, and CO_2 single-pulse lasers", J. Appl. Phys. **64**, 1083–1096 (1988).

[78]M. Murakami, J. Meyer-ter-Vehn, and R. Ramis, "Thermal X-Ray Emission from Ion-Beam-Heated Matter", J. Xray Sci. Technol. **2**, 127–148 (1990).

[79]M. Murakami, S. Fujioka, H. Nishimura, T. Ando, N. Ueda, Y. Shimada, and M. Yamaura, "Conversion efficiency of extreme ultraviolet radiation in laser-produced plasmas", Phys. Plasmas **13**, 033107 (2006).

[80]O. O. Versolato, "Physics of laser-driven tin plasma sources of EUV radiation for nanolithography", Plasma Sources Sci. Technol. **28**, 083001 (2019).

[81]S. K. Moore, "EUV lithography finally ready for fabs", IEEE Spectrum **55**, 46–48 (2018).

[82]A. A. Schafgans, D. J. Brown, I. V. Fomenkov, R. Sandstrom, A. Ershov, G. Vaschenko, R. Rafac, M. Purvis, S. Rokitski, Y. Tao, D. J. Riggs, W. J. Dunstan, M. Graham, N. R. Farrar, D. C. Brandt, N. Böwering, A. Pirati, N. Harned, C. Wagner, H. Meiling, and R. Kool, "Performance optimization of MOPA pre-pulse LPP light source", in EUV Lithography VI, Vol. 9422 (SPIE, 2015), 94220B.

[83]M. A. Purvis, A. Schafgans, D. J. W. Brown, I. Fomenkov, R. Rafac, J. Brown, Y. Tao, S. Rokitski, M. Abraham, M. Vargas, S. Rich, T. Taylor, D. Brandt, A. Pirati, A. Fisher, H. Scott, A. Koniges, D. Eder, S. Wilks, A. Link, and S. Langer, "Advancements in predictive plasma formation modeling", in EUV Lithography VII, Vol. 9776 (SPIE, 2016), 97760K.

[84]R. Schupp, F. Torretti, R. A. Meijer, M. Bayraktar, J. Scheers, D. Kurilovich, A. Bayerle, K. S. E. Eikema, S. Witte, W. Ubachs, R. Hoekstra and O. O. Versolato, "Efficient generation of extreme ultraviolet light from Nd: YAG-driven microdroplet-tin plasma", Phys. Rev. Appl. **12**, 014010 (2019).

[85]D. Colombant and G. F. Tonon, "X-ray emission in laser-produced plasmas", J. Appl. Phys. **44**, 3524–3537 (1973).

[86]V. Bakshi, *EUV sources for lithography*, Vol. 149 (SPIE press Bellingham, Washington, 2006).

[87]A. Hassanein, V. A. Sizyuk, T. S. Sizyuk, and S. S. Harilal, "Effects of plasma spatial profile on conversion efficiency of laser-produced plasma sources for EUV lithography", J. Micro/Nanolithogr. MEMS MOEMS **8**, 041503 (2009).

[88]A. Hassanein, T. Sizyuk, V. Sizyuk, and S. S. Harilal, "Combined effects of prepulsing and target geometry on efficient EUV production from laser produced plasma experiments and modeling", in EUV Lithography II, Vol. 7969 (SPIE, 2011), 79690D.

[89]R. Schupp, F. Torretti, R. A. Meijer, M. Bayraktar, J. Sheil, J. Scheers, D. Kurilovich, A. Bayerle, A. A. Schafgans, M. Purvis, K. S. E. Eikema, S. Witte, W. Ubachs, R. Hoekstra, and O. O. Versolato, "Radiation transport and scaling of optical depth in Nd:YAG laser-produced microdroplet-tin plasma", Appl. Phys. Lett. **115**, 124101 (2019).

[90]S. S. Harilal, T. Sizyuk, A. Hassanein, D. Campos, P. Hough, and V. Sizyuk, "The effect of excitation wavelength on dynamics of laser-produced tin plasma", J. Appl. Phys. **109**, 063306 (2011).

[91]C. W. Siders, A. C. Erlandson, T. C. Galvin, H. Frank, S. Langer, B. A. Reagan, H. Scott, E. F. Sistrunk, and T. M. Spinka, *Efficient high power laser drivers for next-generation High Power EUV sources*, EUV Source Workshop 2019, presented: November 6, 2019.

[92]G. Arisholm, Ø. Nordseth, and G. Rustad, "Optical parametric master oscillator and power amplifier for efficient conversion of high-energy pulses with high beam quality", Opt. Express **12**, 4189–4197 (2004).

[93]J. Scheers, C. Shah, A. Ryabtsev, H. Bekker, F. Torretti, J. Sheil, D. A. Czapski, J. C. Berengut, W. Ubachs, J. R. Crespo López-Urrutia, R. Hoekstra, and O. O. Versolato, "EUV spectroscopy of highly charged Sn^{13+}–Sn^{15+} ions in an electron-beam ion trap", Phys. Rev. A **101**, 062511 (2020).

[94]K. L. Sequoia, Y. Tao, S. Yuspeh, R. Burdt, and M. S. Tillack, "Two dimensional expansion effects on angular distribution of 13.5 nm in-band extreme ultraviolet emission from laser-produced Sn plasma", Appl. Phys. Lett. **92**, 221505 (2008).

[95]H. Chen, H. Lan, Z.-Q. Chen, L.-N. Liu, T. Wu, D.-L. Zuo, P.-X. Lu, and X.-B. Wang, "Experimental study on laser produced tin droplet plasma extreme ultraviolet light source", Acta Phys. Sin. **64**, 075202 (2015).

[96]J. P. Apruzese, J. Davis, K. G. Whitney, J. W. Thornhill, P. C. Kepple, R. W. Clark, C. Deeney, C. A. Coverdale, and T. W. L. Sanford, "The physics of radiation transport in dense plasmas", Phys. Plasmas **9**, 2411–2419 (2002).

[97]A. Sasaki, A. Sunahara, K. Nishihara, T. Nishikawa, K. Fujima, T. Kagawa, F. Koike, and H. Tanuma, "Atomic modeling of the plasma EUV sources", High Energy Density Phys. **3**, 250–255 (2007).

[98]C. N. Danson, C. Haefner, J. Bromage, T. Butcher, J.-C. F. Chanteloup, E. A. Chowdhury, A. Galvanauskas, L. A. Gizzi, J. Hein, D. I. Hillier, N. W. Hopps, Y. Kato, E. A. Khazanov, R. Kodama, G. Korn, R. Li, Y. Li, J. Limpert, J. Ma, N. Chang-hee, D. Neely, D. Papadopoulos, R. R. Penman, L. Qian, J. J. Rocca, A. A. Shaykin, C. W. Siders, C. Spindloe, S. Szatmári, R. M. G. M. Trines, J. Zhu, P. Zhu, and J. D. Zuegel, "Petawatt and exawatt class lasers worldwide", High Power Laser Sci. Eng. **7** (2019).

[99]F. Torretti, F. Liu, M. Bayraktar, J. Scheers, Z. Bouza, W. Ubachs, R. Hoekstra, and O. O. Versolato, "Spectral characterization of an industrial EUV light source for nanolithography", J. Phys. D: Appl. Phys. **53**, 055204 (2019).

[100]Z. Bouza, J. Scheers, A. N. Ryabtsev, R. Schupp, L. Behnke, C. Shah, J. Sheil, M. Bayraktar, J. R. Crespo López-Urrutia, W. Ubachs, R. Hoekstra, and O. O. Versolato, "EUV spectroscopy of Sn^{5+}–Sn^{10+} ions in an electron beam ion trap and laser-produced plasmas", J. Phys. B: At. Mol. Opt. Phys. **53**, 195001 (2020).

[101]L. Oster, "Emission, absorption, and conductivity of a fully ionized gas at radio frequencies", Rev. Mod. Phys. **33**, 525–543 (1961).

[102]H. A. Kramers, "XCIII. On the theory of X-ray absorption and of the continuous X-ray spectrum", Philos. Mag. **46**, 836–871 (1923).

[103]H. Mizoguchi, H. Nakarai, T. Abe, K. M. Nowak, Y. Kawasuji, H. Tanaka, Y. Watanabe, T. Hori, T. Kodama, Y. Shiraishi, T. Yanagida, G. Soumagne, T. Yamada, T. Yamazaki, and T. Saitou, "High power LPP-EUV source with long collector mirror lifetime for high volume semiconductor manufacturing", in Proc. CSTIC 2018 (IEEE, 2018), 1–7.

[104]K. Nishihara, A. Sunahara, A. Sasaki, M. Nunami, H. Tanuma, S. Fujioka, Y. Shimada, K. Fujima, H. Furukawa, T. Kato, F. Koike, R. More, M. Murakami, T. Nishikawa, V. Zhakhovskii, K. Gamata, A. Takata, H. Ueda, H. Nishimura, Y. Izawa, N. Miyanaga, and K. Mima, "Plasma physics and radiation hydrodynamics in developing an extreme ultraviolet light source for lithography", Phys. Plasmas **15**, 056708 (2008).

[105]S. Fujioka, M. Shimomura, Y. Shimada, S. Maeda, H. Sakaguchi, Y. Nakai, T. Aota, H. Nishimura, N. Ozaki, A. Sunahara, K. Nishihara, N. Miyanaga, Y. Izawa, and K. Mima, "Pure-tin microdroplets irradiated with double laser pulses for efficient and minimum-mass extreme-ultraviolet light source production", Appl. Phys. Lett. **92**, 241502 (2008).

[106]R. Schupp, L. Behnke, J. Sheil, Z. Bouza, M. Bayraktar, W. Ubachs, R. Hoekstra, and O. O. Versolato, "Characterization of 1- and 2-µm-wavelength laser-produced microdroplet-tin plasma for generating extreme ultraviolet light", submitted.

[107]L. Behnke, R. Schupp, Z. Bouza, M. Bayraktar, Z. Mazzotta, R. Meijer, J. Sheil, S. Witte, W. Ubachs, R. Hoekstra, and O. O. Versolato, "Extreme ultraviolet light from a tin plasma driven by a 2-µm-wavelength laser", Opt. Express **29**, 4475–4487 (2021).

[108]H. Matsukuma, A. Sunahara, T. Yanagida, H. Tomuro, K. Kouge, T. Kodama, T. Hosoda, S. Fujioka, and H. Nishimura, "Correlation between laser absorption and radiation conversion efficiency in laser produced tin plasma", Appl. Phys. Lett. **107**, 121103 (2015).

[109]T. Higashiguchi, N. Dojyo, M. Hamada, W. Sasaki, and S. Kubodera, "Low-debris, efficient laser-produced plasma extreme ultraviolet source by use of a regenerative liquid microjet target containing tin dioxide (SnO_2) nanoparticles", Appl. Phys. Lett. **88**, 201503 (2006).

[110]D. Nakamura, T. Akiyama, K. Okazaki, K. Tamaru, A. Takahashi, and T. Okada, "Ablation dynamics of tin micro-droplet irradiated by double pulse laser used

for extreme ultraviolet lithography source", J. Phys. D: Appl. Phys. **41**, 245210 (2008).

[111]I. W. Choi, H. Daido, S. Yamagami, K. Nagai, T. Norimatsu, H. Takabe, M. Suzuki, T. Nakayama, and T. Matsui, "Detailed space-resolved characterization of a laser-plasma soft-x-ray source at 13.5-nm wavelength with tin and its oxides", J. Opt. Soc. Am. B **17**, 1616–1625 (2000).

[112]B. Liu, D. Kurilovich, H. Gelderblom, and O. O. Versolato, "Mass Loss from a Stretching Semitransparent Sheet of Liquid Tin", Phys. Rev. Appl. **13**, 024035 (2020).

[113]B. Liu, R. A. Meijer, J. Hernandez-Rueda, D. Kurilovich, Z. Mazzotta, S. Witte, and O. O. Versolato, "Laser-induced vaporization of a stretching sheet of liquid tin", accepted (2021).

[114]G. D. O'Sullivan and R. Faulkner, "Tunable narrowband soft x-ray source for projection lithography", Opt. Eng. **33**, 3978–3984 (1994).

[115]T. Sizyuk and A. Hassanein, "Tuning laser wavelength and pulse duration to improve the conversion efficiency and performance of EUV sources for nano-lithography", Phys. Plasmas **27**, 103507 (2020).

List of publications

Chapter 1
R. Schupp, F. Torretti, R. A. Meijer, M. Bayraktar, J. Scheers, D. Kurilovich, A. Bayerle, K. S. E. Eikema, S. Witte, W. Ubachs, R. Hoekstra, and O. O. Versolato, "Efficient generation of extreme ultraviolet light from Nd:YAG-driven microdroplet-tin plasma", Phys. Rev. Appl. **12**, 014010 (2019)

Chapter 2
R. Schupp, F. Torretti, R. A. Meijer, M. Bayraktar, J. Sheil, J. Scheers, D. Kurilovich, A. Bayerle, A. A. Schafgans, M. Purvis, K. S. E. Eikema, S. Witte, W. Ubachs, R. Hoekstra, and O. O. Versolato, "Radiation transport and scaling of optical depth in Nd:YAG laser-produced microdroplet-tin plasma", Appl. Phys. Lett. **115**, 124101 (2019)

Chapter 3
L. Behnke, **R. Schupp**, Z. Bouza, M. Bayraktar, Z. Mazzotta, R. Meijer, J. Sheil, S. Witte, W. Ubachs, R. Hoekstra, and O. O. Versolato, "Extreme ultraviolet light from a tin plasma driven by a 2-μm-wavelength laser", Opt. Express **29**, 4475-4487 (2021)

Chapter 4
R. Schupp, L. Behnke, J. Sheil, Z. Bouza, M. Bayraktar, W. Ubachs, R. Hoekstra, and O. O. Versolato, "Characterization of 1- and 2-μm-wavelength laser-produced microdroplet-tin plasma for generating extreme ultraviolet light", submitted

Chapter 5
R. Schupp, L. Behnke, Z. Bouza, J. Sheil, M. Bayraktar, W. Ubachs, R. Hoekstra, and O. O. Versolato, "Characterization of angularly resolved EUV emission from 2-μm-wavelength laser-driven Sn plasma using preformed liquid disk targets", to be submitted

The author also contributed to the following publications:

1. F. Torretti, J. Sheil, **R. Schupp**, M. M. Basko, M. Bayraktar, R. A. Meijer, S. Witte, W. Ubachs, R. Hoekstra, O. O. Versolato, A. J. Neukirch, and J. Colgan, "Prominent radiative contributions from multiply-excited states in laser-produced tin plasma for nanolithography", Nat. Commun. **11**, 2334 (2020)
2. J. Scheers, **R. Schupp**, R. Meijer, W. Ubachs, R. Hoekstra, and O. O. Versolato, "Time- and space-resolved optical Stark spectroscopy in the afterglow of laser-produced tin-droplet plasma", Phys. Rev. E **102**, 013204 (2020)
3. Z. Bouza, J. Scheers, A. Ryabtsev, **R. Schupp**, L. Behnke, C. Shah, J. Sheil, M. Bayraktar, J. R. Crespo López-Urrutia, W. Ubachs, R. Hoekstra, and O. O. Versolato, "EUV spectroscopy of Sn^{5+}–Sn^{10+} ions in an electron beam ion trap and laser-produced plasmas", J. Phys. B: At. Mol. Opt. Phys. **53**, 195001 (2020)
4. R. A. Meijer, **R. Schupp**, J. Sheil, K. S. E. Eikema, O. O. Versolato, and S. Witte, "Spall velocity reduction in double-pulse impact on tin microdroplets", submitted
5. F. Torretti, **R. Schupp**, D. Kurilovich, A. Bayerle, J. Scheers, W. Ubachs, R. Hoekstra, and O. O. Versolato, "Short-wavelength out-of-band EUV emission from Sn laser-produced plasma", J. Phys. B: At. Mol. Opt. Phys. **51**, 045005 (2018)
6. D. Kurilovich, M. M. Basko, D. A. Kim, F. Torretti, **R. Schupp**, J. C. Visschers, J. Scheers, R. Hoekstra, W. Ubachs, and O. O. Versolato, "Power-law scaling of plasma pressure on laser-ablated tin microdroplets", Phys. Plasmas **25**, 012709 (2018)
7. D. Kurilovich, T. de F. Pinto, F. Torretti, **R. Schupp**, J. Scheers, A. S. Stodolna, H. Gelderblom, K. S. E. Eikema, S. Witte, W. Ubachs, R. Hoekstra, and O. O. Versolato, "Expansion dynamics after laser-induced cavitation in liquid tin microdroplets", Phys. Rev. Appl. **10**, 054005 (2018).
8. J. Scheers, A. Ryabtsev, A. Borschevsky, J. C. Berengut, K. Haris, **R. Schupp**, D. Kurilovich, F. Torretti, A. Bayerle, E. Eliav, W. Ubachs, O. O. Versolato, and R. Hoekstra, "Energy level structure of Sn^{3+} ions", Phys. Rev. A **98**, 062503 (2018)

In addition to these publications, the work presented in this thesis resulted in 7 application ideas shared with ASML.

Acknowledgments

After five years my chapter at ARCNL nears its end. I would like to thank all my colleagues, family and friends that were part of my PhD journey.

First to thank is Oscar who provided me with the possibility to do my PhD in his research group. Thank you very much for the guidance and help you provided me with thoughout my PhD. I much enjoyed your continuous enthusiasm and positivity. I would like to extend this thank you to my other two promotors Wim and Ronnie who were always very welcoming and happy to dedicate time for discussions. Thank you also for the diligent proofreading of my manuscripts that resulted in this thesis.

Next to my promotors, I would like to thank my group members. All the hours spent in the lab and office were made much more enjoyable by working together with you. Thanks to Lars, Zoi, Yahia, Bo, Lucas, Dmitry, Adam, Javier, Francesco, Alex, Diko, Edcel, Sjoerd, Jim, Subam, Mart-Johan, Klaas, Jaap and Job. In addition to my direct group members, I would like to thank Stefan, Randy, Zeudi and Aneta from the EUV Generation and Imaging group who I worked closely with and who built and maintained a marvelous laser system that I used in lots of experiments. I separately would like to thank my paranymphs John and Joris for their help during the final stage of my thesis and its defense. We had a great time together at and outside of ARCNL. A highlight of which certainly was our visit to the APiP conference which was, to put it in John's words, 'unreal'. An essential part of every research group are the technicians. Thank you Laurens and Thomas for all your hard work in helping to build and maintain our experimental setups. Thanks also to the technicians of the other groups at ARCNL who were always happy to help whenever a hand was needed.

During my PhD I further had the opportunity to work with a number of people outside of ARCNL that I would like to thank. Muharrem Bayraktar provided us with a great EUV spectrometer and also joined experimental campaigns at ARNCL. The obtained data was frequently discussed with our ASML contact person Wim van der Zande, whose questions and suggestions helped to strengthen the manuscripts in this thesis. Our colleagues Alexander Schafgans and Michael Purvis from ASML San Diego kindly provided us with spectra of CO_2 laser-driven tin plasmas that were used in Chapter 2. Stefan Bäumer from TNO kindly made time for questions and

discussions regarding laser optics and laser beam imaging that were very helpful during the start of my PhD. Starting from the discussions with Stefan, Jelmer Weda (technician at the VU at the time) helped me with the design of optical elements.

A key element to a PhD project is technical advice and guidance provided by the support staff. I would like to thank the mechanical engineering department, in particular Henk-Jan and Iliya who provided lots of clever designs and helped in making setup figures for this thesis. After the drawings are finalized, the parts need to be machined. Fortunately, we have an excellent mechanical workshop. Thanks to Jan, Wessel, Tom, Menno, Ricardo and Niels for machining our Dalek setup as well as many other parts. Materials and parts can only be machined after they have been ordered. Thanks to the finance and the purchasing department, and especially to André, Radjin and Angela. Once a setup is up and running it would be tedious to obtain data without a good data acquisition software. Thanks to Jorijn and Marco from the software department for an excellent piece of data acquisition software. Thank you also for your patience whenever we asked you to add yet another camera to the abundance of devices that were already controlled by your software. A thank you is also needed for the ICT department. Carl, Cees, Gerben, Wiebe and Richard helped a lot with the hardware of the data acquisition system. Another person I would like to thank is Rutger who repaired my laptop on multiple occasions whenever it decided to die on me once again. For their help with any question regarding read-out electronics and the design of smart circuit boards that also survive the hands of a physicist, I would like to thank the electronics department and in particular Dico, Duncan, Pepijn and Bob. Whenever I had any questions, the secretaries were at hand to answer them. Thanks to Romy, Rosa and Cathelijne.

Next to the working conditions, I very much enjoyed the atmosphere at ARNCL. Thank you Marjan and Joost for providing a framework in which both are possible. I would like to thank the PV who organized a lot of fun events such as outings, borrels and Christmas parties. Aside from the PV events, I always had a good time during the coffee break or when having a beer with friends and colleagues from both ARNCL and AMOLF. Thank you Ale A., Caro, Guido, Victor, Fiona, Stephen, Tiago, Maisie, Görsel, Vanessa, Ale T., Jan, Neha, Amelie, Kuan-Da, Lars L., Marco, Lorenzo, Giorgio, Feng-Chun, Christina, Zoey, Eliane, Verena, Lucie, Florian, Ruslan, Roberto, Daan, Maarten, Sylvianne, Christos and Filippo.

Finally, I would like thank my family for their continuous support that they provide me with. To my parents Manuela and Stefan and my sister Julia.